NTNU

Norwegian University of
Science and Technology

Novel Short-pulsed Holmium-fiber Master Oscillator Power Amplifier for LiDAR applications

Ingrid Katrina Bakke

Master of Science in Physics and Mathematics
Submission date: June 2018
Supervisor: Irina T Sorokina, IFY

Norwegian University of Science and Technology
Department of Physics

Preface

I would like to thank Irina Sorokina and Nikolai Tolstik for immense help with guiding and reviewing this thesis.

Abstract

Pulsed lasers enable a number of technologies including LiDAR (Light Imaging Detection and Ranging). Among significant remote sensing LiDAR applications are tracing of atmospheric gases, which is important for climate change research, and range finding, which is of great relevance for the development autonomous vehicles. The $2-2.5$ μm spectral atmospheric window is considered to be the ideal window for remote sensing, when taking atmospheric transmittance, scattering, state-of-the-art detector technology and eye safety into account. Promising LiDAR laser sources emitting within this window are fiber lasers and semiconductor laser diodes (LDs) as they are electrically controlled, tunable, robust and light-weight. The output power of master oscillators, such as fiber lasers and LDs, can be scaled by fiber amplifiers. Such combinations are examples of master oscillator power amplifiers (MOPAs).

For this thesis a light-weight, compact, all-diode-pumped single-mode polarization-maintaining holmium-doped all-fiber amplifier providing amplification in the $2-2.1$ μm spectral region has been developed. The amplifier successfully provided a maximal 18 dB gain for a 0.5 mW average power signal from a mode-locked holmium-doped fiber laser emitting pulses of picosecond duration at a repetition rate of 3.81 MHz and at 2089 nm wavelength. The amplifier operated with a slope efficiency of 10 %, and an optical-to-optical efficiency of 5.3 % at maximum amplification. A complementary numerical model describing the behavior of the amplifier has been developed and was improved using experimental data.

A MOPA, integrating the mode-locked fiber laser and the amplifier, has been demonstrated as the laser source in a proof of principle range-finding LiDAR. While operating this MOPA to emit pulses of 3.5 ps duration at 2088.8 nm wavelength at a repetition frequency of 3.81 MHz and 8 mW average power, the LiDAR could successfully measure distance to a reflective target. The LiDAR range resolution was 6.1 mm. The LiDAR maximal range of 39 m is limited by the repetition rate of the mode-locked laser.

Additionally, a gain-switched discrete-mode LD has been considered as a potential LiDAR laser source. The LD was seen to be tunable in the wavelength range between 2051 and 2053 nm with a laser linewidth less than 0.05 nm, and could be driven to emit pulses of 1 ns duration with peak power of 6 mW, and at repetition rate set between 10-100 kHz. The improved amplifier numerical model predicts an amplification of the LD peak power to 0.8 W. Range-finding LiDAR parameters have been estimated for a LiDAR where the laser source is a MOPA, consisting of the amplifier and the LD, nd referred to as the LD-MOPA, emitting pulses with peak power of 0.8 W and 1 ns pulse duration at a 10 kHz repetition rate. This LD-MOPA based LiDAR would allow range finding to a reflective target up to a peak power-limited maximal distance of 1.6 km, and with a range resolution of 15 cm. If power were scaled, the 10 kHz repetition rate limited maximal range for the same LiDAR is 15 km.

To allow further amplification of the LD-MOPA output, a 2^{nd} stage holmium-doped power amplifier has been planned, and a complementary time-dependent numerical model developed. The 2^{nd} stage power amplifier model, estimates amplification of LD-MOPA peak power to megawatt level, and shortening of LD-MOPA pulse width from 1 ns to 200 ps duration. Calculations show that this will be sufficient to range allow range finding up to 15 km, and will improve range resolution to 3.5 cm.

Finally, the possibility of using the wavelength-tunable LD as the single laser source in a DIAL (differential absorption LiDAR) for sensing of atmospheric CO_2 concentrations has been discussed.

Sammendrag

Pulsede lasere muliggjør flere teknologier som inkluderer LiDAR (Light Imaging Detection and Ranging). Blandt betydningsfulle fjernanalyse LiDAR anvendelser er overvåkning av atmosfæriske gasser, som er viktig for forskning innen klimaendringer, og avstandsmåling, som er relevant for utvikling av selvkjørende kjøretøy. Det $2-2.5$ μm spektrale atmosfæriske vinduet er ansett som det ideelle vinduet for fjernanalyse, når en tar atmosfærisk transmisjon, spredning, nyeste detektor teknologi og øyesikkerhet i betraktning. Lovende LiDAR-laserkilder som utstråler i dette vinduet, er fiberlasere og halvleder laserdioder (LDer), da de er elektrisk styrbare, bølgelengdejusterbare, robuste og lette. Intensiteten til masteroscillatorer, som fiberlasere og LD-er, kan forsterkes av fiberforsterkere. Slike kombinasjoner er eksempler på master oscillator power amplifiers (MOPAer).

Til denne oppgaven er det utviklet en lett, kompakt, ren-diode-pumpet singel-mode polariserings-vedlikeholdende holmiumdopet bare-fiber forsterker som forsterker i $2-2.1$ μm spektralområdet. Forsterkeren ga vellykket en maksimal forsterkning på 18 dB for et signal med 0.5 mW gjennomsnittlig intensitet fra en mode-låst holmiumdopet fiber-laser som sender ut pulser med pikosekundvarighet ved en repetisjonsfrekvens på 3.81 MHz og ved 2089 nm bølgelengde. Forsterkeren opererte med en stigningsvirkningsgrad på 10% og en optisk-til-optisk virkningsgrad på 5,3% ved maksimal forsterkning. En komplementær numerisk modell som beskriver oppførselen til forsterkeren er blitt utviklet og ble forbedret ved hjelp av eksperimentelle data.

En MOPA, som integrerer den mode-låste fiberlaseren og forsterkeren, har blitt demonstrert som laserkilde i en bevis-på-prinsipp avstandsmålende LiDAR. Ved at denne MOPA-en sender ut pulser med 3.5 ps varighet ved 2088.8 nm bølgelengde med en repetisjonsfrekvens på 3.81 MHz og 8 mW gjennomsnittlig intensitet, kunne LiDARen vellykket måle avstanden til et reflekterende mål. LiDAR-oppløsningen var 6.1 mm. LiDARens rekkevidde på 39 m er begrenset av repeteringsfrekvensen til den mode-låste laseren.

I tillegg er en forsterknings-variert, diskret mode LD blitt vurdert som en potensiell LiDAR laserkilde. LDen viste seg justerbar i bølgelengdeområdet mellom 2051 og 2053 nm med en laserlinjebredde mindre enn 0.05 nm, og kunne bli drevet til å sende ut pulser med 1 ns varighet, med en toppintensitet på 6 mW og ved repetisjonsfreknvens satt mellom 10 - 100 kHz. Den forbedrede forsterkerens numeriske modell anslår en forsterkning av LD-toppintensitetn til 0.8 W. Avstandsmålende LiDAR-parametere er estimert for en LiDAR hvor laserkilden er en MOPA, som består av forsterkeren og LDen, heretter referert til som LD-MOPAen, som sender ut pulser med toppintensitet på 0.8 W og 1 ns pulsvarighet med en 10 kHz repetisjonfrekvens. Denne LD-MOPA-baserte LiDARen vil tillate en avstand til et reflekterende mål på opptil en toppintensitetsbegrenset rekkevidde på 1.6 km, og med en oppløsning på 15 cm. Hvis intensiteten ble skalert, er den 10 kHz repitisjonsfrekvensbegrensede rekkevidden for samme LiDAR 15 km.

For å tillate ytterligere forsterkning av LD-MOPA-intensiteten, har en 2.-trinns holmiumdopet forsterker blitt planlagt, og en komplementær tidsavhengig numerisk modell blitt utviklet. Den 2.-trinns forsterkermodellen anslår forsterkning av LD-MOPA-toppintensiteten til megawattnivå, og forkortelse av LD-MOPA pulsbredden fra 1 ns til 200 ps varighet. Beregninger viser at dette vil være tilstrekkelig til at avstandsmåling opptil en rekkevidde på 15 km er mulig, og vil forbedre oppløsningen til 3.5 cm.

Til slutt er muligheten for å bruke den bølgelengdejusterbare LDen som eneste laserkilde i en DIAL (differential absorption LiDAR) for å finne atmosfæriske CO_2-konsentrasjoner blitt diskutert.

Abbreviations

ASE	=	Amplified Spontaneous Emission
BW	=	Band Width
CW	=	Continuous Wave
DIAL	=	Differential Absorption LIDAR
DM	=	Discrete Mode
FBG	=	Fiber Bragg Grating
FH	=	Fiber Holder
FOV	=	Field Of View
FWHM	=	Full Width Half Maximum
IR	=	Infrared
LASER	=	Light Amplification by Stimulated Emission of Radiation
LiDAR	=	Light Imaging Detection and Ranging
LD	=	Laser Diode
LMA	=	Large Mode Area
MOPA	=	Master Oscillator Power Amplifier
MQW	=	Multiple Quantum Well
NA	=	Numerical Aperture
NEP	=	Noise Equivalent Power
PM	=	Polarization-Maintaining
radar	=	RAdio Detection And Ranging
SNR	=	Signal to Noise Ratio
SOA	=	Semiconductor Optical Amplifier
TEC	=	Thermoelectric Cooler
TOF	=	Time Of Flight
UV	=	Ultraviolet
WDM	=	Wavelength Division Multiplexer

List of Symbols

A_{det}	=	detector area
A_r	=	LiDAR receiver aperture
A_T	=	illuminated by LiDAR beam cross sectional target area
c	=	speed of light in a given medium
d_{clad}	=	fiber cladding diameter
d_{core}	=	fiber core diameter
D	=	fiber core diameter
D_r	=	LiDAR receiver aperture diameter
D_T	=	target diameter
E_1	=	lower energy level in a two level scheme
E_2	=	upper energy level in a two level scheme
E_{pulse}	=	pulse energy
f_{rep}	=	repetition frequency
G	=	total Gain
h	=	Planck's constant (= 6.63×10^{-34} Js)
I	=	light intensity
I	=	current
I_{dark}	=	detector dark current
I_{on}	=	on current periodically injected into pulsed laser diode
I_p	=	pump light intensity
I_s	=	signal light intensity
I_{th}	=	current injected into laser diode threshold for lasing
I_{therm}	=	thermistor current
${}^5I_x$	=	Relevant Holmium energy level, with level index x
k_B	=	Boltzmann's constant (= 1.38×10^{-23} JK^{-1})
L	=	waveguide length
L	=	total fiber amplifier length
L	=	total mode-locked fiber laser length
m	=	spatial mode number in a fiber
M^2	=	M^2 number
n_{clad}	=	fiber cladding refractive index
n_{core}	=	fiber core refractive index
n_0	=	refractive index of medium surrounding the fiber
n_1	=	fractional population of the lower laser level
n_2	=	fractional population of the upper laser level
N	=	number of ions in a two level system
N	=	doping concentration
N_{Ho}	=	holmium doping concentration
N_a	=	atmospheric absorber concentration
N_s	=	atmospheric scatterer concentration
N_1	=	number of lower level ions in a two level system
N_2	=	number of upper level ions in a two level system
O	=	overlap function
P_{avg}	=	average power
P_{noise}	=	noise power
P_{noise}^{BG}	=	background noise power
P_{noise}^{det}	=	internal noise power in LiDAR detector
P_{peak}	=	pulse peak power

P_p	=	pump power
P_p^{in}	=	pump input power
$P_{p,th}^{in}$	=	pump input power threshold for lasing
P_r	=	LiDAR return power
$P_{r,min}$	=	minimal detectable LiDAR return power
P_s	=	signal power
P_s^{in}	=	signal input power
P_t	=	transmitted LiDAR power
q	=	heat loss due to the quantum defect
q	=	atmospheric scatterer radius
$\mathscr{R}$	=	Photodetector responsivity
R	=	range between target and LiDAR
R_{max}	=	maximal coverage range between target and transmitter/receiver or maximal range of LiDAR
R_{therm}	=	thermistor resistance
t	=	time
$\mathscr{T}$	=	atmospheric transmittance
t_{ret}	=	LiDAR return time
t_{offset}	=	LiDAR offset time
t_{rise}	=	rise time
$\mathscr{R}$	=	photodetector responsivity
T	=	temperature
T_{rep}	=	repetition period
V	=	V parameter of fiber
V_{therm}	=	thermistor voltage
V_{trig}	=	are electrical trigger pulse voltage amplitude
w	=	Gaussian beam waist radius
W_{ij}	=	rate of transition between energy levels i and j
x	=	distance into the fiber

β	=	backscatter coefficient
$\Delta_{\lambda,r}$	=	LiDAR detector response wavelength interval
$\Delta\nu$	=	light frequency width
ΔR	=	range resolution
$\Delta R^{\perp}$	=	LiDAR transverse resolution
Δt	=	pulse duration
Δt_{trig}	=	electrical trigger pulse duration
ϵ	=	Average energy difference between two manifolds of energy sublevels
η	=	optical-to-optical efficiency
η_s	=	slope efficiency
η_{sys}	=	LiDAR system optics efficiency
η_q	=	quantum defect limited efficiency
γ	=	gain
λ	=	light wavelength
λ_{on}	=	DIAL on wavelength
λ_{off}	=	DIAL off wavelength
λ_s	=	signal wavelength
λ_p	=	pump wavelength
ν	=	light frequency
ν_p	=	frequency of pump light
ν_s	=	frequency of signal light
Ω_T	=	solid angle into which the target reflects
$\Omega_{FOV,r}$	=	LiDAR receiver solid angle field of view
ρ	=	target reflectance
σ	=	cross section
σ_a	=	atmospheric absorber cross section
σ_{abs}	=	absorption cross section
σ_g	=	atmospheric scatterer geometric cross section
σ_{eff}	=	effective cross section
σ_{em}	=	emission cross section
σ_s	=	atmospheric scatterer cross section
τ	=	lifetime of an upper level
τ_{nr}	=	non radiative lifetime of an upper level
τ_r	=	radiative lifetime of an upper energy level
θ	=	Gaussian beam angle of divergence upon exiting the waveguide
θ_c	=	Nongaussian beam angle of divergence upon exiting the waveguide
θ_m	=	angle of spatial mode m in a fiber
θ_t	=	LiDAR transmitter angle of divergence

Table of Contents

Chapter 1

Introduction

Laser light is special because it is coherent. Coherence allows lasers to produce highly collimated beams of short pulses or continuous monochromatic light. Such properties make lasers valuable to various applications such as optical atomic clock standards [1], medicine [2] and for remote sensing LiDAR (Light Imaging Detection and Ranging) including range finding [3] and sensing of gas concentrations in the atmosphere [4]. The term "LiDAR" has come to be used for both the technique and the device performing remote sensing [5].

LiDARs for remote sensing, utilizing the time of flight (TOF) principle transmit pulses, which are either reflected or scattered back by a target. Keeping track of the pulse return time, the distance or range R may be calculated [6]. TOF LiDARs operate at laser wavelengths where the atmosphere is transparent [7]. Figure 1.1 shows how transmittance (black curve) of the atmosphere modulated by scattering (red curve) varies with wavelength. Spectral regions where the transmittance is high are recognized as atmospheric windows. Although generally considered as transparent, windows may also contain fingerprint absorption lines of specific gases [8, pp. 216-217]. Gas tracing TOF LiDARs tune the laser wavelength first to an absorption line of the gas to be traced, and then to a wavelength at which the atmosphere is transparent. Comparing the power level of the backscattered pulses, the gas density may be calculated. Such a LiDAR is called a differential absorption LiDAR (DIAL) [9].

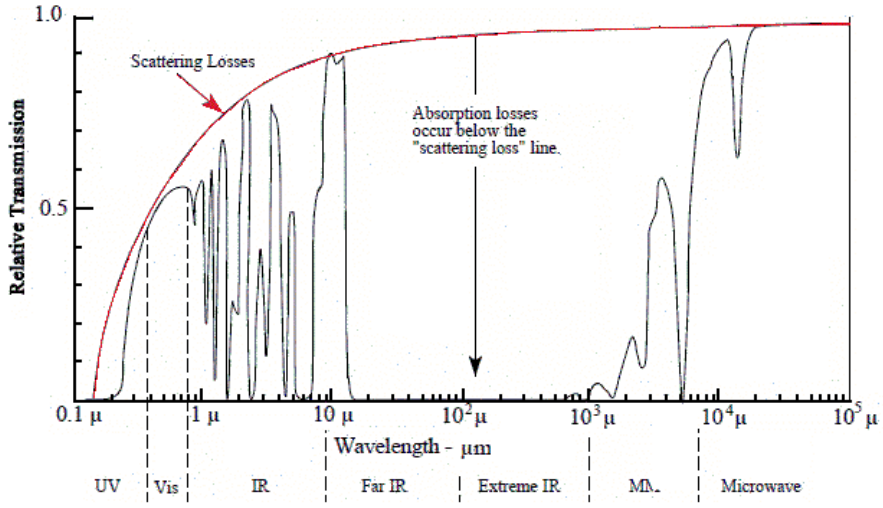

Figure 1.1: The black curve shows the spectral atmospheric transmittance due to absorption modulated by scattering (red curve). The spectral regions considered as ultraviolet (UV), visible and infrared (IR) are also marked. Appended from [10]

Today, commercial range finding LiDARS for autonomous vehicles operate at 905 nm and 1550 nm [3]. However, the $2-2.5$ μm window is considered to be the ideal window for remote sensing applications [7] for a number of reasons. First, eye safe pulse energy increases into the infrared (IR) compared to the visible [11]. Secondly, scattering due to fog, aerosols and molecules in the air, decreases with wavelength [12] towards the microwaves where traditional radar operates. Radar is however being reinvented by LiDAR in the IR due to the demand for higher resolution offered at shorter wavelengths [3]. Thirdly, state-of-the-art photodetectors needed to detect the return signal, are more sensitive in this window compared to the far IR [7]. Also, background noise due to solar radiation is significantly lower at $2-2.5$ μm than in the visible [13, p. 56]. Finally, several important green house gases have absorption lines and can be monitored within this window, as seen from Figure 1.2b. Specifically, tracing of CO_2 is considered favorable at 2.05 μm [14]. Figure 1.2a shows the atmospheric transmittance due to absorption in the $2-2.5$ μm window in more detail.

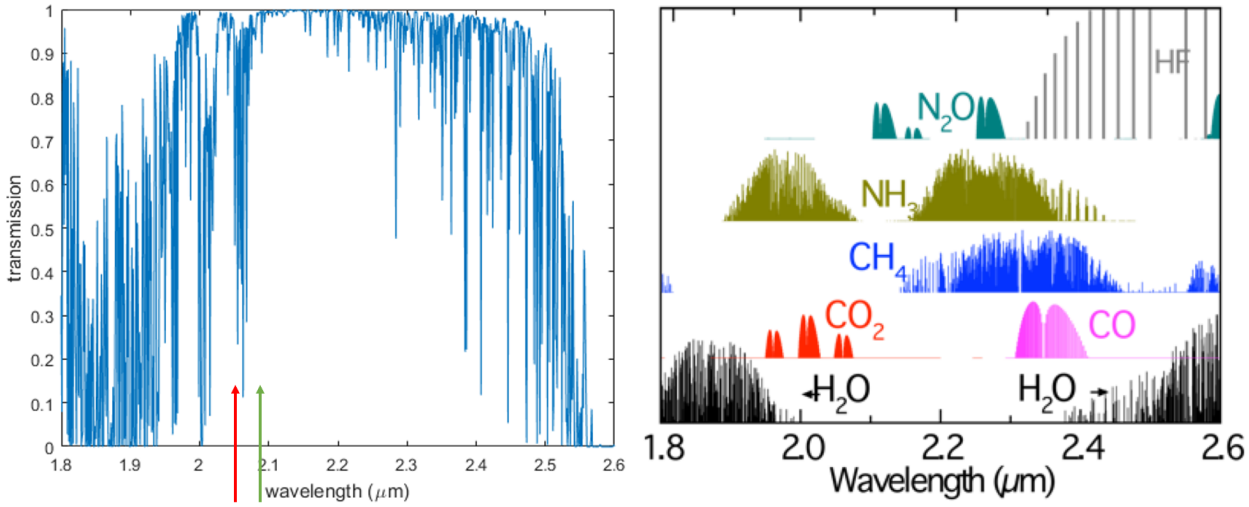

(a) **(b)**

Figure 1.2: (a) Spectral atmospheric transmittance due to absorption through a vertical column of the atmosphere. CO_2 absorption line at 2.05 μm (red arrow). Transparency at 2.09 μm (green arrow). Generated with data from [15]. (b) Absorption lines of atmospheric gases within the $2-2.5$ μm window. Appended from [16].

In addition to demands on the laser signal wavelength λ_s, LiDAR applications require laser sources to be robust, light weight, non-complex, operatable at room temperature and to provide pulses tailored to the specific LiDAR task. Tailoring a pulse implies specifying the pulse parameter which directly determines the abilities of the LiDAR. The pulse duration Δt governs resolution of range ΔR [17, p. 241]. The repetition rate f_{rep}, or the frequency at which a pulses are transmitted sets an upper limit to maximal measurable range R_{max} [18]. The energy of the pulse determines how close to R_{max} the LiDAR can reach [3].Laser sources which are tunable, and easily controllable in these parameters are advantageous [5] as they may serve several LiDAR applications.

Laser systems combining doped optical fibers and semiconductor laser diodes (LDs) meet the above listed demands on laser sources for LiDAR within the 2-2.5 μm atmospheric windows on for several reasons. Optical fibers are robust, light weight and self-containing waveguides [12]. When doped with ions, optical fibers can act as fiber lasers or amplifiers within the wavelength range of positive dopant ion gain [19]. Driven by telecommunication industry, Erbium-doped fiber lasers and amplifiers are well developed around 1.5 μm [20]. Thulium-doped fiber lasers have attracted a lot of attention in the last decade [21], and have provided milliJoule nanosecond pulses at 2.05 μm [22]. Holmium-doped fiber amplifiers and have been demonstrated between $2-2.1$ μm[23]. LDs are compact, lightweight and available up until 2.7 μm [24]. Electronically controlled, they allow directly setting pulse peak power, pulse duration down to 86 ps [25] as well as tune wavelength in a certain range [26]. LDs below 1600 nm are powerful enough to pump fiber lasers or fiber amplifiers [23]. However, in the spectral range above 1.9 μm they do not surpass 15 mW peak power [27]. However, LD power can be boosted by a fiber amplifier. Such a configuration is an example of a master oscillator power amplifier (MOPA), where the master oscillator is the LD, but could just as well be a fiber laser [7]. MOPA configurations have also been reported on to show pulse shortening during amplification [28].

The aim of this thesis is to develop a light-weight, compact, pulsed laser source based on Holmium-doped fiber and semiconductor LDs, and to show the the possibilty of such a laser source to be used for LiDAR applications within the 2 - 2.5 μm atmospheric window. The laser operated at 2.09 μm (green arrow in Figure 1.2a) could be promising for ranging applications and at 2.05 μm (red arrow in Figure 1.2a), for sensing of CO2 or ranging applications. Specifically, this aim will be achieved by completing four goals:

1. Charactere the optical output properties of a semiconductor LD tunable in wavelength around 2.05 μm.

2. Build an all-diode-pumped, holmium-doped fiber power amplifier, capable of amplifying laser sources in the

2-2.1 μm range, and develop a complementary numerical model of the amplifier.

3. Demonstrate the power amplifier by integrating it in a MOPA system with the LD as master oscillator, and also in a MOPA with an available mode-locked holmium-doped fiber laser emitting at 2.09 μm as master oscillator.

4. Carry out a proof of principle range-finding experiment with a LiDAR setup where an above named MOPA is the laser source.

This thesis is structured in the following manner: **Chapter 2** gives background theory on lasing in fibers and LDs as well as principles of range finding. **Chapter 3** presents the experimental setup of the MOPA and LiDAR systems. Chapter 4, 5 and 6 deal with the MOPA systems, where **Chapter 4** presents MOPA laser component characteristics. **Chapter 5** describes the designing of the power amplifier, and the complementary numerical model. **Chapter 6** provides the experimental results and discussion on the demonstration of the power amplifier. Chapter 7 and 8 deal with the LiDAR system, where **Chapter 7** describes the implementation of the LiDAR setup, and **Chapter 8** gives the experimental results and discussion of a range-finding LiDAR experiment. In **Chapter 9** conclusions are drawn. Finally, two appendices are included, where **Appendix A** presents the design and results of a time-dependent numerical model for a planned 2^{nd} stage power amplifier, and **Appendix B** shows how the LD could be implemented as the laser source of a CO_2 monitoring DIAL at 2.05 μm.

Chapter 2

Theoretical background

This chapter addresses relevant theory useful for understanding how a fiber lasers and amplifiers as well as LDs operate, and how laser properties are utilized in remote sensing. The theory chapter does not aim at being a comprehensive study of the field. Examples are chosen which are relevant for this thesis.

First general properties of laser light are introduced, next follows a short introduction to optical fibers. Then amplification of light in a medium is considered, first in fibers and then in the case of semiconductor diodes. Lastly general principles of remote sensing with emphasis on range finding are introduced.

2.1 Laser and properties of laser light

The core principle behind laser technology, is stimulated emission of photons. Under stimulated emission, photons are "cloned", producing coherent monochromatic light. Light is coherent when the photons are all in phase. Light is monochromatic when the photons all have the same wavelength or frequency [29, p. 2].

There are several sources of incoherent radiation, for example sunlight or thermal radiation. The novelty of lasers lies in their ability to produce highly coherent light, allowing them to tailor collimated beams of short pulses or continuous monochromatic light.

This section defines lasers and lasers amolifers and lookes at laser properties such as pulse

2.1.1 Definition of LASER

A LASER (Light Amplification by Stimulated Emission of Radiation) is an acronym for the process of creating highly coherent monochromatic light. Laser is also used for the devices creating laser light (laser oscillator) or amplifying laser light (laser amplifier) [30].

Figure 2.1 illustrates the three main aspects of a laser oscillator [29, p. viii]:

- an active medium
- a pumping source of energy
- an optical resonator

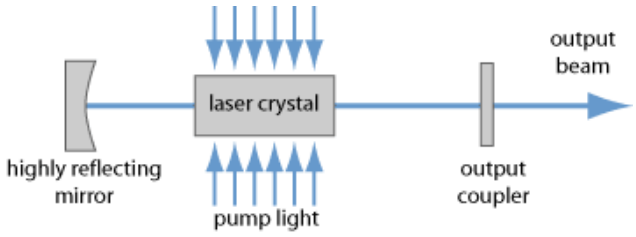

Figure 2.1: The main components of a laser oscillator generating laser light (output beam) consist of an active medium(crystal), pump energy source (pump light) and a resonance chamber (between the highly reflecting mirror and the partially transmitting output coupler). Appended from [30].

Firstly, the active medium is a system which may exist in different quantum energy states. For example a crystal containing ions which may be exited to higher quantum energy states (or levels), or a semiconductor heterostructure with electrons and holes which occupying states in the conduction and valence energy bands.

Secondly, a pump energy source must excite the system to a higher state and thereby store energy in the system. Continuing with the examples, the ions in the crystal may absorb photons and be excited (pumped) to a higher level. In the semiconductor, an electric current injects electrons into the conduction band and holes into the valence band. The stored energy is released through stimulated emission of photons, where an incident photon with lasing frequency ν corresponding to the energy difference between the upper and lower laser level, respectively stimulates the ions in the crystal to deexcite, or an electron-hole-pair in the semiconductor to recombine. In both examples two photons, identical to the incident photon, are emitted.

Thirdly, a resonance chamber or cavity, typically a set of mirrors placed on either side of the crystal in a conventional solid-state laser, or the polished facets of the semiconductor providing optical feedback. Such photons travel forth and back several times between the mirrors, increasing in number by every passing of the gain medium. One mirror is partially transmitting, and coherent monochromatic laser light may be outputted.

Laser amplifiers and laser oscillators are similar in that they channel energy from a pump source into amplifying a signal by way of stimulated emission. They differ, because amplifiers enhance an already existing signal provided as input, whereas the laser oscillator must itself be the source the signal. A Master Oscillator Power Amplifier (MOPA) is a system combining the laser oscillator and amplifier. A master oscillator provides the signal, and the power amplifier strengthens it [31].

2.1.2 Spectral linewidth and pulse duration

Due to interactions in the system, the upper and lower energy levels split into several sublevels [32, p. 341]. Thus, photons within a frequency width $\Delta\nu$ around the main lasing frequency ν may all be amplified. Even though this produces a spectrally broad train of photons, the term light at frequency ν is still being used [32, p. 286].

Pulsed lasers are designed to emit pulsed optical signals with pulse duration Δt. $\Delta\nu$ and Δt are respectively the full width half maximum (FWHM) of the spectral or temporal intensity profiles of the pulse [33, p. 9]. Following Heisenberg uncertainty relation [33, p. 10]

$$\Delta\nu\Delta t \geq \text{constant}, \tag{2.1}$$

the spectral width $\Delta\nu$ will fundamentally limit how short in duration Δt the signal can be, and vice versa. The constant of Equation 2.1 depends on the temporal intensity profile of the pulse [33, p. 10]. Therefore, light is only truly monochromatic ($\Delta\nu \to 0$) if it is continuous in time implying that $\Delta t \to \infty$. Continuous wave (CW) laser systems, can be viewed as emitting pulses of very long Δt, and have a close to monochromatic emission. The shorter in time the pulse is, the wider must the frequency spectrum be, although the spectrum can still peak at the main lasing frequency.

The optical spectrum can alternatively be described by wavelength λ. λ is related to frequency ν by the speed of light c in a medium [32, p. 7],

$$c = \lambda\nu\,. \tag{2.2}$$

The spectrum of a pulse (centered at wavelength λ), will then have a width $\Delta\lambda$ (linewidth) [34],

$$\Delta\nu = c\frac{\Delta\lambda}{\lambda^2}\,. \tag{2.3}$$

Thus, inserting Equation 2.3 in Equation 2.1, the pulse duration-linewidth product (or time-bandwidth product) of a pulse centered at wavelength λ is transform limited by [34]

$$c\frac{\Delta\lambda}{\lambda^2}\Delta t \geq \text{constant}\,. \tag{2.4}$$

2.1.3 Divergence of laser beams

Coherent light exiting a cavity or waveguide will be subject to diffraction due to uncertainty in momentum and position. How wide the beam spreads out (diverges) depends upon the geometry of the exit, but also the beam quality of the light [32, pp. 286-287]. Beams with a Gaussian spatial intensity profile, are the least divergent [32, p. 307], diverge at an angle [32, p. 309]

$$\theta = \frac{\lambda}{\pi D/2}, \tag{2.5}$$

where D is diameter of the waveguide exit. Gaussian beams may to a good approximation be obtained in single-mode fibers [35].

2.2 Aspects concerning optical fibers

Optical glass fibers are widely used in telecommunications. They act as waveguides, and if doped, also act as an active media for a laser activity [36].

This section introduces general aspects on fibers by first considering them as waveguides. Then relevant fiber types are presents, and finally doped fibers introduced.

2.2.1 Fiber structure

A basic fiber structure may be seen in Figure 2.2a. It has a cylindrical symmetry with a silica glass (SiO_2) core and cladding of respective diameters d_{core} and d_{clad}, and refractive index n_{core} and n_{clad}. Glasses differ from crystals in that they are amorphous [36], whereas crystals are periodic. Crystal SiO_2 is better known as quartz. The fiber is finally protected by a polymer coating. The refractive index profile is shown in Figure 2.2b. The step-index enables the fiber to act as a waveguide. The fiber cylindrical geometry, provides a high surface to volume ratio allowing for easy dissipation of heat compared to rod shaped solid state crystal lasers [37].

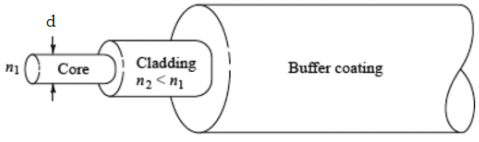

(a) The structure of a single clad fiber, showing the inner core, cladding and polymer coating. The notation for refractive indices used is $n_1 = n_{core}$ and $n_2 = n_{clad}$. Appended from [38].

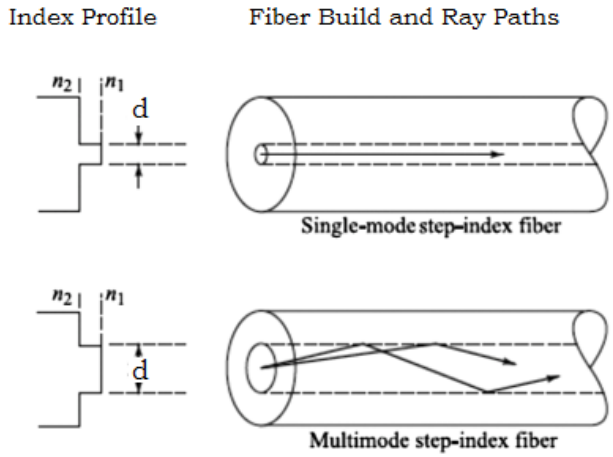

(b) Two step refractive index fibers. Depending on the diameter of the core, the fiber is either single-mode supporting one spatial mode, or multi-mode supporting several spatial modes. The notation for refractive indices used is $n_1 = n_{core}$ and $n_2 = n_{clad}$. Appended from [38].

Figure 2.2

2.2.2 Fiber optical modes and modal dispersion

The fiber as a waveguide may support several spatial modes of a ray with given wavelength λ. A spatial mode m is characterized by the angle θ_m at which the beam propagating in the core is incident on the boundary between the core and the cladding [32, p. 50]. According to Snell's law, the beam will experience the total internal reflection effect if this angle is greater than $\arcsin(\frac{n_{clad}}{n_{core}})$ [32, p. 11]. Because no power escapes into the cladding, one can say that the fiber maintains this mode, by letting all the power continue down the fiber. In a cylindrical geometry the number of maintained modes for a given wavelength λ and core diameter d_{core} depend on the V parameter of the fiber defined as [39]

$$V = \frac{2\pi}{\lambda} d_{core} \mathrm{NA}\,, \tag{2.6}$$

where the numerical aperture (NA) [40]

$$\mathrm{NA} = \frac{1}{n_0}\sqrt{n_{core}^2 - n_{clad}^2} \tag{2.7}$$

is the parameter typically provided by the fiber producer. Here n_0 is the refractive index of the medium surrounding the fiber.

Single-mode fibers

When

$$V < 2.405 \tag{2.8}$$

the fiber core only maintains a single transverse mode, namely the one propagating straight down the fiber, always parallel to the walls [32, p.49]. Thus the fiber is said to me single-mode. For larger V, several transverse modes are supported by the fiber, and the fiber is called multi-mode. As seen from Equation 2.6, the single mode may be obtained by narrowing the diameter of the core d_{core}. A single mode is favourable because it offers no modal dispersion, in the sense that all photons of the same wavelength will travel the same distance and arrive in phase at the end of the fiber [20]. Wave packets are also subject to chromatic dispersion, which will be discussed later.

Polarization maintaining (PM) fibers

Additional structuring in the cladding of a single-mode fiber introduces a birefringent axis in the plane normal to the propagation axis, making the fiber polarization-maintaining (PM) [41]. Linear polarized light with polarization aligned with the birefringent axis will maintain its polarization, even if the fiber is bent or experiences other forms of stress. PM fibers are examplewise useful for constructing interferometers.

2.2.3 Doped fibers

A pure silica fiber (passive fiber) only acts as a waveguide. Introducing dopant ions in the host material (silica) makes the fiber an active fiber; a gain medium with the ability to amplify signals. Dopant ions are chosen by considering the energy levels, revealing possible energy transitions, and hence which wavelengths may be amplified [19]. Energy spectra of typical rare earth ions, with that silica fibers may be doped with, are shown in Figure 2.3.

Next, holmium-doped silica fiber and its properties will be considered as a relevant example.

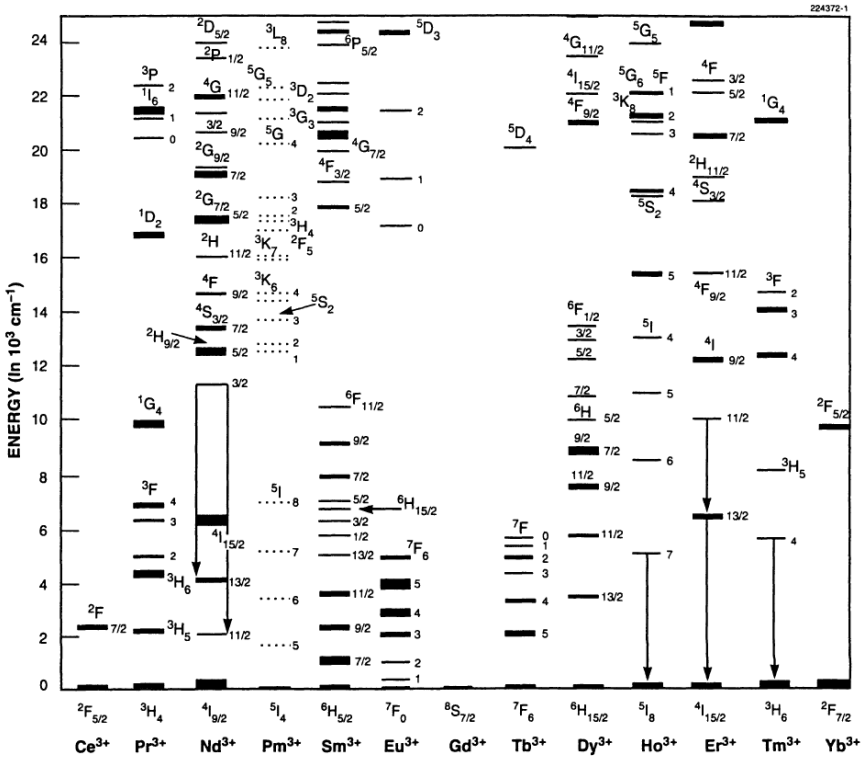

Figure 2.3: Energy levels of rare earth ions. Appended from [42].

Energy levels and absorption spectrum of holmium-doped silica fiber

The lower energy levels of holmium Ho^{3+}-ions in glass fiber as seen in Figure 2.3 are labelled ${}^5I_x$, where x is the level indexes. Possible transitions between these levels become apparent in an absorption spectra shown in Figure 2.4. Holmium absorbs both in the visible at 550 nm and 650 nm, and in the infrared around 1150 nm and between 1800 nm and 2200 nm.

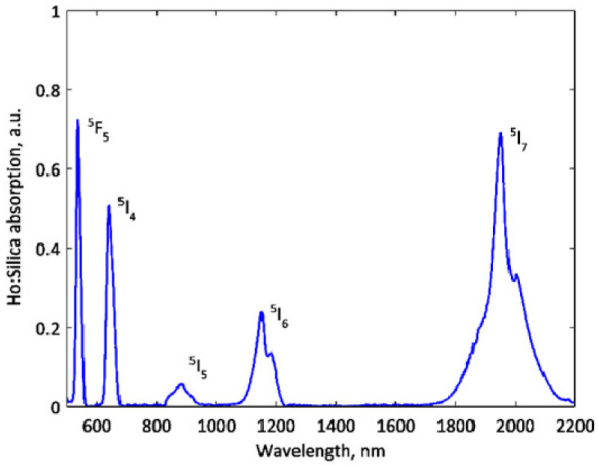

Figure 2.4: Absorption at different wavelengths of holmium-doped silica fiber. The corresponding energy levels ${}^5I_x$ are marked. Appended from [23].

2.3 Optical fiber power amplifiers

So far, general trademarks of laser oscillator devices and the possibilities of doped optical fibers as a gain medium have been introduced.

This section deals with how active fibers act as optical amplifiers by accommodating the transfer of energy from a pump energy source into the signal to be amplified. It gives a short introduction to how light interacts with matter. Rate equations coupling the intensity of the signal with the population of energy levels are outlined. It then considers which frequencies may be amplified by the gain medium, and how this gain depends on the pump and signal input powers and the doping concentration. Quasi-three-level schemes are discussed. It closes with efficiency, total gain and limitations on the fiber amplifier.

2.3.1 Optical interaction with matter

Consider a gain medium of N ions, which may occupy one of two energy levels labeled 1 and 2 with respective energies E_1 and E_2. Let N_1 and N_2 be the number of ions in each energy state. Photons of energy $h\nu = E_2 - E_1$, where h is Planck's constant, may interact with the gain medium by being absorbed, emitted spontaneously or emitted through stimulated emission. The rate at which the population of the upper level changes is closely linked to the rate at which the flux of photons changes. The three processes are shown in Figure 2.5, and will be considered separately based on [29, pp. 1-3].

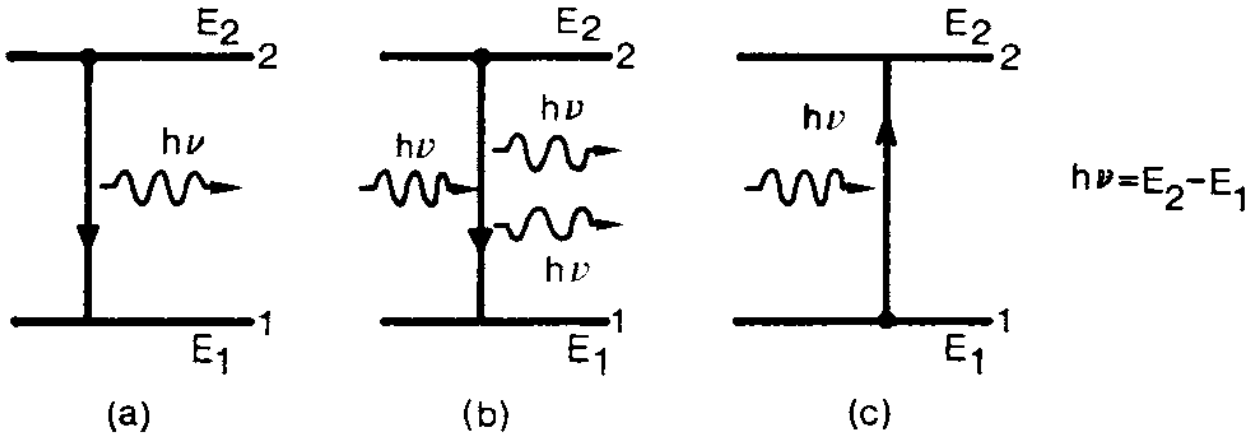

Figure 2.5: Transitions (a) spontaneous emission (b) stimulated emission (c) absorption between two energy levels E_1 and E_2 of a system through interaction with photons of energy $h\nu = E_2 - E_1$. Appended from [29, p. 2].

Spontaneous Emission

An ion in the excited state will after a certain time τ_{sp} spontaneously relax into the ground state, releasing the energy as a photon with a random phase and spatial direction, and changing the upper level population N_2 at a rate

$$\left(\frac{dN_2}{dt}\right)_{sp} = \frac{1}{\tau_r} N_2, \tag{2.9}$$

where τ_r is the radiative (spontaneous) lifetime of the upper level.

Stimulated emission and absorption

When the relaxation from the upper state into the ground state is induced by an incoming photon(spontaneous emission), the upper level population changes according to

$$\left(\frac{dN_2}{dt}\right)_{st} = -W_{21}N_2, \tag{2.10}$$

where W_{21} is the rate at which this process occurs. Stimulated emission is amplification, because it turns one photon into two identical photons. Similarly, an ion in the ground state may be elevated to the excited level, changing the upper state population at a rate

$$\left(\frac{dN_2}{dt}\right)_{a} = W_{12}N_1, \tag{2.11}$$

where W_{12} is the rate at which this process occurs. Absorption of the pump power is storing energy in the system. Absorption of the signal power may be seen as a loss.

Following Fermi's Golden Rule [32, p. 353], the rate of transitions W_{ij}, where $ij = 12$ or $ij = 21$, will be proportional to the number of incident photons $\frac{I}{h\nu_{ij}}$ with the frequency ν_{ij} corresponding to the transition, in a beam of light with intensity I, and given by

$$W_{ij} = W_{ij}(\sigma_{ij}, I) = \frac{\sigma(\nu_{ij})I(\nu_{ij})}{h\nu_{ij}}. \tag{2.12}$$

Where σ_{ij} is the proportionality constant for the transition ij, and will later will be introduced as the cross section of this transition.Fermi's golden rule couples the flux of photons, with frequency corresponding to the transition ij, to the level populations.

Non-radiative transitions

It should also be mentioned that excited ions can interact with phonons (lattice vibrations) and non-radiative transitions from higher to lower levels may take place at a rate $\frac{1}{\tau_{nr}}$, where τ_{nr} is the non-radiative lifetime of the upper level. The energy released contributes to heating in the fiber.

$$\left(\frac{dN_2}{dt}\right)_{nr} = -\frac{1}{\tau_{nr}}N_2, \tag{2.13}$$

describes the corresponding change in upper level population N_2.

2.3.2 The cross section σ

Equation 2.12 defines the the cross section as the proportionality constant between gain and population inversion [32, p. 351]. The cross section may be interpreted as the area seen by an incoming photon in which it will be affected by the potential of the ion.

Due to Stark splitting [32, pp. 340-342], the cross sections for absorption and emission at a particular wavelength are different. When placed in an environment (for example glass fiber), the ions are affected by the surrounding crystal field, and every degenerate level splits into a multiplet or manifold of sublevels. For Holmium in silica fiber, ${}^5I_x$ are such manifolds, where x indexes the level. A possible splitting may be imagined as shown in Figure 2.6. Here, the energy difference between the lowest states in the two manifolds is ε. One can define the absorption cross section $\sigma_{abs}(\nu)$ as the cross section of absorption of a photon with frequency ν from all sublevels of the ground level 1 to all sublevels of the exited level 2. And likewise for the emission cross section $\sigma_{em}(\nu)$.

Ions will tend to relax to the lowest possible sublevel of the manifold they occupy. Photons of smaller energies (longer wavelengths) are required to stimulate emission from the lowest upper level to the highest lower level. And

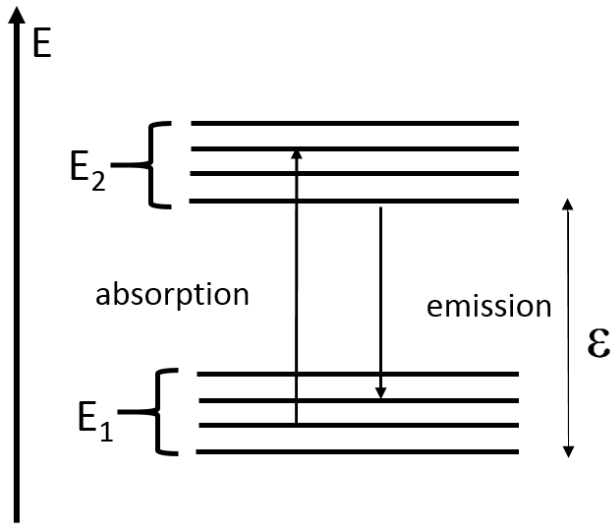

Figure 2.6: Due to the environment(for example fiber glass), the energy levels E_1 and E_2 each split into a manifold of sublevels with an average energy difference ε. Shorter wavelength photons are more likely to be absorbed by ions in the lower level. In the upper level, ions relax to the bottom of the level. Reproduced from [32, p. 341].

conversely photons of larger energies (shorter wavelengths) must be absorbed to excite ions from the lowest ground state level to the upper level. σ_{abs} will be larger at shorter wavelengths and σ_{em} larger at longer wavelengths. The McCumber relation relates the spectral shift between the the two cross sections [32, p. 341]

$$\sigma_{abs}(\nu) = \sigma_{em}(\nu) e^{\frac{h\nu-\varepsilon}{k_B T}}, \tag{2.14}$$

where k_B is Boltzmann's constant, and T is the temperature.

The cross section spectra in a particular crystal or glass fiber environment may be found in the literature [43], and were plotted in Figure 2.7 for Ho^{3+} ions in silica glass fiber. The Stokes shift is recognized in the plot of the absorption σ_{abs} and emission σ_{em} cross sections as the distance between the two peaks [32, p. 438].

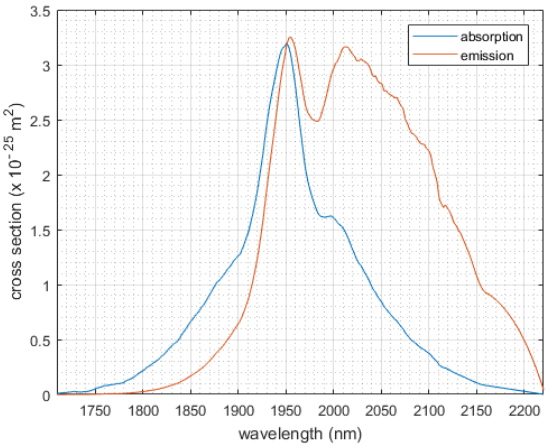

Figure 2.7: Absorption (blue) and emission(orange) cross sections of Ho^{3+} in silica. Plotted after data from [43].

2.3.3 Quasi-Three-Level systems

The two lasing levels so far introduce the lower laser level. Generally, lasing cannot be achieved in the two-level system, because the sufficient population inversion may not be obtained [29, p. 6]. In lasers additional levels, between which absorption of pump photons happen, are used. One possible system, the quasi-three-level laser, is relevant for lasing action between the three lower energy levels of holmium in silica fiber [42] which are shown in Figure 2.8. The levels ${}^5I_8$, ${}^5I_7$ and ${}^5I_6$ are given extra labels 1, 2 and 3.

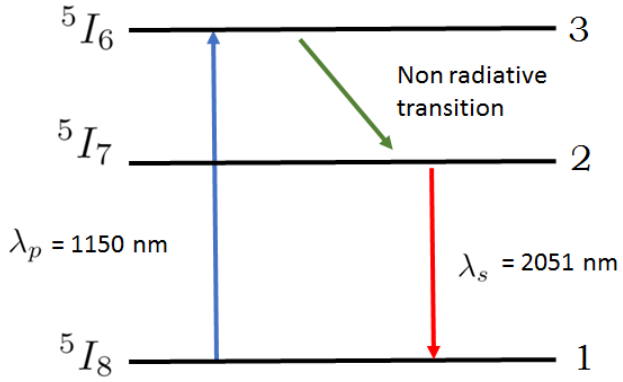

Figure 2.8: The three lower energy levels of holmium in silica fiber relevant for lasing action. Here shown with a pump source at 1150 nm and a signal to be amplified at 2051 nm.

The quasi-three-level model makes some assumptions, as presented in [42]. The ground level multiplet ${}^5I_8$ or 1, of population N_1, contains both the lower lasing level and the ground state. The lower lasing level is already thermally populated at room temperature. Ions may be pumped from the ground state to an upper pump level ${}^5I_6$ or 3 of population N_3, by absorbing a photon from the pump source of wavelength λ_p. Although the levels 3 and 2(${}^5I_7$) are separate, it is assumed that the non-radiative lifetime τ_{nr} of level 3 is much shorter than the time before a spontaneous relaxation or stimulated emission back into the ground state. Hence, the population N_3 of level 3 is assumed to be zero, and any absorption of pump photons by ground state ions contribute to the population N_2 of the upper laser level manifold 2. The energy released in the non-radiative transition between level 3 and 2 is dissipated as heat in the medium. Allowed interactions between level 2 and 1 are assumed to be spontaneous and stimulated emission of photons with the signal wavelength λ_s.

Under these assumptions, keeping in mind Fermi's golden rule (Equation 2.12), upper laser level population changes with contributions from Equation 2.9 for transitions $2 \rightarrow 1$, Equation 2.10 for transitions $3 \rightarrow 1$ and $2 \rightarrow 1$, and Equation 2.11 for transitions $1 \rightarrow 3$ and $1 \rightarrow 2$, according to

$$\left(\frac{dN_2}{dt}\right) = -\frac{1}{\tau_{21}}N_2 - \frac{\sigma_{em}(\lambda_s)I_s}{h\lambda_s}N_2 - \frac{\sigma_{em}(\lambda_p)I_p}{h\lambda_p}N_2 + \frac{\sigma_{abs}(\lambda_s)I_s}{h\lambda_s}N_1 + \frac{\sigma_{abs}(\lambda_p)I_p}{h\lambda_p}N_1 \tag{2.15}$$

where I_s and I_p are the intensity of signal and pump light. Where τ_{21} is the radiative lifetime of the $2 \rightarrow 1$ transition. Finally, number of upper and lower state ions must be conserved and equal the total doping ions N according to,

$$N = N_1 + N_2. \tag{2.16}$$

Equation 2.15 is a simplification, as it only includes a limited number of transitions, but is relevant for a certain range of parameters. It is illustrative in seeing how signal and pump photon fluxes are coupled with level populations.

2.3.4 Gain and Amplification

So far, changes in level populations in interaction with light have been looked at. Switching point of view, changes in light intensity in interaction with a gain material is considered, and are outlined in this section assuming the quasi-three-level model, and following [32, pp. 337-340].

At a point x in the fiber the change in upper and lower populations $\Delta(N_2 - N_1)$ will emit a flux of photons with energy $h\nu\ \mathrm{d}N_2$. Propagating down the fiber at a speed c, this will correspond to a change in light intensity $\mathrm{d}I$ of

$$\mathrm{d}I = c\ h\nu\ \mathrm{d}(N_2 - N_1). \tag{2.17}$$

In a time $\mathrm{d}t$, the light will travel a distance

$$\mathrm{d}x = c\,\mathrm{d}t \tag{2.18}$$

along the fiber. Dividing Equation 2.17 by Equation 2.18 one obtains

$$\frac{\mathrm{d}I}{\mathrm{d}x} = h\nu\frac{\mathrm{d}N_2}{\mathrm{d}t}. \tag{2.19}$$

Applying Equation 2.10 and Equation 2.11, assuming the contribution of spontaneous emission to be much weaker than the stimulated emission, together with Fermi's golden rule (Equation 2.12), one obtains

$$\frac{\mathrm{d}I}{\mathrm{d}x} = I(N_2\sigma_{em} - N_1\sigma_{abs}), \tag{2.20}$$

valid at time t and point x in the fiber for signals of wavelength λ. Equation 2.20 defines the gain γ as

$$\gamma(\lambda, x, t) = N_2(x,t)\sigma_{em}(\lambda) - N_1(x,t)\sigma_{abs}(\lambda), \tag{2.21}$$

which in words is the fraction with which light intensity changes per distance propagated in the fiber. Here the properties of the single dopant ion are contained in the cross sections σ_{em} and σ_{abs} whereas the information about the population densities is contained in N_2 and N_1.

$N_2\sigma_{em}(\lambda)$ accounts for stimulated emission and amplification of the light, whereas $N_1\sigma_{abs}(\lambda)$ is due to absorption and thus attenuation of light intensity. If there is net amplification, then

$$\gamma(\lambda, x, t) > 0, \tag{2.22}$$

and the flux increases. This is the amplification criterion, which is desirable for signal wavelengths λ_s. Conversely, gain fulfilling the absorption criterion

$$\gamma(\lambda, x, t) < 0 \tag{2.23}$$

leads to an decreases in flux, and is mostly desirable for pump light wavelengths λ_p, but can be relevant for signal wavelengths as well.

Equation 2.20 and Equation 2.15 form a coupled set of equations, which may be solved numerically [32, p. 477].

Effective cross sections

At a given wavelength λ, cross sections are constant and tabulated. Therefore, N_2 in comparison with N_1, related through Equation 2.16 determine if gain is positive or negative a this λ. To see which upper state populations are needed for positive gain, it is useful to define the effective cross section σ_{eff} as

$$\sigma_{eff} = \frac{\gamma}{N} = n_2\sigma_{em}(\lambda) - (1 - n_2)\sigma_{abs}(\lambda), \tag{2.24}$$

where the fractional populations of the upper n_2 and lower n_1 manifolds have been defined as

$$n_2 = \frac{N_2}{N} = 1 - n_1. \tag{2.25}$$

Now, σ_{eff} may be plotted for for different values of n_2. Curves showing $\sigma_{eff} > 0$ indicate where a certain upper level population fraction n_2 provides positive gain. Such σ_{eff} curves are plotted in Figure 2.9 for holmium in silica fiber using the σ_{em} and σ_{abs} from Figure 2.7. Since, having n_2 requires a certain pump power, the intersection of the curves with $\sigma_{eff} = 0$ indirectly defines the threshold pump intensity or also power $P^{in}_{p,th}$ for every wavelength λ.

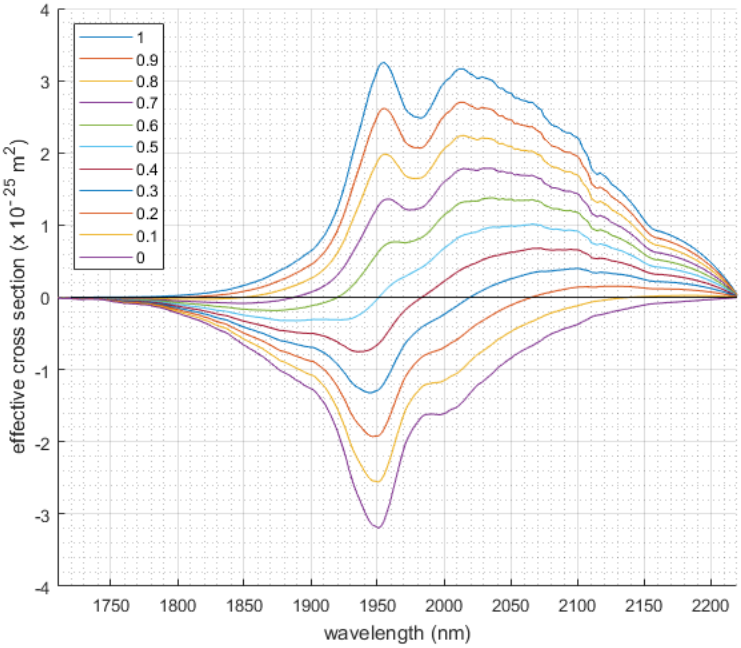

Figure 2.9: Effective cross section of holmium (Ho^{3+}) in silica fiber plotted for different upper laser levels populations n_2. Plotted after data from [43].

Notable is, firstly, that the fractional population of the entire upper manifold n_2 varies with position x in the fiber, and in short-pulsed regimes with time t, and so the relevant curve in Figure 2.9 for a signal of wavelength λ is also time dependent, and varies along entire fiber. Secondly, n_2 smaller than 0.5 (not population inversion between the upper and lower manifolds), nevertheless provides positive gain. This is not a contradiction to the requirement of population inversion, because all sublevels spaced hv apart within the manifolds obtain population inversion.

2.3.5 A steady-state solution or time independent gain

Consider a doped fiber, continuously pumped by an energy source causing ions to be excited and installing a population inversion. Then, at a certain point in time, a pulsed signal enters the fiber, and propagates down it while deexciting the ions and gradually getting more intensive. This would be a situation where the pulse was a disturbance to the equilibrium, and gain γ would be dependent on time.

Conversely, if the signal is continuously fed into the fiber, a new equilibrium in population densities at every point in the fiber is established (Equation 2.15 = 0). Then gain is independent of time, and a steady state may be assumed

to take place. The steady-state solution simplifies the calculations of pump intensity and signal intensity in the fiber.

According to [44], the steady-state solution may as an approximation also be applied to a pulsed signal, under the following conditions:

1. The pulse energy must be under the saturation energy E_{sat} of the amplifier. E_{sat} corresponds to where the gain of the amplifier reduces with $1/e$ and is given [45]

$$E_{sat} = A\frac{h\nu_s}{\sigma_{em}(\nu_s)+\sigma_{abs}(\nu_s)} \tag{2.26}$$

   where A is the mode area of the pulse. Conversely, in very intensive pulses where the energy of the front exceeds E_{sat}, the front deexcites enough ions, such that the end of the pulse will see very different level populations, and thus experience a different gain, which may lead to pulses shortening in duration [28].

2. The wavelength bandwidth of the pulse must be narrow enough, so that all wavelength components constituting the pulse approximately have the same gain.

3. The optical spectrum of the pulse must also not broaden significantly during amplification.

So far, the pump and signal intensities have been considered. However, for measurement purposes signal and pump power may be the useful quantity. In fibers which are long cylinders, power P relates to intensity I [32, p. 427]

$$P = \frac{\pi d_{core}^2}{4} I, \tag{2.27}$$

where $\frac{\pi d_{core}^2}{4}$ is the core area.

The power of the pulsed signal when modelled as a continuous signal will be its average power P_{avg},

$$P_{avg} = P_{peak}\frac{\Delta t}{T_{rep}}, \tag{2.28}$$

where

$$E_{pulse} = P_{peak}\Delta t \tag{2.29}$$

is defined to be the pulse energy E_{pulse} of a pulse with peak power of P_{peak} and pulse duration Δt. T_{rep} is the time period between two successive pulses enter the fiber, but also the time between a pulse is emitted fromthe fiber. The period T_{rep} is related to the repetition rate f_{rep} via,

$$f_{rep} = \frac{1}{T_{rep}}\ . \tag{2.30}$$

2.3.6 Optical-to-optical efficiency, slope efficiency and total gain

Having solved the coupled Equation 2.20 and Equation 2.15 by applying a steady-state or time-dependent approach for given input pump power P_p^{in} and input signal power P_s^{in}, one generally looks at the output pump power P_p^{out} and output signal power P_s^{out}. A probable relationship between P_s^{out} varying P_p^{in}, for a given P_s^{in} is included in Figure 2.10. The laser outputs signal above a threshold input pump power $P_{p,th}^{in}$ already introduced in subsection 2.3.4. To evaluate performance of an optical amplifier, the parameters optical-to-optical efficiency η, slope efficiency η_s and total gain G based on P_p^{in}, P_s^{in}, P_p^{out} and P_s^{out} are defined.

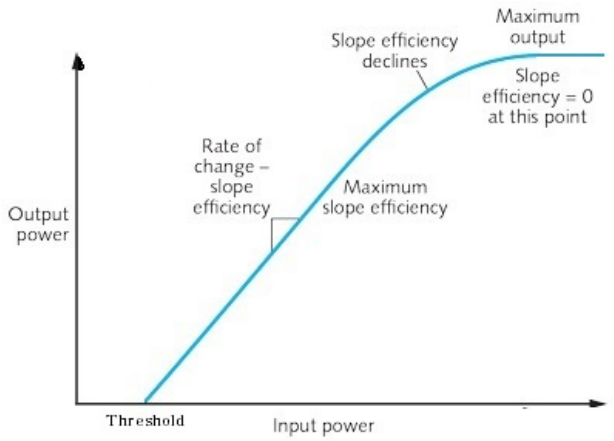

Figure 2.10: Typical shape of output power to pump power curve. The curve slope is the slope efficiency. Appended from [46].

Total gain G and slope efficiency η_s

The total gain G [32, p. 477] of the amplifier defined as

$$G = \frac{P_s^{out}}{P_s^{in}}, \tag{2.31}$$

When convenient, G may be expressed in decibel dB

$$G = 10\log(\frac{P_s^{out}}{P_s^{in}}) \text{ dB}. \tag{2.32}$$

The slope efficiency η_s [32, p. 373] indicates the incremental increase in signal power produced by an additional increment in pump power, and is defined as

$$\eta_s = \frac{dP_s^{out}}{dP_p^{in}}. \tag{2.33}$$

By observing Figure 2.10 the maximum slope efficiency(and therefore maximum profit in gain by paying more input power) is found in the linear regime right after threshold.

Due to the finite number of doping ions in the fiber, the fiber will after a certain pump power be transparent to the pump light. This effect is called absorption saturation. At such pump powers, all the ions are excited out of the ground state. This will be reflected in a flattening out of the signal output intensity and a decrease in slope efficiency as seen in Figure 2.10. Flattening of signal output intensity also implies flattening of total gain as seen from Equation 2.31, assuming the input signal intensity remained unchanged.

Optical-to-optical efficiency η and the quantum defect

The optical-to-optical efficiency indicates what fraction of the total pump energy provided is converted into signal energy, and is here defined as

$$\eta = \frac{P_s^{out} - P_s^{in}}{P_p^{in}} \tag{2.34}$$

As seen in Figure 2.10, lowering the $P_{p,th}^{in}$ increases η, because the curve shifts to the left. Upon passing the thresh-

old, η increases with increasing pump power, but falls off approaching absorption saturation. Operating in the linear regime with a steep slope (i.e. a high η_s) leads to high optical-to-optical efficiency.

The remaining fraction $(1-\eta)$ of total absorbed pump power corresponds to losses of pump energy, in the form of dissipated heat in the fiber (or in the isolators P_p^{out}), splicers, impurities in the fiber structure [46]. Even when having perfect loss-less couplers, every ion excited by a pump photon undergoes a non-radiative transition from level 3 to level 2 [46], as exemplified in Figure 2.8 loosing an energy q to heat in the fiber, which may be written [47]

$$q = h\nu_p - h\nu_s = h\nu_p(1 - \frac{h\nu_s}{h\nu_p}) \tag{2.35}$$

Where $1 - \frac{h\nu_s}{h\nu_p}$ is the fraction of the pump power which is always lost. This is know as the quantum defect and sets the upper limit η_q to the optical-to-optical efficiency of the system,

$$\eta \leq \eta_q = \frac{h\nu_s}{h\nu_p} \tag{2.36}$$

This is the the best optical-to-optical efficiency you can hope to attain in a system. Because the pumping photons always are higher in energy than the signal photons, $\frac{h\nu_s}{h\nu_p} < 1$. Choosing pumping wavelengths closer to the signal wavelengths, thus increased η_q.

2.3.7 Limitations

Three factors limiting both the total amplification of the signal (gain) and thus the efficiency of the amplifier are Amplified Spontaneous Emission (ASE), reabsorption of signal power, and passive losses.

Amplified Spontaneous Emission (ASE)

Ions in the upper laser level relax to the lower laser level manifold according to Equation 2.9, and emit photons of wavelengths λ not in general equal to the signal wavelength λ_s. A laser amplifier has the natural disadvantage of also amplifying such parasitic signals fitting within the gain of the amplifier readable from Figure 2.9. This is the ASE effect [48], and lays claim on available pump power. Thus, ASE will be a loss of pump power with regard to amplifying the signal, and effectively lowers the optical-to-optical efficiency η of the amplifier and the total gain G of the signal. ASE is noise, which broadens the outputted optical spectrum of the amplifier. Such noise can be filtered out by placing optical filters at the end of the fiber.

Reabsorption

Absorption of signal photons by lower state ions, $N_1(x)\sigma_{abs}(\lambda_s)$, is termed reabsorption, and contributes negatively to the gain γ as seen from Equation 2.21. Reabsorption is generally avoided by choosing the signal wavelength λ_s should where $\sigma_{em}(\lambda_s)$ is high compared to $\sigma_{abs}(\lambda_s)$ [32, p. 439].

Passive losses

Both signal and pump power attenuates due to scattering off of impurities in the fiber, and due to absorption by the host material (silica glass) [32, po. 55-57]. These source of loss are passive losses.

2.4 Mode-locked fiber lasers

This sections includes some main principles on how mode-locked fiber lasers operate. The section is meant to support and enable a discussion on how mode-locked laser performs as master oscillator in a MOPA compared to other laser types. A more thorough introduction to mode-locked laser may be found in [29, p. 339-367].

A fiber amplifier distinguishes itself from a fiber laser in that it takes a laser signal and amplifies it to a stronger output, whereas the fiber laser is an oscillator, and generates the laser signal itself.

A mode-locked fiber laser operates according to the principles described in subsection 2.1.1, and consists of the three necessary laser components listed in subsection 2.1.1. Following [32, p. 425], the fiber is the waveguide cavity, bounded at either end by a fully reflecting and a partly transmitting component. These can be mirrors. The active medium is obtained by doping the fiber as explained in subsection 2.2.3. Holmium-doped fiber lasers would have the energy level structure shown in Figure 2.8. Finally, a pump energy source is coupled to the fiber.

Light in the holmium-doped fiber laser generally interacts with matter as described for holmium-doped fiber amplifiers in section 2.3. In the fiber laser however, the signal is initially generated by spontaneous emission from level 2 to level 1 in Figure 2.8, and the signal does not propagate through the fiber just once, as is the case for the amplifier, but oscillates forth and back between the mirrors, and is thus gradually amplified.

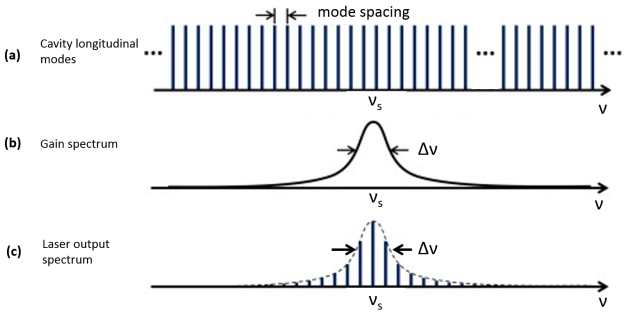

Figure 2.11: (a) The CW longitudinal modes supported by the geometry of the cavity. (b) Gain of the active medium. (c) The laser output spectrum of frequency linewidth $\Delta\nu$. Appended from [49].

The cavity length L determines which longitudinal single-frequency CW modes fit inside the cavity [32, p. 410]. These modes are shown in Figure 2.11a, and have a phase difference locked in time, hence a mode-locked laser. Furthermore, the gain material only supports the single-frequency modes, for which gain is positive and Equation 2.22 is fulfilled [32, p. 431]. The medium gain curve of frequency bandwidth $\Delta\nu$ [32, pp. 403-404] is drawn in Figure 2.11b. As gain is proportional to the effective cross section via Equation 2.24, the gain curve corresponds to the effective cross section curves shown in Figure 2.9 in the case of holmium-doped silica fiber. The modes, that fulfill both the cavity and gain medium requirements, are the lasing modes shown in Figure 2.11c. The lasing modes build a pulse circulating the cavity with frequency linewidth $\Delta\nu$ centered at the main lasing frequency ν_s labelled in Figure 2.11. $\Delta\nu$ is recalculatable to the $\Delta\lambda$ via Equation 2.2, and the pulse duration Δt is then found by Equation 2.1.

The period between when two consecutive pulses of light are emitted by the fiber cavity at the partly reflecting mirror is [32, p. 407]

$$T_{rep} = \frac{2L}{c} \,. \tag{2.37}$$

T_{rep} can be interpreted as the time it takes the circulating pulse to complete a round trip in the cavity, and be partly transmitted at the partly reflecting mirror [32, p. 407]. The corresponding repetition rate f_{rep} of the mode-locked laser is given by Equation 2.30.

Thus, the longer the cavity length L, the lower the repetition rate f_{rep} [32, p. 407]. The broader the gain medium bandwidth $\Delta\lambda$ or $\Delta\nu$, and the shorter the pulse duration Δt [32, p. 406].

The discussion on optical-to-optical efficiency, slope efficiency and threshold pump power for optical amplifiers in subsection 2.3.6 also apply to mode-locked lasers.

2.5 Semiconductor Laser Diodes

This section briefly elaborates on the laser diode (LD) introduced in subsection 2.1.1. Various methods of achieving wavelength selection are described. Finally how LDs allow control and monitoring of LD temperature is discussed.

2.5.1 Lasing in a LD

The LD is an electrically pumped laser oscillator. An example of a semiconductor LD may be seen in Figure 2.12, and is based on a semiconductor pin-junction in the z direction and a optical waveguide cavity confinement in the x and y directions. In the pin-junction, the p-doped and n-doped layers are often of the same semiconductor type, whereas the undoped intrinsic i-layer is a semiconductor of smaller band gap. This three layered heterostructure forms a quantum well. In the z direction the electrons and holes are confined in the i-layer between the n-end p-layers, but are free to move in the x and y direction, making them two dimensional.

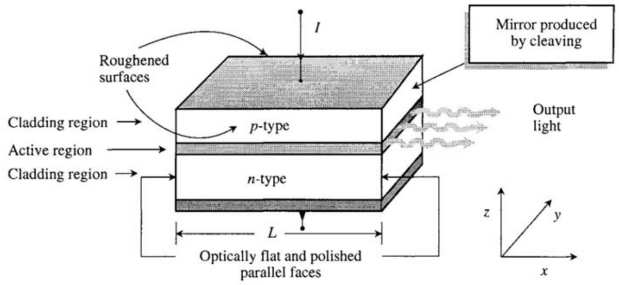

Figure 2.12: A simple semiconductor LD, an intrinsic semiconductor forms an active region by being sandwiched in the z direction between an n- and p-type of a semiconductor of larger band gap. A pumping current I injects holes and electrons into the active region, where they recombine. Mirrors at the end of the diode of length L in the x direction provide feedback, and selects the allowed wavelengths. Above the threshold current I_{th}, the recombination is stimulated, and amplified light of the specified wavelengths is emitted at one of the mirrors. Appended from [50, p. 246].

The conduction band is the equivalent of the upper laser level and the valence band the lower laser level. Forward biasing the diode injects electrons from the n-type side and holes from the p-type side into the quantum well. In the quantum well also called the active region, the holes and electrons may only take certain energy values. They will recombine and emit a photon with wavelength corresponding to the difference of these energy layers plus the energy gap of the i-layer semiconductor. Thus, the quantum confinement allows photons of longer wavelength than the band gap being emitted.

Let the x direction be the waveguide of length L, and set two mirrors at the ends. Such a waveguide is called a Fabry Perot chamber, and will only support wavelengths fitting in the length L [50, p. 245]. Spontaneously emitted photons of such wavelengths will start oscillating forth and back in the chamber. Further stimulating recombination of the electron and holes being injected into the active region. Thus the emitted spectrum of the LD is centered at the lasing wavelength λ_s determined by the quantum well and band gap structure, as well as the modes supported by the cavity length L.

Net amplification, or positive gain is obtained when the number of stimulated emitted photons exceed the ones lost by absorption in the walls of the cavity or escape through the end mirrors [50, p. 247]. This happens at a certain level of the pumping current termed the threshold current I_{th} of the LD. After this, the outputted light power at one

mirror end will increase linearly [32, p. 195] with the pump current. The light output may be coupled into a passive fiber. Fiber-coupled LDs can than easily be integrated in fiber laser or amplifier systems [51].

The two dimensionality introduced by the pin-junction increases the density of states at the band edges compared with the three-dimensional pn-junction, increasing the gain of the LD [32, p. 206]. It also reduces the reabsorption [32, p. 192]. Layering several quantum wells in the z direction creates a multiple quantum well (MQW) structure. The MQW diode provides higher gain than the single quantum well diode, at the cost of a higher threshold current, simply because more electrons and holes are demanded injected into the quantum wells [32, p. 206].

2.5.2 Creating short pulses by gain-switching

Creating short pulses may be done by gain-switching. A LD driver may periodically (with repetition frequency f_{rep}) direct current into the LD for a short duration Δt_{trig}. The diode will then produce laser pulses at repetiton rate f_{rep} with duration of Δt. The average output power of the pulse is then described by Equation 2.28.

2.5.3 Finer selection of wavelength

To allow for more specific wavelength selection different improvements to the Fabry Perot chamber may be taken.

Discrete Mode (DM)

A discrete-mode (DM) LD features a grated structure on the top of the waveguide, causing a correspondingly periodic change in refractive index, which provides additional reflection of one Fabry Perot mode. Thus, this mode is additionally amplified, the others are suppressed, which effectively narrows the output spectrum, the linewidth $\Delta\lambda$, of the diode.

The grating also allows for wavelength tunability of the diode. Varying the temperature, the refractive indices in the grating will change, and correspondingly change the lasing wavelength λ_s [26].

Fiber Bragg Grating (FBG)- stabilization

Fiber Bragg Grating (FBG) stabilization is a method for enhancing one of the Fabry Perot modes, thus obtaining single-mode operation of the LD. Adding a periodic grating of the refractive index in the fiber into which the diode outputs, provides a certain reflection of a single wavelength, which is fed back into the diode, stimulating an extra amplification of this wavelength, and thereby stabilizing the output signal of the diode around this wavelength [52].

2.6 Remote sensing

Remote sensing is gathering information from a distance [53, p. 1]. Laser sources such as mode-locked lasers and LDs combined with fiber amplifiers facilitate remote sensing.

This section shows how laser parameters introduced in the previous sections enable LiDAR, while focusing on pulsed range finding. First, it introduces the LiDAR equation which models the return power to the LiDAR system. LiDAR parameters such as maximal range and resolution are provided. Finally atmospheric effects on pulse propagation is discussed.

2.6.1 Range finding with the pulsed time of flight (TOF) technique

Range finding can be achieved with the pulsed time of flight (TOF) method [6]. As illustrated in Figure 2.13a, the distance or range R between a LiDAR system, consisting of a transmitter and a receiver, and a target is found by measuring the return time t_{ret} of a reflected (or backscattered) pulsed signal. The distance R to the target will then be half the distance the pulse has travelled during t_{ret} [54, p. 9]

$$R = \frac{1}{2}\, t_{ret}\, c. \tag{2.38}$$

Due to beam divergence, as illustrated in Figure 2.13b, the pulse spreads out in a cone and a single pulse may hit and reflect back from several points on one object, at different ranges R. Then, the return pulse will be seen as multiple returning pulses, or alternatively as one return pulse spread out in time. Such applications are 3D imaging [55] where the shape in depth of one object is determined, or LiDAR scanning of forest profiles [56]. Thus, power received at times t, corresponds to backscattering or reflection from range R [55],

$$R = R(t) = \frac{1}{2}\, t\, c. \tag{2.39}$$

Although, time t is the variable the LiDAR systems keeps track of, the equations given or derived here will be functions of R, as this is the parameter of interest, while keeping in mind that R is really a function of time [54, p. 9].

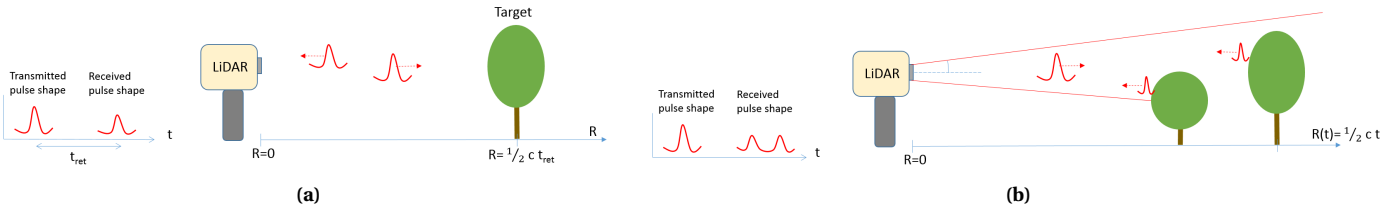

Figure 2.13: (a) Return time t_{ret} determines range. (b) LiDAR beam spreads out in a cone and returns from several targets.

The return pulse is detected at the receiver by a photodetector. A photodetectors may be pin-junction semiconductors similar LDs, where the reverse process to light generation described for LDs in section 2.5 where incident photons are absorbed, and an electron hole pair is generated, inducing an electrical current which is portional to the incident optical power [57]. As detectors have a smallest possible detectable power, the power of the return signal from range R is an important quantity given by the LiDAR equation which will be derived next.

2.6.2 The range finding LiDAR equation - return power

Generally, the the range finding LiDAR equation models the power received at the detector P_r from a target at range R. Specifically when the target is a reflecting surface of reflectance ρ, the power received P_r at time t (corresponding to a range R via Equation 2.39) of a signal at wavelength λ is given by [58]

$$P_r(R,\lambda) = P_t \underbrace{\frac{A_T}{\pi(w(R))^2}}_{\text{Target fill factor}} \rho \underbrace{\frac{A_r}{R^2\Omega_T}}_{\text{receiver fill factor}} \eta_{sys}\, \mathcal{T}(R,\lambda) \tag{2.40}$$

where,

- P_t is the initially transmitted power
- A_T is the cross sectional area of the target illuminated by the beam
- $w(R)$ is the beam radius w at range R, and $\pi\big(w(R)\big)^2$ the area of the beam at range R when the beam is

transmitted from a circular opening.

- A_r is the aperture of the receiver
- ρ is the reflectance of the target
- Ω_T is the solid angle into which the target reflects
- η_{sys} is the efficiency of the transmitter and receiver optics.
- $\mathcal{T}$ is the atmospheric transmittance, and describes the attenuation of the LiDAR signal due to scattering and absorption of the signal. $\mathcal{T}$ will be a number between 0 and 1, depending on the wavelength of the signal λ, and on the range R, and is to be considered in subsection 2.6.4.

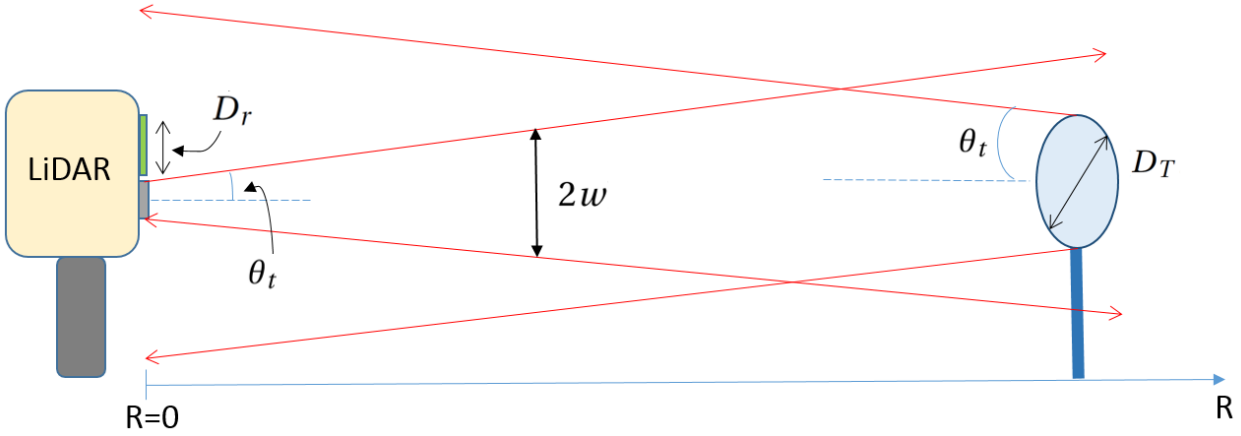

Figure 2.14: A perfectly reflecting circular target of diameter D_T is located at a distance from the LiDAR along the axis of range R. The LiDAR emits pulses in a beam diverging at an angle θ_t, with a range-dependent beam spot diameter of $2w(R)$. The beam reflects off of the target at angle θ_t and is received at the LiDAR, which has a receiver aperture diameter D_r.

Equation 2.40 can be rewritten as will be discussed in the following. Figure 2.14 is included to illustrate important parameters.

The target fill factor of the Equation 2.40, is understood as the fraction of the power emitted by the transmitter that is incident on the target, and equals the ratio of the illuminated area of the target A_T, to the the beam spot area $\pi\big(w(R)\big)^2$ at R. If the beam is Gaussian, it diverges at the transmitter angle θ_t [54, p. 11]. In the far field approximation the spot size radius w at a distance R from the transmitter will be [32, p. 309]

$$w(R) = R\theta_t \,. \tag{2.41}$$

and the beam spot area

$$\pi\big(w(R)\big)^2 = \pi(R\theta_t)^2 \,. \tag{2.42}$$

If the target of diameter D_T is circular, having a cross sectional area $\pi(D_T/2)^2$ as seen from the receiver, then the illuminated area of the target A_T will be

$$A_T = \begin{cases} \pi(D_T/2)^2 & \text{if} \quad 2w(R) > D_T \\ \\ \pi(R\theta_t)^2 & \text{otherwise} \,. \end{cases} \tag{2.43}$$

Thus, the target fill factor is = 1 if the target diameter D_T is larger than the beam spot diameter ($2w(R)$) at R, and < 1 if the beam illuminates more than the target at range R.

The receiver fill factor of the Equation 2.40, is understood as the fraction of beam power reflected at the target that

is incident on the receiver, and equals the ratio of the receiver aperture A_r, to the full area $R^2\Omega_T$ illuminated by the reflector back at the receiver. If the target is a perfect reflector, then light reflects at the same angle θ_t it was incident [17, p. 25], and

$$R^2\Omega_T = \pi(R\theta_t)^2. \tag{2.44}$$

If the receiver has a circular aperture of diameter D_r is the diameter, then

$$A_r = \pi\Big(\frac{D_r}{2}\Big)^2. \tag{2.45}$$

Inserting Equation 2.42, Equation 2.43, Equation 2.44 and Equation 2.45 into the LiDAR Equation 2.40, one obtains a LiDAR equation for perfectly reflecting targets, when the target is either located at a range where it reflects the whole beam ($2w(R) < D_T$), or only a fraction of it ($2w(R) > D_T$),

$$P_r(R,\lambda) = \begin{cases} P_t \ \dfrac{D_T^2/4}{(R\theta_t)^2} \ \rho \ \dfrac{D_r^2/4}{(R\theta_t)^2} \ \eta_{sys} \ \mathscr{T}(R,\lambda) & \text{if} \quad 2w(R) > D_T \\ \\ P_t \ \rho \ \dfrac{D_r^2/4}{(R\theta_t)^2} \ \eta_{sys} \ \mathscr{T}(R,\lambda) & \text{otherwise} \end{cases} \tag{2.46}$$

The effect of the detector rise time t_{rise} on the LiDAR equation

The detector will take a time t_{rise} (rise time or response time) to respond to an incident pulse, by raising the current from 10% to 90% [32, p. 261] of the current corresponding to the optical power of the incident pulse. t_{rise} depends on the detector bandwidth (BW). There are several definitions of rise time [59], however, here [32, p. 261]

$$t_{rise} = \frac{0.35}{\text{BW}}. \tag{2.47}$$

will be used.

P_r of Equation 2.40 and Equation 2.46 is the instantaneous power incident on the receiver. From the point of view of the receiver, with a detector of finite response time t_{rise}, the pulse energy $P_{peak}\Delta t$ (from Equation 2.29), of a pulse of duration Δt and peak power P_{peak}, is spread across an effective pulse width $(t_{rise}+\Delta t)$ [60], and it sees the transmitted power P_t as

$$P_t = P_{peak}\frac{\Delta t}{\Delta t + t_{rise}}, \tag{2.48}$$

under the condition that $\frac{1}{2}c(\Delta t + t_{rise}) << R$ [17, p. 241].

The modification of the LiDAR Equation 2.46 with Equation 2.48 can be understood better by looking at the limiting cases of Δt to t_{rise}. If the response time is much shorter than the pulse width $t_{rise} << \Delta t$, then $P_t \to P_{peak}$ and the detecting of the pulse can be seen as a real time process. If the pulse width is much shorter than the sampling speed $\Delta t << t_{rise}$, then $P_t \to P_{peak}\frac{\Delta t}{t_{rise}}$, and the energy of the pulse received $P_r\Delta t$ is averaged over the rise time t_{rise}.

2.6.3 Range finding LiDAR parameters

A LiDAR may be described by its system parameters range resolution ΔR and maximal range R_{max}. How they depend on parameters of the transmitter and receiver will be discussed here.

Resolution of range ΔR and transverse resolution $\Delta R^{\perp}$

From the detector point of view, the atmosphere can be thought of as divided into discrete boxes. From every box, the LiDAR can then remotely sense information such as gas concentration or the presence of a solid target [5]. The resolution of the LiDAR measurements is then the size of the boxes.In the radial direction (along the beam drawn in Figure 2.14) ΔR is the range resolution. Perpendicular to the beam, $\Delta R^{\perp}$ is the transverse resolution.

If the detector responded instantaneously ($t_{rise} \to 0$) to an incident pulse, the smallest measurable change in range R, the range resolution ΔR, is the product of speed of light c and half the pulse width Δt, or half the distance travelled during the pulse width Δt. However, the finite response time or rise time t_{rise} of the detector also sets limitations on the resolution [17, p. 241]

$$\Delta R = \frac{1}{2} c(\Delta t + t_{rise}). \tag{2.49}$$

The beam spreads out in a cone, covering an area $\pi\big(w(R)\big)^2$, where w was the beam radius given in Equation 2.41. Since ranging often is done from airplanes towards the ground, the cone area is called the beam footprint [53, p. 180]. The transverse range resolution $\Delta R^{\perp}$, the diameter of the spot [53, p. 179],

$$\Delta R^{\perp}(R) = 2w(R) = 2R\theta_t \,, \tag{2.50}$$

may be understood as the closest distance two targets can be located and still be distinguishable.

Whereas the range resolution ΔR is seen to remain constant with range R, the transverse resolution deteriorates with R. According to Equation 2.5. Thus fundamentally, resolution in travel direction is Δt dependent and in the transverse direction, λ dependent.

Maximal range R_{max} of the LiDAR system limited by noise power level P_{noise} and repetition rate f_{rep}

A criterion of the TOF method, is that the return pulse is powerful enough for the sensor in the receiver to distinguish it from the noise power level. The signal-to-noise ratio (SNR), defined as

$$\text{SNR} = \frac{P_r}{P_{noise}}, \tag{2.51}$$

is a figure comparing the LiDAR return power P_r to the total power of all sources of noise P_{noise},

$$P_{noise} = P_{noise}^{BG} + P_{noise}^{det}, \tag{2.52}$$

where P_{noise}^{BG} is external background noise, and P_{noise}^{det} is internal noise in the detector [17, p. 223].

P_{noise}^{BG} includes black body radiation from sources such as the sun and the earth. Direct solar radiation peaks in the visible and is plotted in Figure 2.15a. Also the earth radiates mid-IR wavelengths ($8-14$ μm centred around 10 μm [17, pp. 2-3]. The daytime diffusive components of solar and earth radiation under clear sky conditions at sea level are plotted in Figure 2.15b. Other sources of black body background radiation is thermal radiation from target itself [61] and from the moon and stars at nighttime [5, p. 11].

P_{noise}^{BG} can be estimated for a LiDAR system with receiver aperture area A_r, receiver optics field of view (FOV) solid angle $\Omega_{\text{FOV,r}}$ and detector response wavelength interval $\Delta_{\lambda,r}$, via [13, p. 47]

$$P_{noise}^{BG} = f(\lambda)\ A_r\ \Omega_{\text{FOV,r}}\ \Delta_{\lambda,r}\ , \tag{2.53}$$

where $f(\lambda)$, evaluated at the center wavelength of $\Delta_{\lambda,r}$, is the background radiance in units $\text{Wcm}^{-2}\text{sr}^{-1}\mu\text{m}^{-1}$ (watts per square centimeter of detector aperture, per receiver optics FOV solid angle $\Omega_{\text{FOV,r}}$, per μm of $\Delta_{\lambda,r}$ interval). Figure 2.15b can be used to estimate $f(\lambda)$.

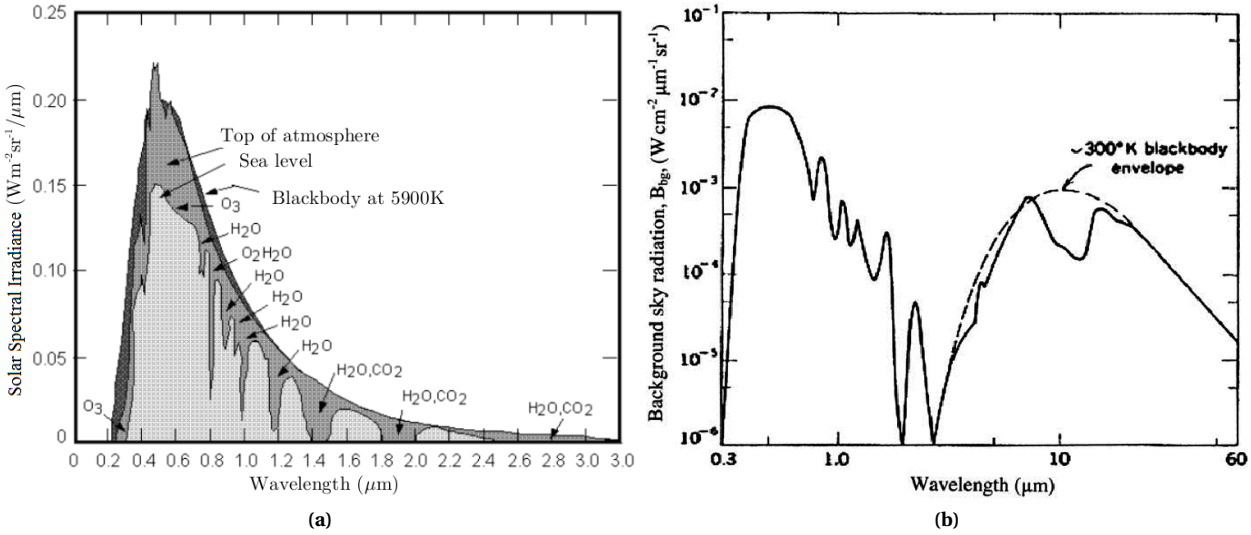

(a) (b)

Figure 2.15: (a) Spectral direct solar irradiance. Appended from [62]. (b) Spectral diffusive solar and earth background radiance at sea level. Appended from [63].

The other component to P_{noise}, is internal noise in the detector P_{noise}^{det} [17, p. 223]. In the absence of radiation shining on the detector, thermally generated charge carriers still produce a current, termed the dark current I_{dark} [17, p. 223], which accounts for a noise level [20, p. 324],

$$P_{noise}^{det} = \frac{I_{dark}}{\mathscr{R}}, \tag{2.54}$$

where $\mathscr{R}$ is the detector responsivity, or its ability to convert optical power to electrical current, and has units AW^{-1}. Both $\mathscr{R}$ and I_{dark} depend on temperature [20, p. 329]. Thermal noise is random, and averaged, does not depend on the range R [64]. P_{noise}^{det} is thus interpreted as the optical signal inducing a current comparable to the dark current.

Alternatively if the spectral noise equivalent power (NEP), and BW of the detector is known, P_{noise}^{det} may be expressed via,

$$P_{noise}^{det} = \mathrm{NEP} \times \sqrt{\mathrm{BW}}. \tag{2.55}$$

NEP of the detector is the optical power which must be incident on a detector of 1 Hz bandwidth to produce a current equal to the current due to all sources of noise in the detector [65]. NEP, in units $\mathrm{WHz}^{-\frac{1}{2}}$ (depends on wavelength and) increases with detector area A_{det} [66, p. 217].

To avoid mistakeingly taking noise to be a return signal, SNR is required to be greater than a creditable [17] SNR_{min}, the smallest detectable optical signal $P_{r,min}$ will consequently be

$$P_{r,min} = \mathrm{SNR}_{min} \times P_{noise}. \tag{2.56}$$

Letting the left side of Equation 2.40 be $P_{r,min}$, the maximal range R_{max} is given implicitly by

$$R_{max} = \begin{cases} \left(\dfrac{P_t}{P_{r,min}} \dfrac{D_T^2/4}{\theta_t^2} \rho \dfrac{D_r^2/4}{\theta_t^2} \eta_{sys} \mathscr{T}(R_{max}, \lambda) \right)^{\frac{1}{4}} & \text{if } 2R_{max}\theta_t > D_T \\ \sqrt{\dfrac{P_t}{P_{r,min}} \rho \dfrac{D_r^2/4}{\theta_t^2} \eta_{sys} \mathscr{T}(R_{max}, \lambda)} & \text{otherwise} \end{cases} \tag{2.57}$$

and can be solved for numerically, or by making assumptions on $\mathscr{T}(R_{max}, \lambda)$. Allowing smaller return signals, by

relaxing the restrictions on SNR_{min}, the LiDAR device can see further, however the chance of falsely detecting a return signal increases.

R_{max} of a LiDAR based on the TOF method is also limited by the repetition rate f_{rep} at which pulses are transmitted [18]. To distinguish two successive pulses, and hence the information they carry, the return time t_{ret} of the pulse must be shorter than the time period $T_{rep} = \frac{1}{f_{rep}}$ between two successive pulses [18]. Thus,

$$R_{max} < \frac{1}{2}\frac{1}{f_{rep}}c, \tag{2.58}$$

where the right side is half the distance the pulse can travel during T_{rep}. There is a trade off between having high rates of acquisition f_{rep}, and sensing at further distances R_{max}.

Thus, the longest measurable distance R_{max} can be increased by optimizing the parameters of Equation 2.57, but must be kept below the threshold of Equation 2.58 to avoid ambiguities in range.

2.6.4 Atmospheric transmittance $\mathscr{T}$

Rigorous calculations of atmospheric transmittance $\mathscr{T}$ is beyond the scope of this thesis. The intention of this section however, is explaining how $\mathscr{T}$ depends on the signal wavelength λ, so that an educated choice of wavelength can be made for every LiDAR application.

Deriving an expression for $\mathscr{T}$

The laser signal transmitted by the LiDAR system is attenuated due to photons in the beam being absorbed by molecules, and Rayleigh or Mie scattered out of the beam by molecules, particles, aeorosols, fog, haze, rain and snow in the atmosphere. Thus, the information about the atmosphere, carried by the LiDAR Equation 2.40, is contained in the transmittance coefficient $\mathscr{T}$ [5, p. 6].

The attenuation of signal power $\mathrm{d}P$ propagated a distance $\mathrm{d}x$ through the atmosphere, can be modelled analogously to how photons are absorbed by dopant ions in the fiber, by rewriting Equation 2.20 [13, p. 28],

$$\frac{\mathrm{d}P}{P} \propto -\Big(\sum_s N_s(x)\sigma_s(\lambda) + \sum_a N_a(x)\sigma_a(\lambda) \Big)\mathrm{d}x\,, \tag{2.59}$$

where it is summed over contributions from all species of absorbers a and scatterers s. The densities of the atmospheric scatterers N_s and absorbers N_a will be unevenly distributed along the path of propagation, and thus depend on the location x. The cross sections $\sigma_a(\lambda)$ (absorption) and $\sigma_s(\lambda)$ (scattering) carry the spectral information on the strength of attenuation by scatterers or absorbers. To be precise, molecules may act as both absorbers and scatterers [5, p. 11].

Integrating both sides of Equation 2.59 along the path $x = 0$ (transmitter) to the target at range $x = R$, and back to the transmitter, one obtains the transmittance coefficient $\mathscr{T}$ [5],

$$\mathscr{T}(R,\lambda) = \underbrace{\exp\Big(-2\int_0^R \sum_s N_s(x)\sigma_s(\lambda)\mathrm{d}x\Big)}_{\text{Scattering}} \times \underbrace{\exp -2\int_0^R \sum_a N_a(x)\sigma_a(\lambda)\mathrm{d}x}_{\text{Molecular Absorption}} \tag{2.60}$$

$\mathscr{T}(R,\lambda)$ is a decreasing function in R, and will always approach 0 as $R \to \infty$, because σ_a and σ_s never truly are 0, as there always are molecules present in the atmosphere. Full transmittance $\mathscr{T} = 1$ is only achieved in vacuum. Here follows a closer look at the strength of absorption and scattering processes given contained in the cross section.

Atmospheric molecular absorption

The absorbers may be atmospheric gases CO_2, O_2 or NO_2. Each gaseous molecule has its own fingerprint energy spectrum, where the main electronic energy levels split into manifolds due to vibrational energy states of the molecule, and further split into a finer spectrum due to rotational energy states [67, pp. 64-65].

The absorption per meter $\sigma_a(\lambda)N_a(x)$ spectrum corresponds to all possible energy level transitions a molecule a may undertake by absorbing a photon of wavelength λ [8, p. 216]. Figure 1.2b showed the absorption lines of various gases a within the IR $2-2.5$ μm atmospheric window. Transitions between electronic energy levels require absorption of UV and visible photons, whereas IR photons excite vibrational and rotational transitions [8, p. 216]. Whereas the gas concentration $N_a(x)$ strengthens the absorption line, the absorption cross section $\sigma_a(\lambda)$ contains all information on where (at what wavelengths) in the spectrum absorption lines are found. Photons absorbed by the gas molecules are either reemitted at a later time, or dissipation as heat within the gases due to ion-ion transitions, and can be taken as removed from the beam.

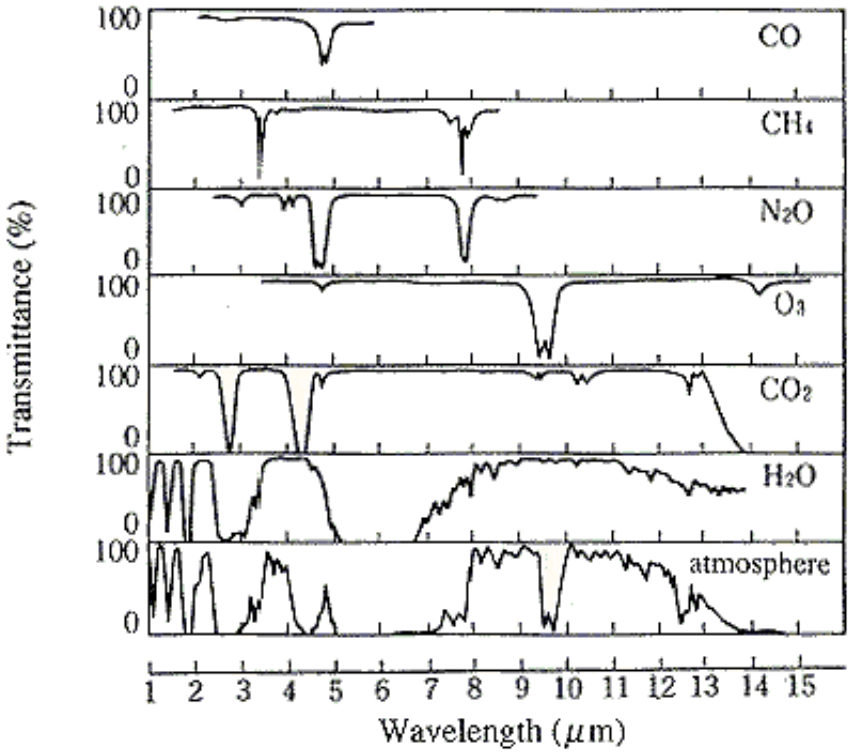

Figure 2.16: The contribution from various gases to spectral atmospheric transmittance due to absorption and neglecting scattering. The lower graph is the combined contribution to transmittance from all gases. Appended from [68].

The lowest graph of Figure 2.16 shows transmittance $\mathscr{T}$ only limited by absorption, while neglecting scattering, of signals at λ between $1-15$ μm across R, where R is an entire vertical column of the atmosphere. In contrast, the upper graphs show the contribution to $\mathscr{T}$ from individual gases. How the lowest graph relates to the other graphs is nicely shown mathematically, by factorizing the transmittance due to absorption in Equation 2.60. Assuming independent molecules, the exponential of a sum of exponents can be rewritten into a of product of exponentials,

$$\underbrace{\exp\left(-2\int_0^R \sum_a N_a(x)\sigma_a(\lambda)\mathrm{d}x\right)}_{\text{transmittance due to absorption of all gases}} = \prod_a \underbrace{\exp\left(-2\int_0^R N_a(x)\sigma_a(\lambda)\mathrm{d}x\right)}_{\text{transmittance due to absorption of gas } a} . \tag{2.61}$$

The left side of Equation 2.61 corresponds to the lower graph of Figure 2.16, while each factor of the right side of

Equation 2.61 corresponds to the transmittance spectrum due to each individual gas in Figure 2.16.

Figure 1.2a showed the transmittance due to absorption by all gases in the $2-2.5$ μm atmospheric window in more detail.

The transmittance spectrum due to absorption in Figure 2.16 is further modified by scattering, as will be seen next.

Atmospheric Rayleigh and Mie scattering

A simple picture of scattering is the interaction of photons with the scatterer (a molecule, aeorsol, small particles or water droplets), causing the photon to change direction [54, p. 15]. Scattering of photons out of the beam is modelled as extinction in Equation 2.60, because the photons are no longer part of the signal [54, p. 15]. The scattering cross section σ_s symbolizes the area of the beam removed due to scattering, and varies with the scatterer radius q to photon wavelength λ ratio $\frac{q}{\lambda}$ [8, p. 213]. In Figure 2.17, σ_s normalized by the geometric cross section $\sigma_g = \pi q^2$ of the scatterer is plotted against $\frac{q}{\lambda}$.

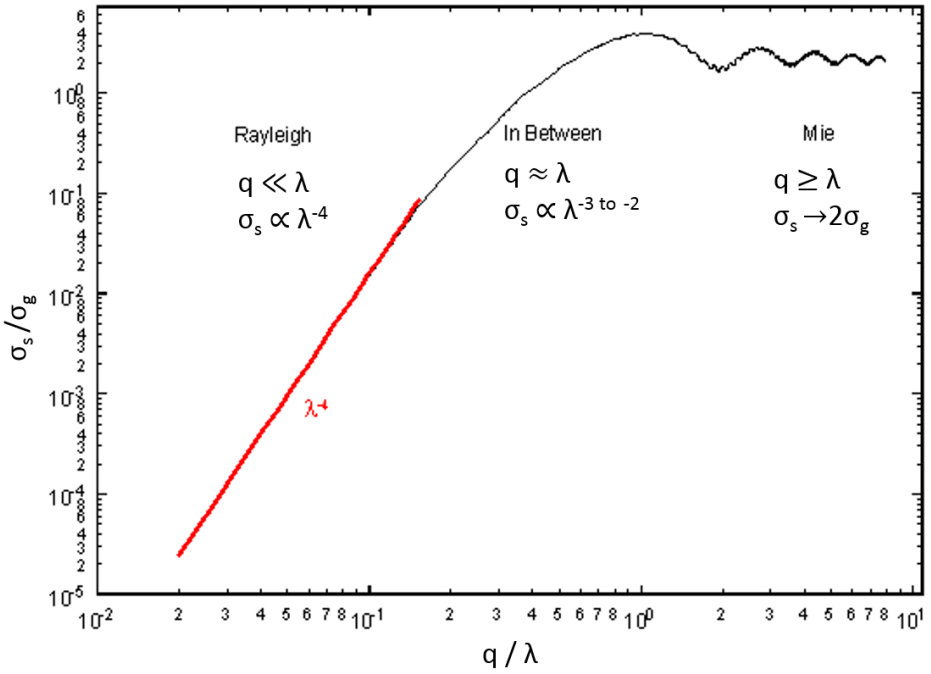

Figure 2.17: Scattering cross section σ_s normalized by the geometric cross section σ_g, plotted against the ratio of scatterer radius q to wavelength λ. Rayleigh ($q << \lambda$) and Mie ($q \geq \lambda$) scattering regimes are indicated. Appended by [69].

Rayleigh scattering describes the regime where the size of the scatterer (molecule or atoms) is much smaller than the signal wavelength ($q << \lambda$) [67, p. 186]. The incident photon raises the molecule to a virtual energy level [17, p. 206] from which it immediately [54, p. 195] relaxes and emits a photon of the same wavelength. The scattering cross section in the Rayleigh regime is proportional to [70]

$$\sigma_s(q << \lambda) \propto \frac{q^6}{\lambda^4} \propto \frac{q^4}{\lambda^4}\,\sigma_g\,. \tag{2.62}$$

Mie scattering describes the regime where the size of the scatterer is comparable to or larger than wavelength ($q \geq \lambda$) [67, p. 53]. Mie scattering involves more complex solution of Maxwell equations around a sphere involving Bessel functions and spherical harmonics [8, p. 291]. Here, it is sufficient to say that the Mie scattering cross section

will be on the order of the geometric cross section, as seen in Figure 2.17 and,

$$\sigma_s(q \geq \lambda) \propto \sigma_g \,. \tag{2.63}$$

It is clear from Figure 2.17 that when fixing concentration N_s and radius q by specifying the scatterer species, the scattering cross section seen by the incoming signal increases when the signal wavelength decreases. Thus, signals of wavelength $\lambda >> q$ will Rayleigh scatter and attenuate much less than a signals of wavelength $\lambda < q$ which will Mie scatter.

The lower graph of Figure 2.16 showed atmospheric transmittance $\mathscr{T}$ only due to absorption. Absorption governs at which wavelengths windows in the atmospheric transmittance spectrum windows can be found. Scattering modulates the numerical value of $\mathscr{T}$. Since the constituents of the atmosphere are fixed for all wavelengths, the atmospheric windows become more and more transparent with increasing wavelength.Figure 1.1 showed the combined effect of absorption and scattering on $\mathscr{T}$, where the part of the transmittance due to absorption was modulated by the scattering (red line) to produce the full transmittance $\mathscr{T}$ (bold line) as given in Equation 2.60.

Choosing LiDAR wavelength based on $\mathscr{T}$

Transmittance $\mathscr{T}$ depends the direction and length of range R, and is then technically only valid for that specific path. Still, the transmittance of the entire atmosphere is included as an important example. When Figure 1.1 shows that signals at certain λ can in fact transverse the entire height of the atmosphere with $\mathscr{T} > 0.7$. Such λ could also be expected to be transparent at other ranges R in other directions although the exact numerical value of $\mathscr{T}$ would of course generally be different.

Thus, to make an educated choice of LiDAR wavelength, figures such as Figure 1.2a showing transmittance due to absorption in the IR window at 2-2.5 μm, or Figure 1.1 can be consulted to make an educated choice of LiDAR signal wavelength. This approach to choosing LiDAR wavelength was adopted by [13, pp. 55-56].

As a final remark, and to allude to appendix B, it can be said that to truly predict the atmospheric transmittance $\mathscr{T}$ the concentrations of all N_a and N_s would have had to be known. these concentrations change in time with winds, an in space with for example local pollution. Determining N_a and N_s is a main task of LiDAR systems called Differential Absorption LiDARs (DIALs) [54, pp. 124-127].

Chapter 3

Experimental setup

This chapter gives a brief overview of the MOPA system setups, as well as the range-finding LiDAR system setup.

3.1 Master Oscillator Power Amplifier (MOPA) Setup

The MOPA systems shown in Figure 3.1 consist of a master oscillator (a laser generating an optical signal) and a power amplifier shown in Figure 3.2. Two possible MOPA configurations were considered with either the laser diode (LD) or mode-locked holmium-doped fiber laser as master oscillator. For convenience, these are respectively referred to as the LD-MOPA shown in Figure 3.1a and the mode-locked-MOPA shown in Figure 3.1b.

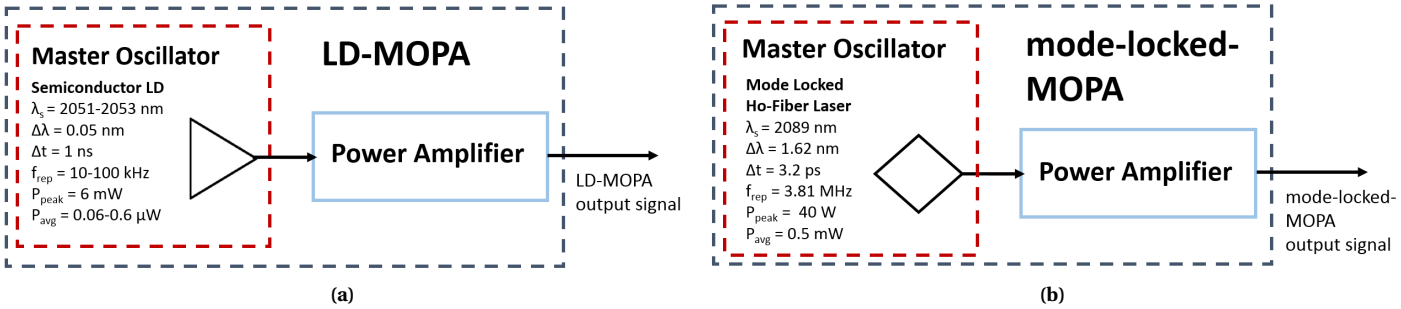

Figure 3.1: The setup of two MOPA configurations, with either a (a) laser diode (LD) or (b) mode-locked holmium-doped fiber laser as master oscillator. The power amplifier is shown in Figure 3.2.

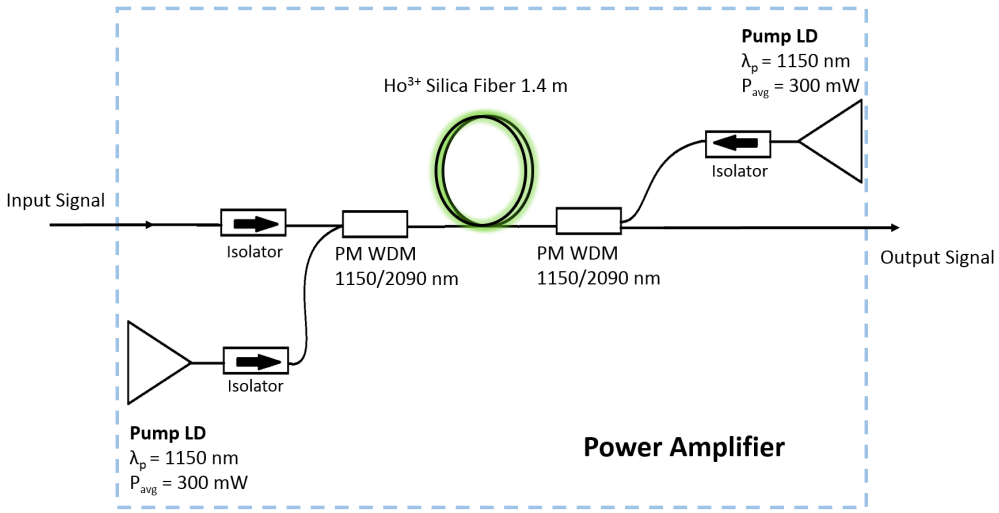

Figure 3.2: The power amplifier from either MOPA configuration shown in Figure 3.1. Triangles represent semiconductor pump LDs, rectangles with arrows are isolators, and plain rectangles represent polarization maintaining (PM) wavelength division multiplexers (WDMs). Optical fibers are drawn as bold lines. The holmium-doped active fiber is coloured green to distinguish it from the passive fiber.

3.1.1 Master Oscillators

The output characteristics of the signal produced by each master oscillator are summarized below and in Figure 3.1a and Figure 3.1b respectively.

Master Oscillator: Laser Diode

The gain-switched DM MQW semiconductor LD (Eblana Photonics) emits at wavelength λ_s tunable between 2051 – 2053 nm, with spectral line width $\Delta\lambda < 0.05$ nm. In pulsed mode, the diode is driven to emit pulses with nanosecond pulse duration Δt and peak power P_{peak} of 6 mW at a repetition rate f_{rep} tunable between 10 – 100 kHz, corresponding to average power P_{avg} of 0.06 – 0.6 μW

Master Oscillator: Mode-locked The Holmium-doped Fiber Laser

A mode-locked holmium-doped fiber-laser emits at λ_s = 2088.90 nm with a line width of $\Delta\lambda$ = 1.62 nm. The laser emits pulses at about 3 ps pulse duration Δt, at repetition rate f_{rep} of 3.81 MHz, and average power P_{avg} = 0.5 mW, corresponding to a peak power P_{peak} of 40 W.

3.1.2 Power Amplifier

The power amplifier in Figure 3.2 is a device on its own, which takes an input signal, amplifies it and transmits further. The amplifier output is also the MOPA output.

Pump Diodes

The two identical pump diodes are FBG-stabilized single-mode fiber-coupled MQW CW semiconductor LDs (Innolume). The diodes emit at pump wavelength λ_p = 1150 nm with maximal output of P_{avg} of 300 mW.

Active Fiber

The active fiber is a commercially available single-mode PM Ho^{3+}-doped silica fiber (iXblue IXF-HDF-PM-8-125). The fiber has a 8 μm core diameter d_{core} and 126.5 μm cladding diameter d_{clad}. The Ho^{3+} doping concentration N_{Ho} is 6 x10^{25} m^{-3}. The fiber length L is 1.4 m.

Wavelength Division Multiplexers (WDMs) and Isolators

The input and output of the power amplifier as well as the output of the respective pump LDs were coupled to the active fiber via PM-fiber-based 1150/2090 Wavelength Division Multiplexers (WDM). These WDMs are specially designed to couple and divide signals at wavelengths of 1150 nm and 2090 nm.

Isolators (Innolume) placed according to Figure 3.2, are unidirectional and made to withstand 500 mW average power. They prevent unwanted feedback to the components.

3.2 LiDAR setup

The LiDAR setup is shown in Figure 3.3. It consists of a transmitter and a receiver. The transmitter outputs a pulse (the LiDAR output), while the returning pulse (the LiDAR input) is received by the receiver.

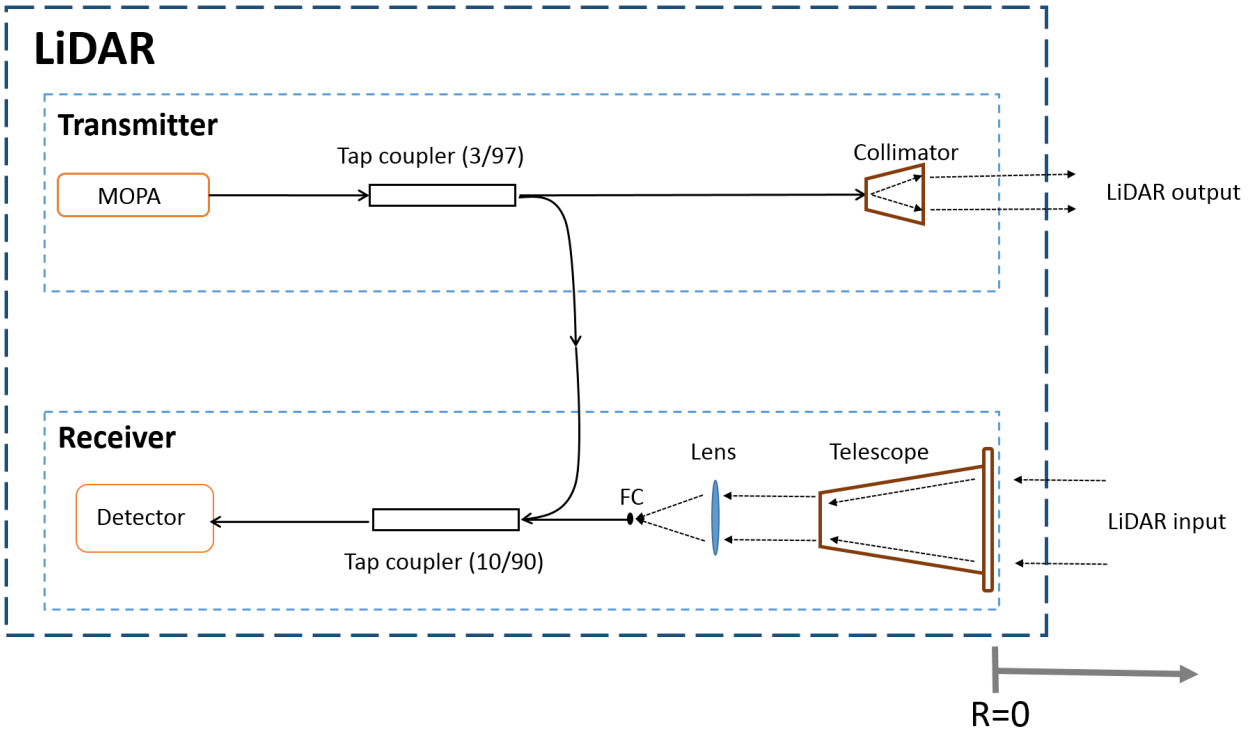

Figure 3.3: Range-finding LiDAR setup. The transmitter consist of a laser source (either MOPA from Figure 3.1), a (3/97) tap coupler, and a collimator transmitting the LiDAR output signal. The LiDAR receiver consists of a telescope receiving the LiDAR input signal, a lens, a fiber holder (FH) and a (10/90) tap coupler. Passive fibers are drawn in bold lines, whereas the free space beams are drawn with dotted lines. Signal propagation direction is indicated with arrows. Range R between the LiDAR and a target is measured from the telescope input.

3.2.1 Transmitter

The pulsed transmitter laser source MOPA can be either the LD-MOPA in Figure 3.1a or the mode-locked-MOPA in Figure 3.1b.

The MOPA output power is split by a (3/97) tap coupler (Gooch & Housego). Tap couplers are bidirectional with, and have four ports, two at each side. The power of a signal entering a port, will be split between the two ports on the other end by a coupling ratio specified for the particular port of entrance.

97% of the signal power is guided through a collimator (Thorlabs TC06FC-2000) of divergence angle $\theta_t = 1.04$ mrad. The pulsed free space output of the collimator is also the LiDAR output.

3% of the MOPA output signal power is guided directly towards the receiver to serve as a reference pulse for subsequent delay time measurements.

3.2.2 Receiver

The pulsed LiDAR input signal is received by a telescope (Thorlabs BE15M) of aperture diameter D_r = 48 mm.

The telescope output is focused by a Thorlabs lens of 25 mm focal length into the passive fiber via a fiber holder (FH), it is then guided through the 90 % port of a (10/90) tap coupler (Gooch & Housego), where it meets the signal coming directly from the transmitter at the 10% port of a (10/90) tap coupler.

Both pulsed signals are guided to the fiber-coupled detector (Newport 818-BB-51). The detector has a rise time t_{rise} = 28 ps, spectral response between 830 nm - 2150 nm, dark current I_{dark} = 1 μA and responsivity $\mathscr{R}$ = 0.7 AW^{-1}.

The delay time between the pulsed signals relate to a range R. The zero-range line $R = 0$ is defined at the telescope entrance.

Chapter 4

Characterization of the MOPA laser components

The MOPAs in Figure 3.1 incorporate a total of four different laser oscillators. They are the two possible master oscillators, as well as the pump LDs of the power amplifier. Experimentally characterizing the optical properties (optical spectrum, temporal behaviour and output power) of all laser sources, was important for several reasons. First, the optical output of the master oscillators point out which LiDAR applications they are suited for. Especially, the dependence of tunable parameters on control parameters is of interest. Secondly, to build and optimize a power amplifier, the characteristics of the master oscillators to be amplified, as well as the pump LDs are necessary.

In this chapter, every individual laser component of the MOPA setup will be considered separately. First, details about the setup and operation are given. Then the results from optical characteristics are presented.

4.1 Master Oscillator Laser Diode

The first master oscillator is an electrically controlled, gain-switched DM, MQW, semiconductor LD (Eblana Photonics) emitting around 2.05 μm.

4.1.1 Setup and operation

Being an InGaAs/InP layered MQW semiconductor LD, the LD outputs an optical signal as described in subsection 2.5.1 when given a current I_{on}.

Gain-switched, the LD can be driven in pulsed mode by a pulsed laser diode driver (Highland Technology T160). The driver generates a constant on current I_{on}. Logic within the driver directs the I_{on} to the LD when the driver is triggered periodically by an external triggering voltage source (Hewlett Packard 8116A Pulse/Function). The voltage source generates electrical voltage trigger pulses, at repetition rate f_{rep}, with amplitude V_{trig} and duration Δt_{trig}, which may all be set at the voltage source, and are related to the optical output of the LD.

The LD can also be driven in CW mode, by letting a current source (Thorlabs LDC200C) continuosly direct a current I_{on} to the LD.

The LD features a built in semiconductor optical amplifier (SOA) which provides additional amplification of the LD output power, and is driven by a CW driver (Wavelength Electronics LDTC2/2).

To monitor the LD temperature T, the LD has a built in 10 kΩ thermistor with a temperature dependent resistance $R_{therm}(T)$. The thermistor is driven by the CW driver. The CW driver directs a constant current $I_{therm} = 100$ μA through the thermistor. Measuring the voltage drop V_{therm} $R_{therm}(T)$ is calculated according to

$$R_{therm}(T) = \frac{V_{therm}}{I_{therm}}. \tag{4.1}$$

The dependence of $R_{therm}(T)$ on T is modelled by the Steinhart-Hart equation and can be found in tables [71].

To regulate the LD temperature, the LD has an integrated thermoelectric cooler (TEC), which is driven by the CW driver. The LD temperature is regulated by varying the current directed to the TEC by the CW driver. The TEC

current is controlled mechanically by turning a screw on the CW driver. The LD is mounted on a heat sink with a fan transporting excess heat away. Being DM, the LD output laser wavelength λ_s changes with LD temperature T as described in section 2.5.3.

4.1.2 Optical output characteristics

The master oscillator LD has the following optical output characteristics.

Pulse Duration Δt and repetition rate f_{rep}

Figure 4.1 shows the optical pulses emitted by the semiconductor LD with pulse widths Δt from left to right of 1.2 ns, 6.2 ns and 15 ns. The pulses were obtained by triggering the driver with electrical pulses from the triggering voltage source according to parameters given in Table 4.1. Shorter electrical pulse widths Δt_{trig} produce shorter optical pulse widths Δt. Δt_{trig} of 8 ns producing an optical pulse with Δt of 1.2 ns was the shortest producible by the triggering voltage source. The electrical pulses are generated as square pulses. Longer Δt_{trig} reproduces square optical pulse shapes. Short Δt_{trig} produce peaked optical pulses.

It was observed that the repetition rate f_{rep} at which the LD emits pulses coincided with which the triggering source triggered the pulsed driver between 10 and 100 kHz.

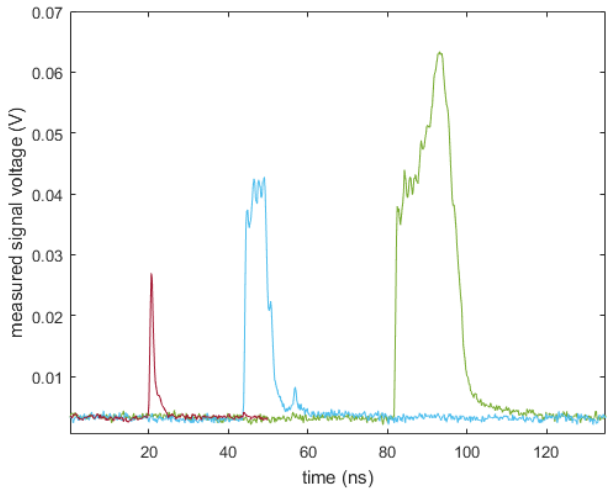

Figure 4.1: Optical pulses emitted by the LD with Δt of 1.2, 6.2 and 15 ns obtained by varying the triggering conditions tabulated in Table 4.1.

Δt_{trig} ns	V_{trig} V	f_{rep} kHz	Δt ns
8	1.42	100	1.2
12	1.52	100	6.2
19	1.52	100	15

Table 4.1: Electrical trigger pulse duration Δt_{trig} and voltage amplitude V_{trig} at repetition frequency f_{rep} producing LD optical output pulses of duration Δt also at repetition frequency f_{rep} plotted in Figure 4.1.

Temperature dependent optical spectrum

While run in CW mode, the spectral output of the LD could be analyzed at an optical spectrum analyzer.

Figure 4.2a shows the measured optical spectrum of the LD with a well defined laser wavelength λ_s at 2051.81 nm and a laser linewidth $\Delta\lambda$ of 0.05 nm when the LD temperature was 24 °C.

Varying the current directed to the TEC, the measured thermistor resistance R_{therm} plotted against the center wavelength λ_s of the LD spectrum is plotted in Figure 4.2b. The lowest measured resistance of 7 kΩ corresponds to a LD

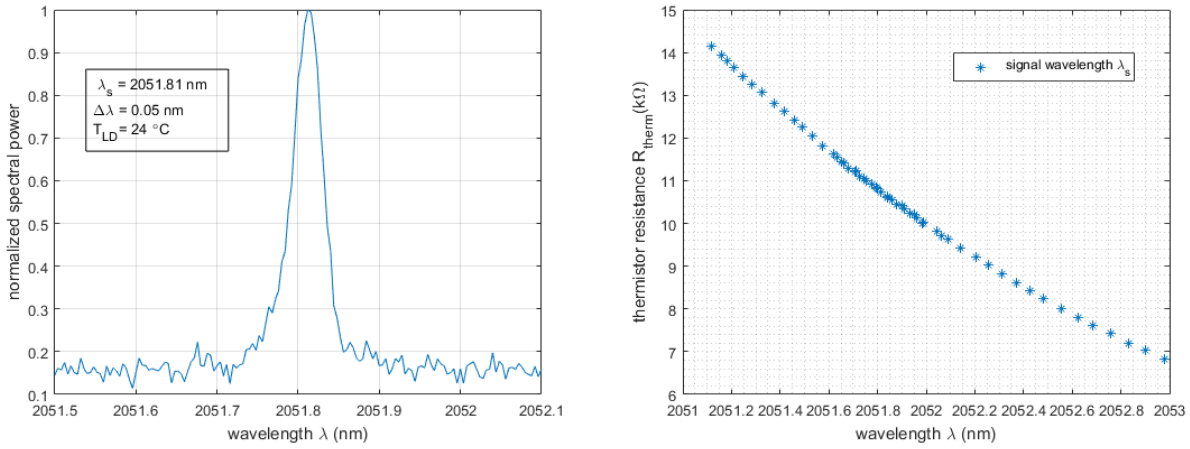

(a) **(b)**

Figure 4.2: (a) Optical spectrum of the master oscillator LD at λ_s = 2051.81 nm, linewidth $\Delta\lambda$ = 0.05 nm at LD temperature T_{LD} = 24°C. (b) Varying T_{LD} (monitored by the thermistor resistance R_{therm}) by setting the TEC current, the signal wavelength λ_s may be chosen with a precision $\delta\lambda$ limited by the resolution of the optical spectrum analyzer.

temperature of 30°C and the highest measured resistance 14 kΩ corresponds to a 17°C LD temperature, which is within the operating temperature of the LD suggested by the LD manufacturer [72].

On average, the linewidth $\Delta\lambda$ of the output was 0.056 nm. According to Heisenberg uncertainty principle of Equation 2.4, and assuming a Gaussian temporal profile of the pulse, the constant of Equation 2.4 0.441 [33, p. 10], pulses centered at λ = 2052 nm will not be transform limited by the linewidth $\Delta\lambda$ of 0.05 nm until the pulse duration Δt is shorter than 280 ps. Consequently, the linewidth $\Delta\lambda$ of 0.05 nm found while operating the LD in CW regime is assumed not to broaden when the LD is run in a nanosecond pulsed regime.

Power-current curve

With a SOA current of 100 mA, the output power of the LD when varying the I_{on} controlled at the pulsed laser diode driver up to 200 mA, is shown in Figure 4.3. When driven in CW mode, Figure 4.3 shows the average power of the LD emission. Driving the LD in pulsed mode, Figure 4.3 shows the peak power of the emitted pulses. The LD current threshold is 21 mA [72].

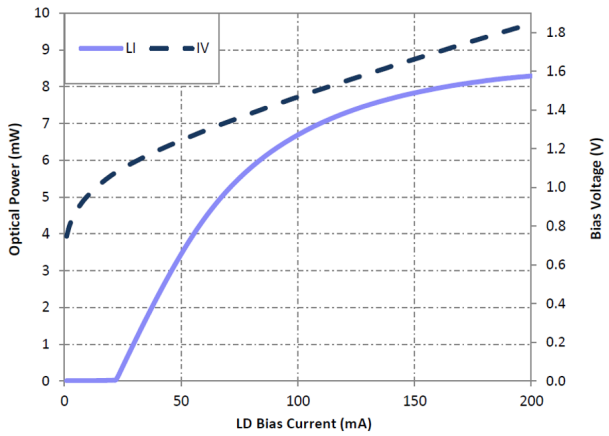

Figure 4.3: LD Power output (peak power in pulsed mode, and average power in CW mode) versus LD input current I_{on} (LD Bias current), with an SOA current of 100 mA. Appended from [72].

4.2 Master Oscillator Mode-Locked Holmium-doped Fiber Laser

The second master oscillator is an available mode-locked holmium-doped fiber laser emitting around 2090 nm.

4.2.1 Setup and operation

The full description of the mode-locked laser setup is beyond the scope of this thesis. An interested reader can find the details in [73]. The laser will therefore be treated as a "black box" with one set of optical output parameters, and started by a CW laser diode driver (Altechna, Tiny LDD Laser Diode Driver).

4.2.2 Optical output characteristics

The mode-locked laser emits at $\lambda_s = 2088.90$ nm with a line width of $\Delta\lambda = 1.62$ nm a seen in Figure 4.4.

The average output power was measured to be just above the minimal measurable power of the used power meter, and was found to be $P_{avg} = 0.5$ mW. Corresponding to a measurement uncertainty of 20 %.

The around 3 ps pulse duration is too short to be measured by any available photodetector. An alternative measurement method is an autocorrolation technique, requiring a certain minimal power, which is higher than the mode-locked laser average power. However, at 12 dB amplification, the pulse duration was found to be $\Delta t = 3.2$ ps. As the spectrum had not changed noticeably (narrowed to 1.41 nm), the pulse duration is assumed to have remained the same. Thus the mode-locked laser is characterized with a 3 ps pulse duration.

The laser emits pulses at a repetition rate of $f_{rep} = 3.81$ MHz.

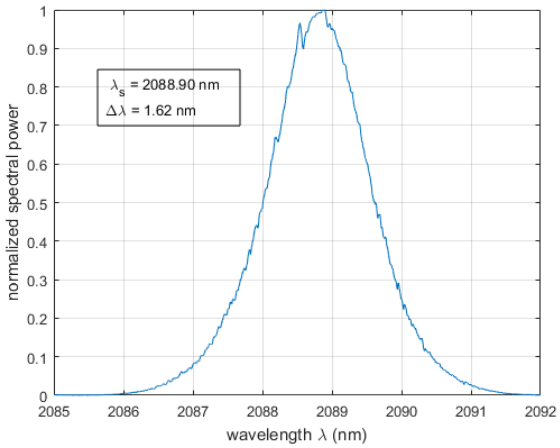

Figure 4.4: Optical spectrum of the mode-locked holmium-doped fiber laser at $\lambda_s = 2088.90$ nm, linewidth $\Delta\lambda = 1.62$ nm.

4.3 Power Amplifier Pump Laser Diodes

The power amplifier pump LDs are CW FBG-stabilized LDs (Innolume) emitting at 1150 nm.

4.3.1 Setup and operation

Directing a continuous current to either pump LD, the pump LD emits continuously as described in subsection 2.5.1.

Each pump LD is driven by a CW laser diode driver (Altechna, Tiny LDD Laser Diode Driver). The LD currents are monitored on a display screen on the drivers.

To prevent heating, the drivers also control the built in TEC of each pump LDs. The pump LDs are each mounted on a fan transporting the excess heat away.

4.3.2 Optical output characteristics

The pump LDs have the following optical output characteristics.

Power-current curves

The minimal possible LD current the driver can provide is 400 mA, which is already above the lasing threshold of the pump LDs. Each LD should not be provided with a current higher than 1200 mA. For this current range, the LDs have linear power current curves shown in Figure 4.5.

Optical Spectra

The optical spectra of the two pump LDs provided by the producer are shown in Figure 4.6a and 4.6b. The diodes both emit at wavelength λ_p of 1150 nm.

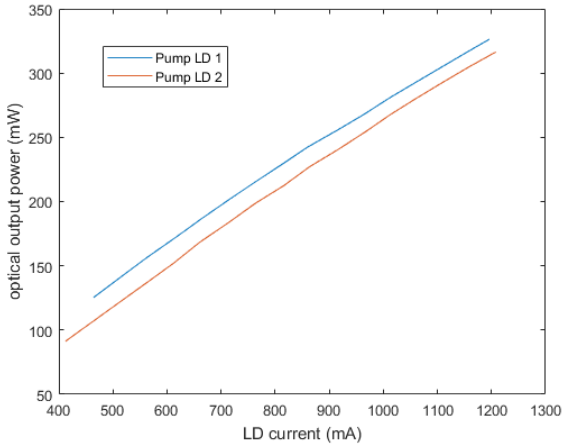

Figure 4.5: Optical output power of the pump LD 1 (blue) and 2 (orange) for input LD currents provided by the LD driver.

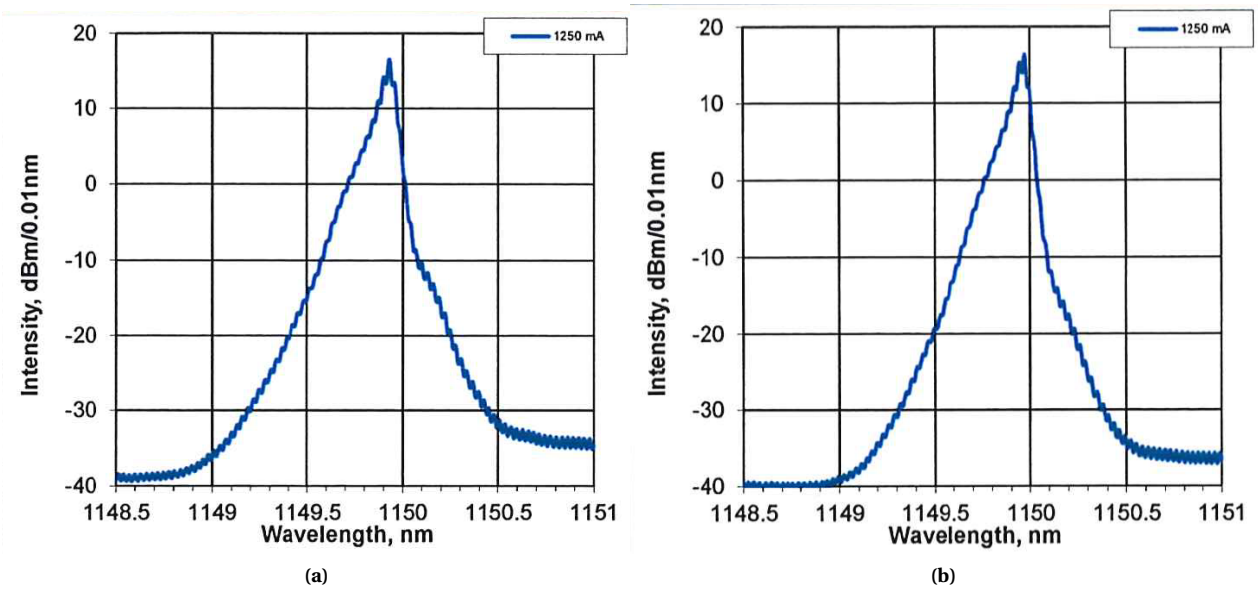

Figure 4.6: (a) Optical spectrum of pump LD 1. Appended from [74].(b) Optical spectrum of pump LD 2. Appended from [75]

Chapter 5

Modelling the Power Amplifier

Simulating the performance of the MOPA systems shown in Figure 3.1 was done in the software *RP Fiber Power V5.0*. This was also the main tool for designing the power amplifier shown in Figure 3.2. The parameters of the power amplifier were chosen in order to maximize the total gain of the signal from the LD master oscillator characterized in section 4.1.

This chapter gives a short introduction to *RP Fiber Power V5.0*, and the assumptions it is based on. It then goes on to describe the process of designing the power amplifier. Lastly the results from the simulations of the power amplifier when integrated in the two MOPAs are presented and discussed.

5.1 A note about *RP Fiber Power V5.0*

A more concise introduction to *RP Fiber Power V5.0* one can get by consulting the manual [76].

The software divides a fiber with length L into steps Δx. Furthermore, the fiber type is specified by doping concentration N, geometrical properties like core and cladding diameters d_{core} and d_{clad}, as well as fiber numerical aperture NA. Spectroscopic properties such as the doping ion absorption and emission cross sections σ_{abs} and σ_{em}, as well as upper to lower laser level radiative lifetime τ.

Initial parameters of the signal to be amplified, hereafter referred to as the signal with parameter subscript s, as well as initial values of the pump energy source of parameters subscripted p, are specified. Parameter include signal and pump average input powers P_s^{in} and P_p^{in}, wavelengths λ_s and λ_p, as well as passive losses discussed in section 2.3.7. Also the end at which the signal or pump source enters the fiber is indicated by a forwards or backwards direction. The V number at the signal and pump wavelengths are calculated using Equation 2.6 is also considered and initial parameter. Finally, also spectral properties of ASE may be defined.

Taking the initial parameters, functionality allows the user to define channels for both CW or pulsed pump and signal sources, as well as channels for ASE. A steady-state or time-dependent model for the pulses must be adopted depending on the pulse energy as discussed in subsection 2.3.5. In the case of a steady-state solution, the coupled rate Equation 2.21 and gain Equation 2.15 are solved iteratively throughout the fiber, until the steady state solution is found. The signal, pump and ASE output powers can than be retrieved, and plotted. The user can calculate and plot gain G (Equation 2.21) and efficiency η (Equation 2.34). The effect on output parameters varying initial conditions such as fiber length L or by adding pump channels (forwards or backwards) different scenarios are modelled and studied. The user is free to define pulse parameters such as peak power P_{peak}, pulse duration Δt and repetition rate f_{rep} and calculate an average power via Equation 2.28 to be used as P_s^{in}, to look at effects of changing pulse properties.

Generally simulations can serve as a help when designing a fiber laser system. Since any model is an approximation and simplification of the physical process, the results of the simulations should be considered with a certain degree of skepticism. Also every model has a domain of input signal characteristics across which it is valid, a relevant example being a steady state model of amplification of pulses. Models aim at replicating the real-life behaviour of the fiber laser systems, and should always be verifying and improved using experimental data.

5.2 Designing the Power Amplifier

The finalized design of the the power amplifier was presented in Figure 3.2. It was chosen after carefully considering several alternative setups. This process is described here.

5.2.1 Possible amplifier components and parameters to be optimized

The power amplifier integrated in the LD-MOPA setup is shown in Figure 3.1a. Table 5.1 summarizes the LD parameters from section 4.1, when run in pulsed and CW mode which were considered when designing the power amplifier.

	λ_s nm	$\Delta\lambda$ nm	$P^{in}_{s,avg}$	$P^{in}_{s,peak}$ mW	Δt ns	f_{rep} kHz
LD in pulsed mode	2051	0.05	0.6 μW	6	1	100
LD in CW mode	2051	0.05	6 mW	-	-	-

Table 5.1: Signal parameters for which the fiber type and number of pump diodes were chosen.

Whether to apply a time-dependent or steady-state model of pulse amplification in the amplifier, the requirements of subsection 2.3.5 were considered. First, looking at Figure 2.9, the effective cross section does not vary significantly across the 0.05 nm linewidth $\Delta\lambda$ of the LD. Secondly, the LD pulse energy calculated with the values of Table 5.1 using Equation 2.29, was 6 pJ. The saturation energy of the amplifier at 2051 nm was calculated with Equation 2.26 to be 13 μJ, where the cross sections were taken from Figure 2.7 at 2050 nm to be $\sigma_{em} = 2.8 \times 10^{-25}$ m^2 and $\sigma_{abs} = 0.85 \times 10^{-25}$ m^2. ν_s was calculated using Equation 2.2 at vacuum speed of light. The mode area was taken as the fiber core area $\pi d^2_{core}/4 = 5 \times 10^{-11}$ m^2. The pulse energy being four orders of magnitude lower than the saturation energy, the steady-state solution was chosen.

The parameters of the amplifier to be optimized were:

1. Pump power P^{in}_p, using one or two pump LDs, each emitting continuously provides an input power up to 300 mW, which is within the limits of the pump LDs (Figure 4.5). This gives a total pump input power up to 600 mW in the case of two pump diodes. Pump diodes may pump the active fiber in the forwards (in the same direction as the signal), or backwards (in the opposite direction to the signal) direction. The pump LDs emit at 1150 nm where holmium was seen to absorb in Figure 2.4.

2. Active fiber type, or essentially the holmium doping concentration N_{Ho}. Three different fiber types provided by iXblue (IXF-HDF-PM-8-125), Nufern(SM-HDF-10-130), CorActive (custom made), differing primarily in doping concentration, which may be viewed in Table 5.2 were considered.

	N_{Ho} 10^{25} m^{-3}	d_{core} μm	d_{clad} μm	NA	τ ms	passive loss$_s$ dBm^{-1}	passive loss$_p$ dBm^{-1}
iXblue	6 (5)	8	125	0.16	0.7 (0.55)	0.01	0.001 (0.01)
Nufern	5.36	10	130	0.15	0.6	0.1	0.1
Coractive	1.93	9	-	0.15	0.6	0.1	0.2

Table 5.2: Doping concentration N_{Ho}, numerical aperture NA, core and cladding diameters d_{core} and d_{clad}, and passive losses of signal s pump p power announced by the manufacturers of the three fibers available. Values in parentheses are tuned after testing of amplifier.

3. Fiber length L

Additionally, spectroscopic parameters of the fiber such as upper laser level lifetime and pump and signal passive losses, provided by the fiber manufacturers, may be improved, so that the model fits experimental data better.

5.2.2 Determining number of pump diodes (pump power) and active fiber type and length

To be determined is which active fiber to choose for the amplifier, as well as whether to pump the active fiber with one pump LD (P_p^{in} = 300 mW) or two pump LDs (P_p^{in} = 600 mW). For every possible fiber type / number of pump LDs combination, the amplification of the master oscillator LD emitting in pulsed mode (P_s^{in} = 0.6 μW average power) or CW mode (P_s^{in} = 6 mW average power). Table 5.3 shows the simulated results for every such fiber type/ pump power/ signal power combination. L is the fiber length providing highest total gain G of the signals.

	P_p^{in} = 300 mW, P_s^{in} = 6 mW			P_p^{in} = 600 mW, P_s^{in} = 6 mW		
	iXblue	Nufern	CorActive	iXblue	Nufern	CorActive
L (m)	.65	.45	1.4	.75	.75	2.3
G (dB)	7.9	4.4	5.1	14	11	11
η (%)	10	3.5	4.5	24	12	12
	P_p^{in} = 300 mW, P_s^{in} = 0.6 μW			P_p^{in} = 600 mW, P_s^{in} = 0.6 μW		
	iXblue	Nufern	CorActive	iXblue	Nufern	CorActive
L (m)	.75	.45	1.5	1.3	.85	2.8
G (dB)	12	5.2	6.3	29	16	18
η (%)	3×10^{-3}	0.4×10^{-3}	0.6×10^{-3}	8×10^{-3}	4×10^{-3}	6×10^{-3}

Table 5.3: Simulated results for the three different fibers iXblue, Nufern, CorActive amplification of a signal of 0.6 μW and 6 mW average power at 2051 nm, when pumping with 300 mW (one pump diode) or 600 mW (two pump diodes). Optimal fiber length L, total gain G and residual pump power P_p^{out} are shown.

When doubling pump power from 300 mW to 600 mW, total signal gain G increased with more than 6 dB for all combinations. Absorption saturation discussed in Figure 2.3.6 does not seem to have taken place in any of signal/fiber type combinations. Thus, pumping with two pump diodes is beneficial.

The iXblue active fiber outperformed the other fiber types in terms of total signal gain G and efficiency η for all signal power/ pump power combination.

Choosing the iXblue fiber, pumped by two pump diodes continuously providing a total of 600 mW pump power P_p^{in}, Figure 5.1 shows how the signal output power (blue curve) of the pulsed LD varies when varying the total fiber length L between 0 and 2 m. Residual pump power to be absorbed by the isolators shown in Figure 3.2 (red curve) is also shown. P_s^{out} peaks to 480 μW corresponding to a gain of 29 dB with total fiber length L = 1.25 m.

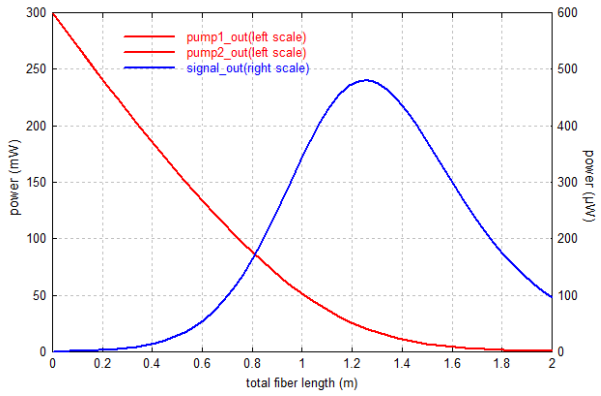

Figure 5.1: The signal output power P_s^{out} (blue curve) and residual pump power P_p^{out} (red curve) depending on total fiber length L, in the case of 2 pump diodes, each emitting 300 mW at 1150 nm, for input signal of 0.6 μW at 2051 nm.

5.2.3 Final design of the power amplifer

The power amplifier was built was built using the length of $L = 1.4$ m of the iXblue active fiber, and two pump diodes emitting 300 mW at 1150 nm, as seen in Figure 3.2.

Figure 3.2 emphasizes that the power amplifier is a stand alone device that takes an input signal and provides an amplified output as long as the laser signal input wavelength overlaps with the gain of holmium.

5.3 Modelled behaviour of the Power Amplifier

The finalized amplifier was tested, as will be discussed in chapter 6. Using experimentsl results, the model could be improved, and can then be a practical tool in understanding the advantages and limitations of the amplifier, and to predict MOPA configuration outputs.

This section first summarizes the changes done to the model after initial experimental tests. Then it compares the simulated behaviour of the LD-MOPA and the mode-locked-MOPA, by looking at signal, pump and ASE output power as well as population inversion ratios at full amplification. Then total gain when varying pump power for different signal input powers is considered. The effect of varying the LD tunable parameters on the LD-MOPA output is simulated. Finally residual pump power in the case where either master oscillator should fail is simulated.

5.3.1 Tuning of the power amplifier model

Due to some technical problmes with the LD, the power amplifier was tested in the mode-locked-MOPA configuration shown in Figure 3.1b. To improve the numerical model, the results from experiments shown in Figure 6.1a (signal amplification) and Figure 6.1b (residual pump power) were considered. The numerical model input doping concentration N_{Ho}, lifetime τ and passive losses tabulated in Table 5.2 were adjusted to the values in parenthesis in order to fit the simulated (purple) curves, to the experimental (blue) curves. chapter 6 will also argue that the steady-state numerical model is valid for describing for amplification of the mode-locked oscillator output.

5.3.2 Pump and signal and Amplified Spontaneous Emission (ASE)

Predicted total gain G efficiency η for the 0.6 μW average power pulsed LD signal at 2051 nm and the 0.5 mW average power pulsed mode-locked signal at 2085 nm are provided in Table 5.4. The 0.6 μW signal has higher gain and lower efficiency than the the 0.5 mW signal.

Master Oscillator	λ_s nm	$P^{in}_{s,avg}$	$P^{out}_{s,avg}$	G dB	P^{in}_p mW	P^{out}_p mW	η %
LD	2051	0.6 μW	80 μW	21	600	30	0.01
mode-locked	2089	0.5 mW	30 mW	18	600	24	5

Table 5.4: Amplifier performance parameters gain G and efficiency η for the two master oscillator sources: a pulsed LD signal at λ_s of 2051 nm and a pulsed mode-locked signal at λ_s of 2089 nm.

Figure 5.2 shows pump and signal power, and also integrated ASE power, as discussed in subsection 2.3.7, at different positions x along the fiber for the (a) 0.6 μW signal at 2051 nm and (b) 0.5 mW signal at 2089 nm.

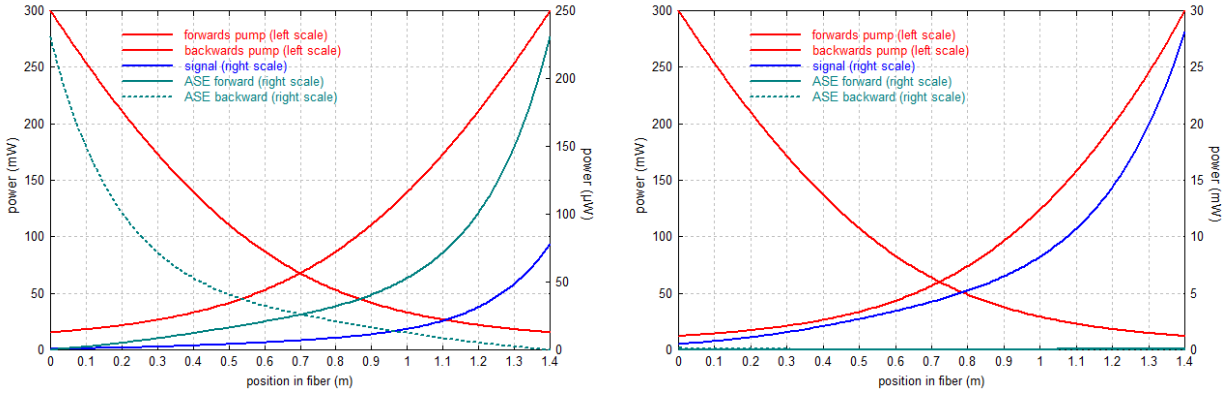

Figure 5.2: Pump, signal and ASE power a distance x into the fiber of total length 1.4 m, for the case of 2 pump diodes, each emitting 300 mW at 1150 nm, for input signal (a) of 0.6 μW at 2051 nm and (b) of 0.5 mW at 2089 nm.

The ASE power level is the integrated contributions from ASE at all wavelengths within the gain range of holmium. The 0.6 μW signal at 2051 nm (Figure 5.2a) is small in comparison with the ASE noise. The 0.5 mW signal at 2089 nm signal (Figure 5.2b) is always stronger than the ASE.

Theses considerations indicate that amplifying signals of sub μW average power would not be efficient/feasible/advisable. Already at 0.6 μW signal strength, noise in the form of ASE is draining the energy which more idealy should be amplifying the signal. If further amplification should be required, an optical filter at the end of the fiber should be added to filter out ASE noise, before the potential second stage amplifier.

5.3.3 Level populations

The fractional population, as defined in Equation 2.25, of the upper n_2 and lower n_1 laser levels a distance x into the fiber is shown in Figure 5.3. Two pump diodes pumping from each side of the fiber, excite ions in the active fiber out of the ground state to the upper laser level. At the center of the fiber total pump power is too weak to maintain a total population inversion of the two levels, and $n_2 < n_1$. Equation 2.25 shows $n_2 > 0.5$ can be expected

in holmium-doped fiber pumped at $\lambda_p = 1150$ nm, [23] attributes this to the relatively fast relaxation time between the $^5I_6$ and $^5I_7$ levels depicted in Figure 2.8 of holmium in silica fiber.

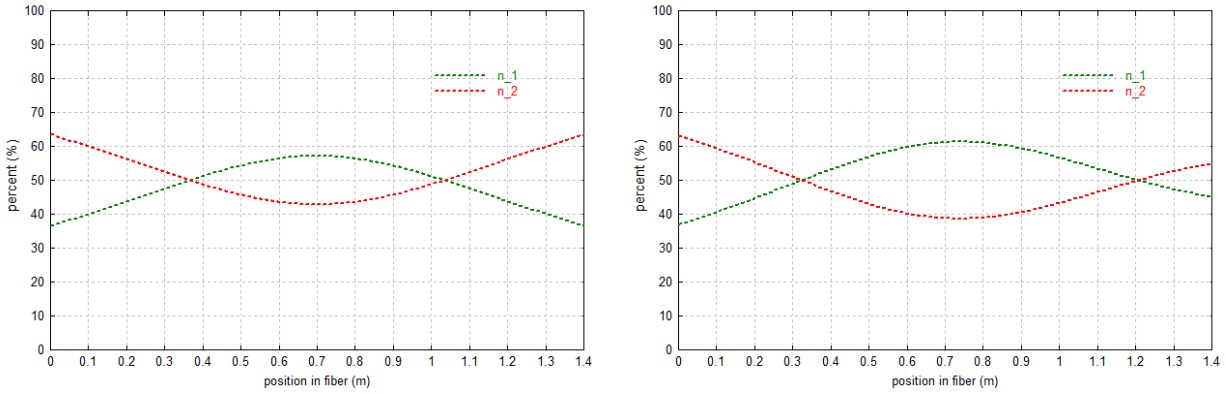

Figure 5.3: Fractional population (given in %) of the upper n_2 and lower n_1 laser levels a distance x into the fiber of length $L = 1.4$ m, for the case of 2 pump diodes, each emitting 300 mW at 1150 nm, for input signal (a) of 0.6 μW at 2051 nm and (b) of 0.5 mW at 2089 nm.

The amplification of the master oscillator LD of $P_s^{in} = 0.6$ μW average power is merely a disturbance to the much stronger 300 mW pump power, and does not change the symmetry as seen in Figure 5.3a. The mode-locked laser signal of $P_s^{in} = 0.5$ mW entering the active fiber from the left. From the center of the fiber and on, the signal power exceeds half the total pump power as seen in Figure 5.2b. This accounts for the asymmetry of the population inversion at the start and end of the fiber.

Together with the effective cross section curves drawn for n_2 in Figure 2.9, Figure 5.3 reveals if at any point x in the fiber the signal is being amplified or attenuates. Figure 2.9 shows that at 2051 nm $n_2 = 0.3$, and at 2085 nm $n_2 = 0.2$ is necessary for having positive gain. Figure 5.3a predicts n_2 at 2051 nm to always be greater than 0.4 (40%), and Figure 5.3a shows that at 2085 nm n_2 stays above 0.2 (20%) throughout the whole length of the fiber. Hence, there are no points in the fiber where either signal attenuates. This is reflected in Figure 5.2 where both signals are monotonously increasing with distance into the fiber.

5.3.4 Variation of total gain with pump power

Figure 5.4 shows the dependence of the total gain G (in dB) on the pump power for the master oscillator LD of $P_s^{in} = 0.6$ μW signal at 2051 nm (blue curve) and the mode-locked laser of $P_s^{in} = 0.5$ mW at 2089 nm (green curve).

Gain for the 0.5 mW signal is also less sensitive to pump power, than the 0.6 μW signal. Flattening of the gain curve, as well as the asymmetry in the upper state population of Figure 5.3b shows that there will be an upper limit in signal input power for which the limited pump power can provide gain.

Pump power threshold for positive gain is wavelength dependent. The effective cross section curves drawn for n_2 in Figure 2.9 show that smaller upper level populations n_2 are needed for longer wavelengths to obtain positive gain. Indeed, Figure 5.4 shows that the shorter wavelength (2051 nm) master oscillator LD has a higher threshold power at 250 mW than the longer wavelength (2089 nm) mode-locked laser which has positive gain at input powers above 175 mW.

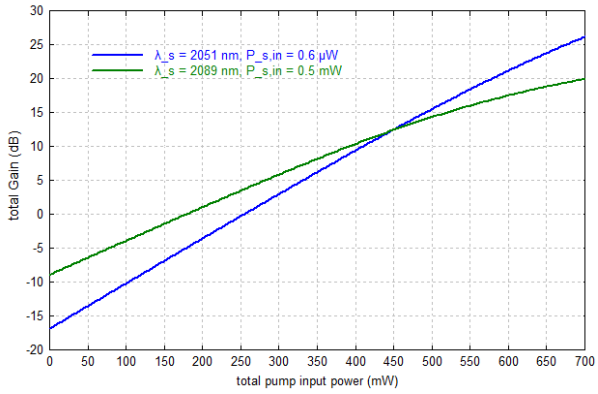

Figure 5.4: Total gain G (in dB) depending on total pump power in a fiber of total length 1.4 m, for the case of 2 pump diodes, each emitting at 1150 nm, for input signal (blue) of 0.6 μW at 2051 nm and (green) of 0.5 mW at 2089 nm.

5.3.5 Peak power when varying LD repetition rate and wavelength

The characterizations of the master oscillator LD of section 4.1 showed that the LD is easily tunable in repetition rate f_{rep} between 10 and 100kHz. And in signal wavelength λ_s between 2051 nm and 2053 nm.

Figure 5.5 shows the simulated dependence on output peak power P_{peak} on repetition rate f_{rep} under full amplification P_p^{in} = 600 mW, when operated at λ_s at 2051 nm (blue curve), 2052 nm (green curve) and 2053 nm (red curve). f_{rep} cannot directly be varied in the steady-state model adopted, as the model only takes the average signal power P_s^{in} as input. However, P_s^{in} was inputted according to Equation 2.28, when f_{rep} was varied between 10 and 100 kHz. Similarly, the peak power plotted in Figure 5.5 is recalculated using Equation 2.28 from the average power outputted by the model.

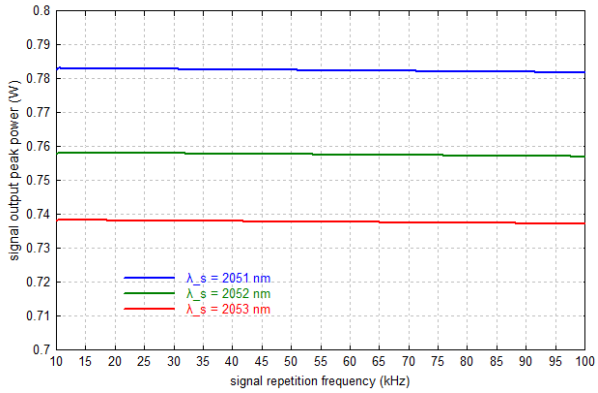

Figure 5.5: Amplified peak power P_{peak} depending on the input repetition frequency of the signal in a fiber of total length 1.4 m, for the case of 2 pump diodes, each emitting at 1150 nm, for input signal (blue) of 0.6 μW at 2051 nm and (green) of 0.5 mW at 2089 nm.

Within this range of f_{rep}, at all considered λ_s, the amplification of peak power varied less than 0.2%, and can be considered constant. This implies that the energy of each pulse is amplified equally independently of how many pulses are being amplified per second within this range of f_{rep}.

5.3.6 Residual pump power

It is also of importance to simulate how much residual pump power must be absorbed by the upper right and lower left isolators in Figure 3.2 in the case that the master oscillator should fail, and input no signal to the power amplifier. Residual pump power above the damage threshold of the isolators may lead to a breakthrough at the isolators, causing feedback of pump power into the pump diodes which may be harmful to them.

Two pump diodes, each emitting 300 mW, L = 1.4 m are simulated to produce 11.1 mW output power at either isolator in the absence of a signal. The isolators in question are made to withstand 500 mW [74, 75].

5.4 Summary of the main results from the numerical model

This chapter designed a power amplifier. The amplifier is tested as discussed in the following chapter 6, and the numerical model could be fitted to the experimental data. The improved model has provided several valuable insights on the behaviour on the amplifier, where the two most important are:

Firstly, the range of signals with respect to their average power, for which the amplifier is suited could be suggested. Bellow μW average power ASE drains the pump energy as seen in Figure 5.3a. With increasing average input signal power, the total gain curves plotted in Figure 5.4 with respect to pump power tend to flatten. Thus, a range of μW to a few mW average input power seems to be the feasible range of amplification.

Secondly, expected optical output of the MOPA system consisting of a master oscillator LD and the power amplifier was modelled and plotted in Figure 5.5. These parameters will be used to estimate LiDAR parameters in chapter 7.

Next up is the experimental results and discussion of the testing of the amplifier.

Chapter 6

Testing the Power Amplifier

Due to some technical difficulties experienced with the LD, the LD-MOPA shown in Figure 3.1a could not be demonstrated for this thesis. However, the power amplifier was implemented as part of the mode-locked-MOPA shown in Figure 3.1b. This chapter provides the experimental method, results and discussion of tests done with the mode-locked-MOPA system.

6.1 Experimental method

The mode-locked-MOPA as shown in Figure 3.1b was tested in the configuration where the master oscillator was a mode-locked holmium-doped fiber laser as characterized in section 4.2. The laser emitted pulses at about 3 picosecond pulse duration at a repetition rate of 3.81 MHz. The emission was centered at at λ_s = 2088.90 nm with a line width of $\Delta\lambda$ = 1.62 nm. The signal had an average power of 0.5 mW. Calculated pulse energy using Equation 2.28 and Equation 2.29 is then 0.13 nJ.

Two experiments were carried out. First, gradually increasing the pump power from 215 mW to 610 mW, the mode-locked-MOPA output was characterized in terms of average power, optical spectrum and temporal profile. Secondly, the master oscillator and one pump LD were disconnected, and residual pump power P_p^{out} from the other pump LD was detected. In both experiments, the amplifier pump power was controlled by setting the pump LD current, using the CW LD drivers, as explained in section 4.3. Total pump input power P_p^{in} was taken as the sum of the contributions from both pump LDs, as plotted in the power-to-current curve in Figure 4.5.

The amplifier signal output was characterized as follows. The average output power was measured by a power meter. The error of the power meter is about 1%, or 0.1 mW at the lowest. The optical spectrum was monitored using an optical spectrum analyzer. The temporal output was measured by an in-house built autocorrelator, as the picosecond pulse duration of the mode-locked laser is too fast to be measured with any available photodetector.

6.2 Results

This section presents the amplified output power of the mode-locked-MOPA and residual pump power. Temporal and spectral properties are provided at medium and full amplification.

6.2.1 Output power

The mode-locked-MOPA average output power from the first experiment was plotted against applied pump power P_p^{in} as shown in Figure 6.1a (blue curve). In the second experiment, the residual pump power P_p^{out} from one pump LD was plotted against P_p^{in} as shown in Figure 6.1b (blue curve).

Figure 6.1a shows that the amplifier operated with a slope efficiency η_s of 10% from the onset of linear output regime starting at about 450 mW applied pump power. At maximum amplification of 610 mW applied pump power, the optical-to-optical efficiency η was 5.3%. Figure 6.1b shows that if the amplifier should run at full amplification, and there should be no input signal, the residual pump power to be absorbed at either isolator in Figure 3.2 would not exceed 3.5 mW which is well below the 500 mW the isolators can withstand [74, 75], and there would be no damaging feedback into the pump LDs.

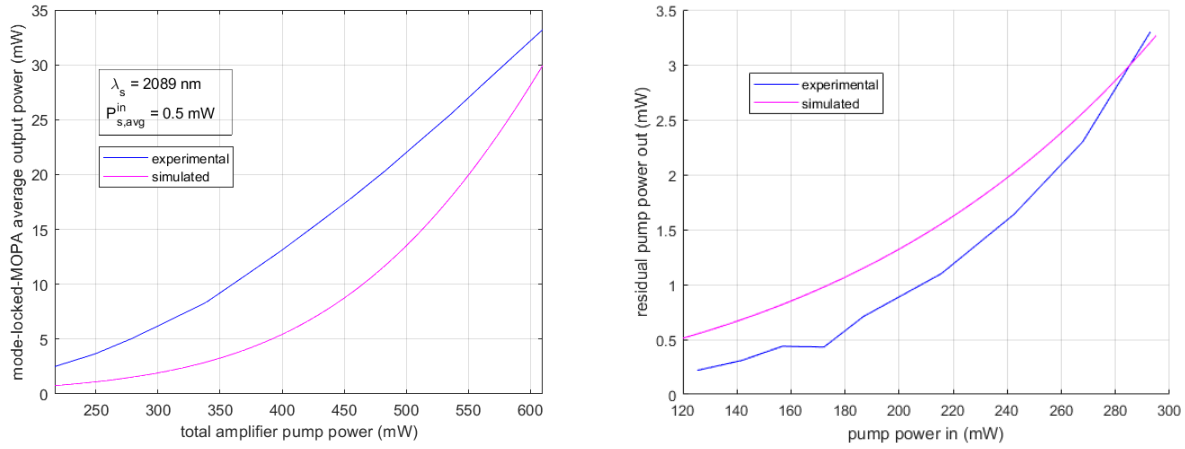

(a) (b)

Figure 6.1: (a) Measured (blue) and simulated (purple) average mode-locked-MOPA output power P_s^{out} depending on total amplifier pump power P_p^{in}. (b) Measured (blue) and simulated (purple) residual pump power P_p^{out} depending on pump power P_p^{in}.

6.2.2 Medium amplification

At 340 mW applied pump power, the mode-locked-MOPA emitted 8 mW average output power corresponding to 12 dB total gain. The optical spectrum centered at $\lambda_s = 2088.8$ nm with a linewidth of $\Delta\lambda = 1.41$ nm is shown in Figure 6.2a. In this regime, the output power was sufficient to successfully measured the pulse to have a duration Δt of 3.2 ps as seen from Figure 6.2b. According to Equation 2.28, the calculated pulse peak power P_{peak} is 690 W, and according to Equation 2.29 the pulse energy is 2 nJ.

The time-bandwidth product (left side of Equation 2.4)of the pulse from the mode-locked-MOPA is equal to 0.31. For pulses of sech^2 profile, the constant ofEquation 2.4 is 0.315 for[33, p. 10], which is reasonably close to 0.31. This shows that the pulse from the oscillator is almost transform limited.

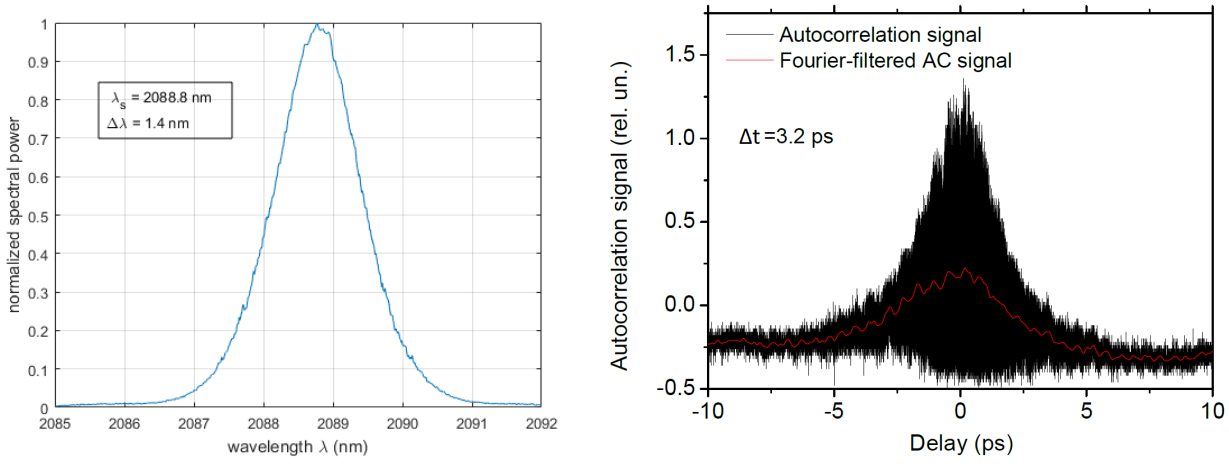

(a) (b)

Figure 6.2: Mode-locked-MOPA signal output of 8 mW average power at pump power of 340 mW. The (a) optical spectrum is centered around $\lambda_s = 2088.8$ nm with a line width of $\Delta\lambda = 1.41$ nm and (b) autocorreolation trace with pulse widh $\Delta t = 3.2$ ps.

6.2.3 Full amplification

Further increasing THE pump power, the linewidth broadened noticeably up to 2.97 nm at 510 mW applied pump power, marking the end of a single peak spectral regime. When applying pump power beyond this point, the spectrum gradually split in two distinct peaks.

At full amplification, when pumping with 610 mW, the 33 mW average output power corresponding to a gain of 18 dB was obtained. The optical spectrum centered at 2089 nm seen in Figure 6.3a, had split into two peaks. The linewidth $\Delta\lambda$ = 6.6 nm was taken as the full width of both peaks at half maximum value of the tallest peak. Temporally, the pulse split into a group of several pulses as seen in Figure 6.3b, with a duration of the pulse group estimated to be < 10 ps.

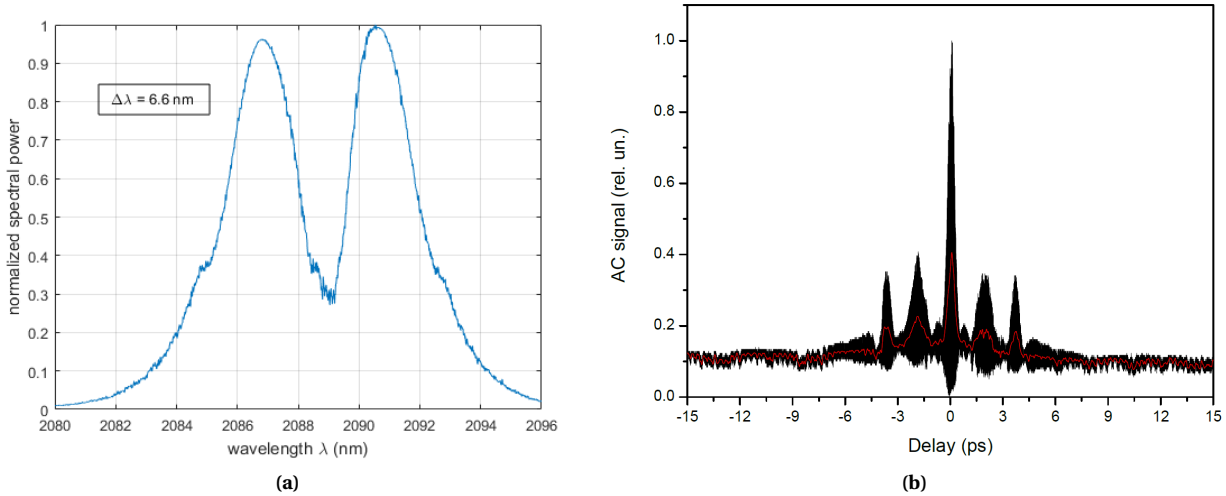

(a) (b)

Figure 6.3: Mode-locked-MOPA average power output of 33 mW at 610 mW applied pump power: (a) optical spectrum centered around 2089 nm with a linewidth $\Delta\lambda$ = 6.6 nm. (b) Autocorreolation trace showing the pulse splitting. The duration of the pulse group as a whole is estimated to be < 10 ps

6.3 Discussion

The holmium-doped fiber amplifier was successfully demonstrated. Amplification to 12 dB without spectral and temporal broadening was achieved from the mode-locked holmium-doped fiber laser picosecond pulsed input signal at 2089 nm, of 0.5 mW average power. At full amplification, 18 dB gain was obtained for the same input signal, however the pulse had then split up into a train of pulses, and the spectrum broadened to 6.6 nm.

Here follows a discussion the efficiency, the validity of the amplifier numerical model for this mode-locked-MOPA configuration, and finally the main advantages of the power amplifier itself.

6.3.1 Efficiency

The optical-to-optical efficiency η and slope efficiency η_s depend not only on the fiber amplifier configuration, but also on the input signal parameters. The quantum defect limited efficiency η_q of the mode-locked MOPA operating at signal wavelengths λ_s =2089 nm and pump wavelength λ_p = 1150 nm is 55% according to Equation 2.36, using Equation 2.2 and assuming that the speed of light in the fiber is equal at both λ_s and λ_p. The optical-to-optical efficiency η observed at full amplification was 5.3%, which is still one order of magnitude lower than η_q. Also the

slope efficiency η_s of 10% is five times lower than η_q. The remaining power is dissipated as heat in the fiber or in the isolators. Cooling of the fiber was not necessary due to the fiber geometry discussed in subsection 2.2.1.

Pumping at a wavelength λ_p in an absorption band centered at 1950 nm and closer to λ_s as seen in Figure 2.4 would reduce the quantum defect discussed in Equation 2.3.6 and increase optical-to-optical efficiency η. η_q would increase to 93 %. State-of-the-art commercially available LDs operating within this absorption band deliver around 15 mW average power [27]. Simulated threshold pump power for the mode-locked laser of this mode-locked-MOPA, as well as the LD-MOPA were simulated to 175 mW and 250 mW respectively as seen in Figure 5.4, indicating that state-of-the-art LDs can not directly be used as pump LDs in the 1950 nm absorption band for the amplification of μW-mW signals.

6.3.2 Comments on the validity of the amplifier numerical model

The complementary amplifier numerical model is a practical tool in predicting amplification of inputted signals. Fitting the model to experimental data increases its trustworthiness. As the experiments showed a tendency of spectral broadening, a discussion on the validity on the numerical model in describing the amplification of the mode-locked laser is included. Specifically, the three requirements for adopting a CW model for pulsed amplification given in subsection 2.3.5 are looked at.

First, the saturation pulse energy E_{sat} at λ_s = 2089 nm is 17 μJ according to Equation 2.26. Cross sections are plotted in Figure 2.7, and the mode area A is taken to be the core area $\pi d_{core}^2/4$. The input pulse energies were seen in section 6.1 to be 0.13 nJ and the pulse energy at maximum amplification 2 nJ. The pulse energies are well below E_{sat}, and assumption number one is fulfilled.

Secondly, gain is proportional to the effective cross section plotted in Figure 2.9, which can be said to be constant across the input linewidth $\Delta\lambda$ = 1.41 nm of the mode-locked laser found in section 4.2. Thus, requirement number two is satisfied.

The third assumption considers broadening of amplifier output during amplification. While amplifying with up to 610 mW pump power, the the laser spectrum remained centered around λ_s = 2089 nm. The linewidth $\Delta\lambda$ broadened four times from the mode-locked laser initial output of 1.62 nm to full amplification mode-locked-MOPA output of 6.6 nm. Around 2089 nm, the effective cross section can be considered constant also across a 6.6 nm linewidth. The considered curves in Figure 2.9 were the n_2 = 0.4, n_2 = 0.5 and n_2 = 0.6 curves, accroding to the simulated level populations at full amplification shown in Figure 5.3b. Therefore, the observed broadening does not violate assumption number three.

Thus, the model can still be seen as valid for the entire range/stretch of amplification for this particular mode-locked-MOPA system. The numerical model of the amplifier was improved as discussed in subsection 5.3.1, using experimental data from amplification, as well as the residual pump characterization. The simulated output power/amplification (purple curve in Figure 6.1a), and residual pump power (purple curve in Figure 6.1b) nicely match the experimental results. Important results on the behaviour of the amplifier were also found with the improved numerical model, and could be presented in chapter 5.

Developing a complementary pulsed numerical model for amplification of master oscillators where the CW model should not be valid would be an important further step in this work.

6.3.3 Advantages of the amplifier

The demonstrated power amplifier has a number of advantages. Being single-mode diode-pumped and having all-fiber design, it is potentially very compact, and can easily be integrated into a more complex system. It has received its own packaging measuring 2 cm x 14 cm x 25 cm.

Due to the broad gain bandwidth of Holmium, it can be used for amplification of any signal between 2000 nm and 2150 nm, where the region above 2050 nm is of most interest due to limited gain of Thulium in that spectral range [23, 77]. An additional advantage is that it was assembled using only PM fiber components, and can therefore be combined with polarized input laser sources [41].

Stable in operation, it has proven to be a stand alone, practical device within the lab. The development resulted in a conference paper [73].

6.4 Outlook and End note

Providing positive gain within the beginning of the 2-2.5 μm atmospheric window, the power amplifier, when integrated in a MOPA system, has the potential of being the laser source of a LiDAR. This chapter ends by stating the regime of operation considered for the mode-locked-MOPA and the LD-MOPA as LiDAR laser sources.

The mode-locked-MOPA operated at both medium and full amplification could be chosen as operation regimes for the LiDAR application. For the following reasons the regime at medium amplification as been selected. At medium amplification the pulses were shorter, the spectrum narrower, but the average power lower than at full amplification, where the output also split into a train of pulses. The following chapter will estimate LiDAR parameters considering the interplay of noise power and detector rise time with the output of a MOPA assumed to posses a well defined peak power and pulse duration. The regime at medium amplification provides such output. However, if it should become apparent that more average power is beneficial, the mode-locked-MOPA could be operated at full amplification, where the group of pulses would be seen as one pulse of effective width of < 10 ps.

The amplifier numerical model aligned nicely with experimental results from the testing with the mode-locked laser. This justifies estimating potential range finding LiDAR parameters with the LD-MOPA using parameters from the simulations in chapter 5. The LD is tuneable in wavelength λ_s and repetition rate f_{rep}, which is generally interesting for LiDAR application. The LD-MOPA configuration considered in chapter 7 will be fixed at λ_s of 2051.81 nm, pulse duration Δt of 1 ns and finally peak power of 0.8 W simulated to be independent of f_{rep}.

Having chosen a regime of operation for both the mode-locked-MOPA and the LD-MOPA, chapter 7 will discuss their viability as laser sources in LiDAR applications in more detail.

Chapter 7

Designing and building the range finding LiDAR

In order to carry out a proof of principle range finding LiDAR experiment using the mode-locked-MOPA demonstrated in chapter 6 as laser source, the LiDAR setup shown in Figure 3.3 was assembled and is looked at closer in this chapter. To settle on the setup shown in Figure 3.3, LiDAR setups based on calculated range-finding LiDAR parameters for both the mode-locked-MOPA, and the potential LD-MOPA were considered and compared. A project work [78], describing the development of a similar range-finding setup, as well as a Ph.D. thesis [13] developing a cloud height-finding ceilometer, both operating at around 1.5 μm were of great help in this work.

This chapter first considers the LiDAR transmitter components, and then describes the calculations behind choices of LiDAR receiver components. Finally a solution for keeping track of return time is presented.

7.1 Transmitter

A close up of the LiDAR transmitter optics are shown in Figure 7.1.

This section first considers the two possible MOPAs in the context of LiDAR laser transmitters, and then describes the outputting collimator.

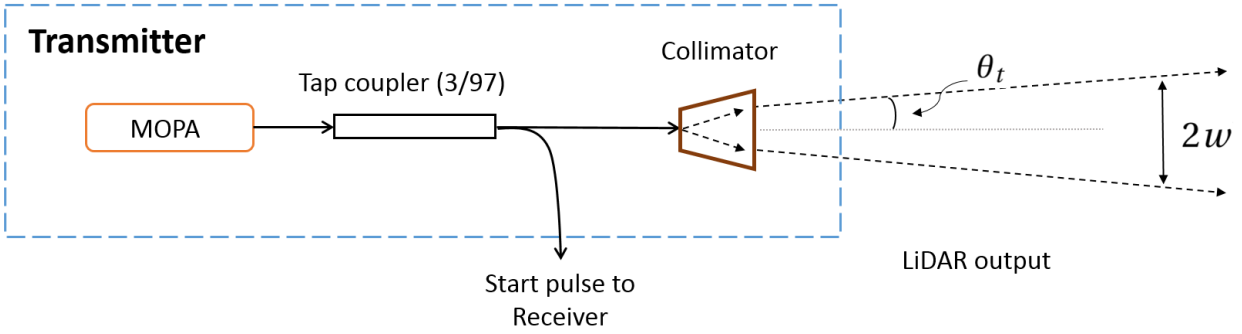

Figure 7.1: Close up of the LiDAR transmitter. The MOPA generates a pulse split at the Tap coupler, 3% is guided to the receiver, and 97% to the collimator which expands and collimates the LiDAR output as a free space beam diverging at an angle θ_t. The beam waist diameter $2w$ is range-dependent.

7.1.1 MOPA as transmitter laser source

The LiDAR transmitter parameters using either MOPA as transmitter laser source are tabulated in Table 7.1. The parameters of the mode-locked-MOPA were taken from the experimental results of chapter 6. As discussed in section 6.4, the LD-MOPA parameters could be taken from from section 4.1, except for the peak power which was simulated using the improved numerical model of the power amplifier as seen in Figure 5.5.

It was stated in the introduction (chapter 1) that the $2-2.5$ μm is the ideal window for remote sensing [7] for a number of reasons, which the two considered MOPAs benefit from.

Transmitter parameters with MOPA laser source	P_{peak} W	Δt	f_{rep}	θ_t mrad	λ_s nm	$\Delta\lambda$ nm
LD-MOPA	0.8	1 ns	$10-100$ kHz	1.04	2051.00 - 2053.00	0.05
mode-locked-MOPA	630	3.2 ps	3.81 MHz	1.04	2088.8	1.4

Table 7.1: Experimentally measured output parameters (except peak power P_{peak} of the LD which is modelled and taken from Figure 5.5) of the transmitter when using the LD-MOPA or mode-locked-MOPA as laser source. θ_t is always the divergence angle of the Thorlabs collimator.

It was said that the atmospheric transmittance due to absorption was relatively high within this spectral range. The LD-MOPA is tunable in wavelength λ_s around 2.05 μm, and exhibits a linewidth $\Delta\lambda$ which fits inside and between the absorption lines within this wavelength range as seen in Figure 7.2a. For range-finding calculations done in this chapter, a LD-MOPA wavelength at $\lambda_s = 2051.81$ nm is assumed. Although the mode-locked-MOPA has a broader linewidth than the LD-MOPA, it can still be used for ranging because the wavelength range in which it emits is transparent over much broader wavelength bands than around 2052 nm as seen in Figure 7.2b.

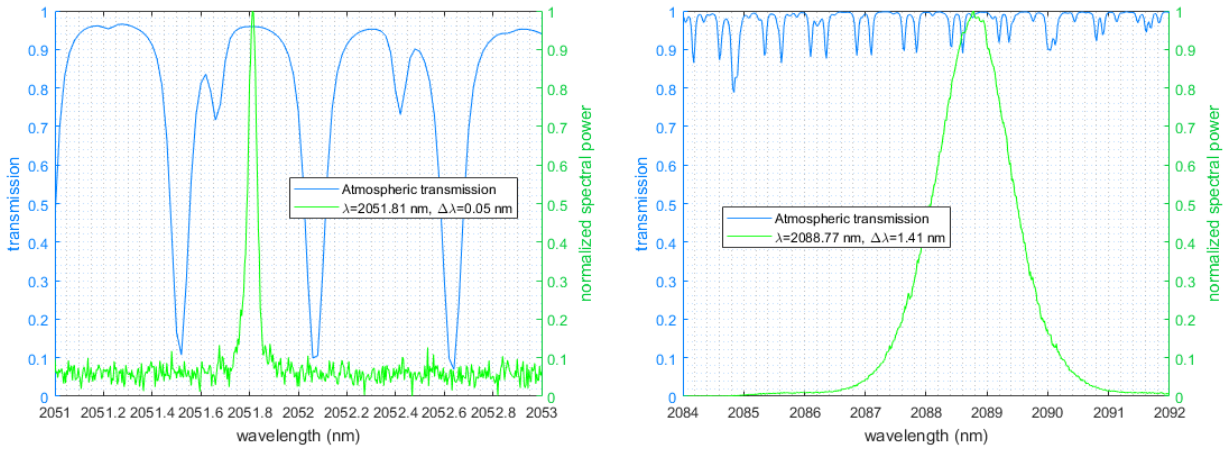

(a) **(b)**

Figure 7.2: Spectral atmospheric transmittance due to absorption (blue curves). Plotted with data from [15]. Coplotted are the spectral outputs of the range finding LiDAR transmitter when the laser source is (a) the LD-MOPA at 2051.81 nm (green curve) from Figure 4.2a, and (b) the mode-locked-MOPA emitting at 2088.8 nm (green curve) from Figure 6.2a.

Both MOPAs are pulsed sources needed for the pulsed TOF method. They are electrically controlled, which in the introduction was considered favorable, with operation described in section 4.1 (LD-MOPA) and section 4.2(mode-locked-MOPA). The LD-MOPA allows setting of repetition rate f_{rep}, whereas the mode-locked-MOPA has a fixed repetition rate of 3.81 MHz. The mode-locked-MOPA outperforms the LD-MOPA in peak power P_{peak}, and has shorter pulse duration Δt. The implications of pulse duration Δt and peak power P_{peak} will be seen in the following sections.

Finally, the introduction also considered eye safe pulse energy. The pulse energies of the LD-MOPA and the mode-locked-MOPA are according to Equation 2.29 0.8 nJ and 2 nJ respectively. Theses are below the 20 mJ considered eye safe energy between $2-2.1$ μm [11]. Thus the potential LiDAR could be used in a public environment.

Thus, either MOPA exhibits properties favorable for LiDAR laser transmitter sources.

7.1.2 Collimator

The LiDAR must transmit a collimated beam of pulses as LiDAR output. The beam will diverge at transmitter divergence angle θ_t. Minimizing θ_t, would increase the maximal range R_{max} of the LiDAR system according to Equation 2.57, and increases transverse resolution $\Delta R^{\perp}$ according to Equation 2.50.

Transmitting the signal directly from the tip of the fiber of either MOPA with fiber core diameter $d_{core} = 8$ μm, would according to Equation 2.5 result in a 0.16 rad divergence angle θ_t 0.16 rad. This implies a 1 m beam diameter at 3.06 m distance according to Equation 2.50.

The transmitter divergence angle is lowered by guiding the MOPA output through a collimator (Thorlabs TC06FC-2000) with an angle of divergence $\theta_t = 1.04$ mrad when θ_t is defined like in Equation 2.41. With this solution, the beam diameter and thus $\Delta R^{\perp}$ will be 1 m at 480 m range. Thus, a collimator was installed in the LiDAR transmitter.

7.2 Receiver

The receiver is sketched in Figure 7.3.

This section discusses of the modelling of LiDAR parameters done to choose a detector, as well as how the return pulse as focused on the detector.

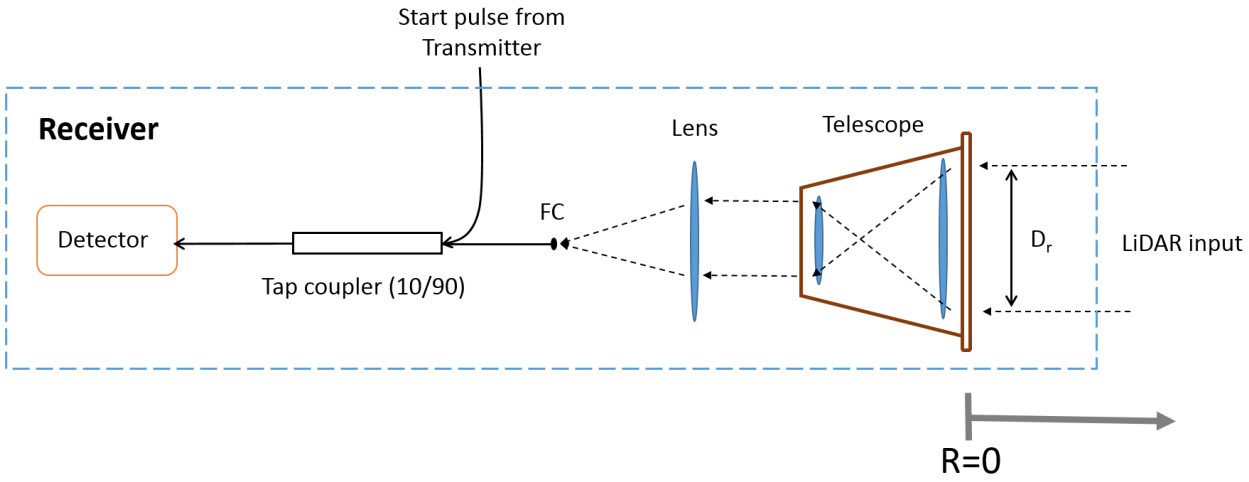

Figure 7.3: Close up of the LiDAR receiver. The telescope aperture is the receiver aperture D_r. A lens focuses the collimated output of the telescope into a fiber via a fiber coupler (FC). At the (10/90) Tap coupler the LiDAR input meets a pulse, which was guided directly from the transmitter. Both signals are detected by the fiber coupled Newport detector. The entrance of the telescope is defined to be the zero-range line where $R = 0$.

7.2.1 Telescope

The return pulse (LiDAR input) is collected by a Thorlabs (BE15M) Galilean telescope. Figure 7.3 The telescope entrance (or almost) is its aperture with diameter of 48 mm. In order for all the collected optical power to be transmitted to the detector through the receiver optics, the aperture D_r of the receiver should be the aperture of the telescope.

The LiDAR zero range ($R = 0$) line is chosen from the entrance to the telescope as illustrated in Figure 7.1.

7.2.2 Detector - chosen based on LiDAR range calculations

Three possible photodetectors Thorlabs PDA10D-EC, Hamamatsu G5853-23, and Newport 818-BB-51 were considered. Table 7.2 tabulates the detector parameters provided by the companies. Specifically, the detector rise times t_{rise}, were either given or calculated with Equation 2.47 if only the BW was provided.

Detector	spectral resp. μm	$\Delta_{\lambda,r}$ μm	BW MHz	t_{rise} ns	I_{dark} μA	NEP pWHz$^{-\frac{1}{2}}$	$\mathscr{R}(\lambda_s = 2.05\,\mu\text{m})$ AW^{-1}	$P^{det}_{noise} \sim P_{noise}$ μW
Thorlabs (PDA10D-EC)	1.2-2.6	1.4	15	23	-	35	1.1	0.136
Hamamatsu (G5853-23)	1.2-2.55	1.35	1.5	230	7.5	-	1.3	5.77
Newport (818-BB-51F)	0.83-2.15	2.32	12.5×10^3	28×10^{-3}	1	-	0.7	1.43

Table 7.2: Parameters of the three detectors estimated or provided by the manufacturers . The detector response interval $\Delta_{\lambda,r}$ is the width of the spectral response.

With 3 available detectors (Table 7.2) and 2 possible transmitter sources (Table 7.1), 6 possible LiDAR systems are considered. The maximal range R_{max} as well as range resolution ΔR and transverse resolution $\Delta R^{\perp} = 2w(R_{max})$ evaluated at R_{max} of every LiDAR system were estimated, and are tabulated in Table 7.3. By comparing the final results, the choice of the Newport detector could be made. In the following, the details on the calculations behind the parameters in Table 7.3 are presented.

LiDAR system with (transmitter/receiver)	$P_{r,min}(SNR_{min} = 10)$ μW	R_{max} m	$\Delta R^{\perp} = 2w(R_{max})$ m	ΔR m
LD-MOPA and Thorlabs PDA10D-EC	1.36	1316	2.7	3.6
LD-MOPA / Hamamatsu G5853-23	57.7	177.8	0.4	35.1
LD-MOPA and Newport 818-BB-51F	14.3	1611.6	3.3	0.15
mode-locked-MOPA + Thorlabs PDA10D-EC	1.36	39 (1575.7)	0.08 (3.3)	3.5
mode-locked-MOPA + Hamamatsu G5853-23	57.7	39 (250.0)	0.08 (0.5)	35.0
mode-locked-MOPA / Newport 818-BB-51F	14.3	39 (4562.5)	0.08 (9.5)	4.7×10^{-3}

Table 7.3: LiDAR parameters of the 6 possible MOPA/detector combinations. $2w_{max}$ is the transverse resolution at R_{max}. Whenever the LiDAR R_{max} is repetition rate limited, the hypothetical power limited R_{max} as well as the transverse resolution at that range is given in parenthesis.

Detector noise P^{det}_{noise} compared to background noise P^{BG}_{noise} calculations

In order to predict R_{max} of the LiDAR systems, the total noise level P_{noise} of Equation 2.52 is estimated for every detector.

First, background noise P^{BG}_{noise} seen by every detectors is estimated using Equation 2.53. A paper [61] took the power flux f in the spectral range between $2.3 - 4.5\ \mu$m to be 5×10^{-5} Wcm^{-2}sr$^{-1}\mu$m^{-1} at daytime under clear sky conditions. Consulting Figure 2.15b, here $f = 5 \times 10^{-4}$ Wcm^{-2}sr$^{-1}\mu$m^{-1} will be used, as all considered detectors have spectral response down to 1 μm. The receiver aperture area A_r is calculated from Equation 2.45 with the aperture diameter D_r given in subsection 7.2.1. The receiver FOV $\Omega_{FOV,r}$ depends upon the geometry the receiver optics [5, p. 5], and is estimated to be < 1 mrad^2. Finally, all detectors have detection range $\Delta_{\lambda,r} \leq 2.32\ \mu$m which is taken as $\Delta_{\lambda,r}$ in the calculation. Thus, Equation 2.53 equates to 20 nW which is a conservative estimate for P^{BG}_{noise} for all detectors.

Secondly, the detector noise P_{noise}^{det} of the three detectors was estimated using Equation 2.54 for the Hamamatsu and Newport detectors as the dark current I_{dark} and responsivity $\mathscr{R}$ was given. For the Thorlabs detector NEP was provided and Equation 2.55 was used. P_{noise}^{det} was calculated to be of μW order for all the detectors.

As, $P_{noise}^{BG} << P_{noise}^{det}$ by three orders of magnitude, P_{noise}^{BG} was neglected, and the total receiver noise power P_{noise} (Equation 2.52) was taken to be P_{noise}^{det} (in the following calculations on signal to noise ratios needed to estimate). This conclusion was also made by [61].

SNR calculations under assumed atmospheric conditions and target properties

Signal to noise ratio was calculated because it conveys information in itself, and is also as a step towards finding R_{max} of every LiDAR system.

SNR was was estimated with Equation 2.51 by comparing the received signal P_r returning from range R to the noise level P_{noise}^{det} of the various detectors and plotted against R in Figure 7.4a (LD-MOPA as transmitter laser) and in Figure 7.4b (mode-locked-MOPA as transmitter laser). P_r was calculated using Equation 2.46 under system conditions, atmospheric transmission and target properties listed in Table 7.4. These conditions will be looked at closer here.

Parameter	Value	Comment
D_r	48 mm	telescope aperture
θ_t	1.04 mrad	collimator divergence angle
η_{sys}	0.87	only tap coupler losses (see section 7.3)
$\mathscr{T}$	0.95	only atmospheric absorption, no scattering
ρ	1	full reflectance of the target
D_T	1 m	target diameter
SNR_{min}	10	minimum allowed SNR level

Table 7.4: Conditions assumed when calculating return power P_r with Equation 2.46 and power limited R_{max} with Equation 2.57.

The target is assumed to be an ideal mirror of reflectance $\rho = 1$ and diameter $D_T = 1$ m. This implies that the beam waist $2w$ equalled the target diameter D_T at range $R = (D_T/2)/\theta_t = 481.4771$ m. This range marks where P_r switches from a R^{-2} to a R^{-4} dependence, and is especially apparent from Figure 7.4a considering the SNR plot for the LD-MOPA/Hamamatsu detector LiDAR combination (orange curve). A singularity is seen at this range.

Regarding the atmospheric transmittance $\mathscr{T}$, the signal wavelengths λ_s have specifically been chosen to minimize absorption. Around 2051.81 nm and 2088.8, the atmospheric transmittance through the entire column of the atmosphere due to absorption amounts to around 0.95 as was seen in Figure 7.2a and Figure 7.2b. For this LiDAR, the number will likely be closer to 1, as the ranges considered here will be considerably shorter than the atmospheric height, and $\mathscr{T}$ increases with decreasing R as seen from Equation 2.60. Scattering generally lowers $\mathscr{T}$ further. Laser light at wavelengths λ_s between 2-2.1 μm will Rayleigh scatter off of atmospheric gases as λ_s is much greater than the molecular nanometer scaled diameters. Aerosols, rain, fog or snow are generally on the $\mu\text{m} - \text{mm}$ scale [8, p. 259], and the LiDAR signal would therefore Mie scatter off of theses as discussed in subsection 2.6.4. Estimates of scattering will not be calculated in this thesis. Restricting the calculations done here to a clear day, scattering is neglected and $\mathscr{T}$ is set to 0.95 for both laser sources.

Precise aligning of the receiver optics have been made in order to make η_{sys} ideal. Due to tap coupler losses, which will be considered in section 7.3, η_{sys} is set to 0.87.

Conditions on η_{sys}, $\mathscr{T}$, and ρ are the same for all the detectors, and do not affect their relative performance. However, estimates were made in order to enable the comparison between repetition rate limited R_{max} to the power

limited R_{max}. As only known factors are included in η_{sys}, $\mathcal{T}$, and ρ, the real power limited R_{max} will likely be somewhat shorter.

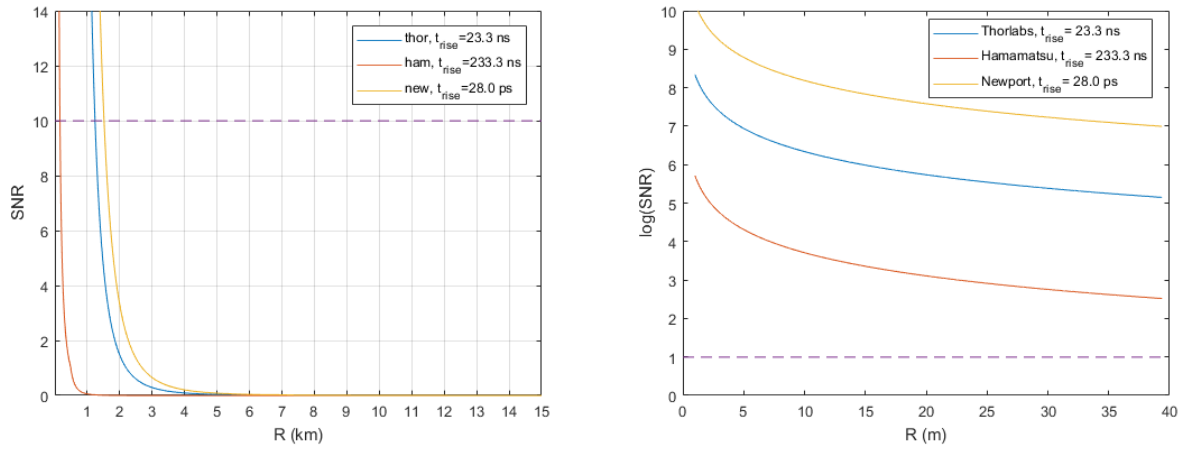

(a) **(b)**

Figure 7.4: (a) SNR of LiDARs with LD-MOPA, and (b) log(SNR) of LiDARs with the mode-locked MOPA. In (a) and (b), SNR is the return power $P_r(R)$ compared to P_{noise}^{det} of each detector. Assumed system parameters are tabulated in Table 7.3. The stippled lines in (a) SNR$_{min}$ = 10 and (b) log(SNR$_{min}$)=1 determine the power limited R_{max}. The R scales end at the repetition rate limited R_{max} which in (a) is 15 k(f_{rep} = 10 kHz) and in (b) is 39 m.

Estimating maximal range R_{max} of the LiDAR

Having calculated the SNR, the power limited R_{max} can be estimated by requiring a certain SNR$_{min}$, and can be compared to the repetition rate limited R_{max}.

A paper [79] developing an aerosol monitoring LiDAR, and a paper [80] looking at evolution of atmospheric water vapour using LiDAR data, both required SNR to be 10 at minimum. Therefore, SNR$_{min}$ =10 will be assumed here, and the smallest detectable and distinguishable optical power $P_{r,min}$ was estimated according to Equation 2.56. The power limited R_{max} were calculated with Equation 2.57.

The repetition rate limited R_{max} of the mode-locked-MOPA is to 39 m, whereas the LD-MOPA operated at at 10 kHz repetition rate would be limited at 15 km, as calculated with Equation 2.58.

Graphically, the power limited R_{max} is seen in Figure 7.4, as the range R at which the SNR curve of each detector/MOPA combination intersects the SNR = 10 or log(SNR) = 1 stippled lines. The horizontal axis of either graph is extended to the MOPA source repetition rate limited range. Thus if the SNR curves intersect the SNR = 10 line or log(SNR) = 1 line the true LiDAR R_{max} is power limited, whereas, if the curves do not intersect the stippled lines, the true LiDAR R_{max} is limited by repetition rate. Figure 7.4 shows that all LiDARS employing the mode-locked-MOPA have repetition rate limited R_{max}. All LiDARS employing the LD-MOPA have power limited R_{max}, as long as f_{rep} is adjusted properly. For example, the Newport detector / LD-MOPA LiDAR (yellow curve in Figure 7.4a) must adjust $f_{rep} < 90$ kHz in order to range to 1.6 km. The true R_{max} is tabulated in Table 7.3. Where R_{max} is repetition rate limited, the hypothetical power limited R_{max} is given in parenthesis.

Estimating LiDAR range resolution ΔR and transverse resolution $\Delta R^{\perp}$

Range resolution ΔR is proportional to the sum of rise time t_{rise} and pulse width Δt according to Equation 2.49, and are tabulated for all LiDAR combinations in Table 7.3. LiDAR ΔR with the mode-locked-MOPA is always limited

by the choice of detector. Only the Newport detector is faster than the LD-MOPA.

The transverse resolution $\Delta R^{\perp}$ given by Equation 2.50 depends equally on range R for all LiDAR system, as the transmitted pulse always diverges with θ_t. Thus for any of the LiDAR combinations, two of the considered targets (fully reflecting with diameter D_T = 1 m) will not be distinguishable as two different objects. $\Delta R^{\perp}$ (beam spot diameter $2w$) evaluated at R_{max} are tabulated in Table 7.3. Where R_{max} was repetition rate limited, the transverse resolution at the hypothetical power limited range are given in parenthesis.

Summary choice of detector

The LiDAR parameters of all systems are tabulated in Table 7.3. The Newport detector excels with respects to range resolution ΔR in comparison with the other two detectors due to its 3 to 4 orders of magnitude shorter rise time t_{rise}. With respects to R_{max}, all detectors manage the 39 m repetiton rate limited R_{max} of the mode-locked-MOPA. None of the detector can detect signals from the 10 kHz repetition rate limited R_{max} at 15 km of the LD-MOPA, but the Newport detector provides the longest power limited R_{max}. With these MOPAs as transmitter lasers, the Newport detector is chosen.

It should be noted that the Thorlabs detector has ten times lower internal noise than the Newport detector. When calculations still do not predict longer R_{max} for the LiDAR systems with the Thorlabs than with the Newport detector, then it is due to both the LD-MOPA and mode-locked having shorter or much shorter pulse duration Δt than the rise time t_{rise} of the Thorlabs detector, but not the Newport detector. When $\Delta t << t_{rise}$, the $\sqrt{\frac{\Delta t}{\Delta t + t_{rise}}}$ factor (or $\left(\frac{\Delta t}{\Delta t + t_{rise}}\right)^{\frac{1}{4}}$ factor) proportional to R_{max} (Equation 2.57) approaches zero. Transmitter lasers emitting pulses comparable to or longer in pulse duration than the Thorlabs rise time of 23 ns, the Thorlabs detector will provide longer maximal ranges R_{max} than the Newport detector due to its lower internal noise.

7.2.3 Focusing the telescope output on the detector

As the Newport detector of choice is a fiber-coupled detector, the outputted collimated beam of the telescope was focused with a Thorlabs lens of 25 mm focal length into a fiber held in place and aimed at the lens by a fiber holder (FH). The fiber then leads via a 10/90 tap coupler to the detector. This was illustrated in Figure 7.3. For completeness, the alignment process is described here.

Initial alignments of the telescope, lens and the inlet of the fiber (held by the FH) were done in a semidark room. The telescope was first aimed at a piece of white paper which was hung a few meters from the telescope and illuminated by a lamp. Then the lens and fiber FH inlet were aligned along the axis of the telescope, by visually inspecting the image of the white paper on the FH inlet.

High precision alignment was achieved after turning on the transmitter laser. Without moving the receiver optics, the illuminated paper was replaced by a mirror, which the collimator was aimed at. The Collimator could be properly aimed at the mirror by tracing the beam spot of the transmitted signal from collimator to the mirror and back to the telescope with a detector card. (Detector cards change colour with temperature.) Mounted on a 3-axis stage (Thorlabs MAX313D(/M)), the FH position could further be finely adjusted (in three independent directions) until the received signal at the detector monitored by an oscilloscope was maximized.

7.3 Keeping track of return time - Coupling the transmitter and the receiver

Having settled on a transmitter and receiver design, this section describes the engineered method for communication between the two.

The range R is measured from the zero-range line ($R = 0$) of the system defined to be at the entrance to the telescope as seen in Figure 7.5. To find R, the transmitter must communicate to the receiver that a pulse was transmitted, and the receiver must be able to compare this information to the return time. This can be achieved by splitting the MOPA-outputted signal in the transmitter before the collimator using a 3/97 tap coupler. 97% of the signal (ranging pulse) is guided on through a fiber and transmitted through the collimator aimed at the target. The remaining 3 % of the signal (starting pulse) is guided in a fiber through the 10 % port of a 10/90 tap coupler at the receiver. It is then led on to the fiber-coupled detector, where it is detected at time t_0, indicating that a pulse has been transmitted. At time t_1 the ranging pulse will have returned form the target, propagated through the receiver optics, through the 90 % port of the 10/90 tap coupler, and is detected at the detector. The time between detection of starting and ranging pulses is the delay time $t_1 - t_0$

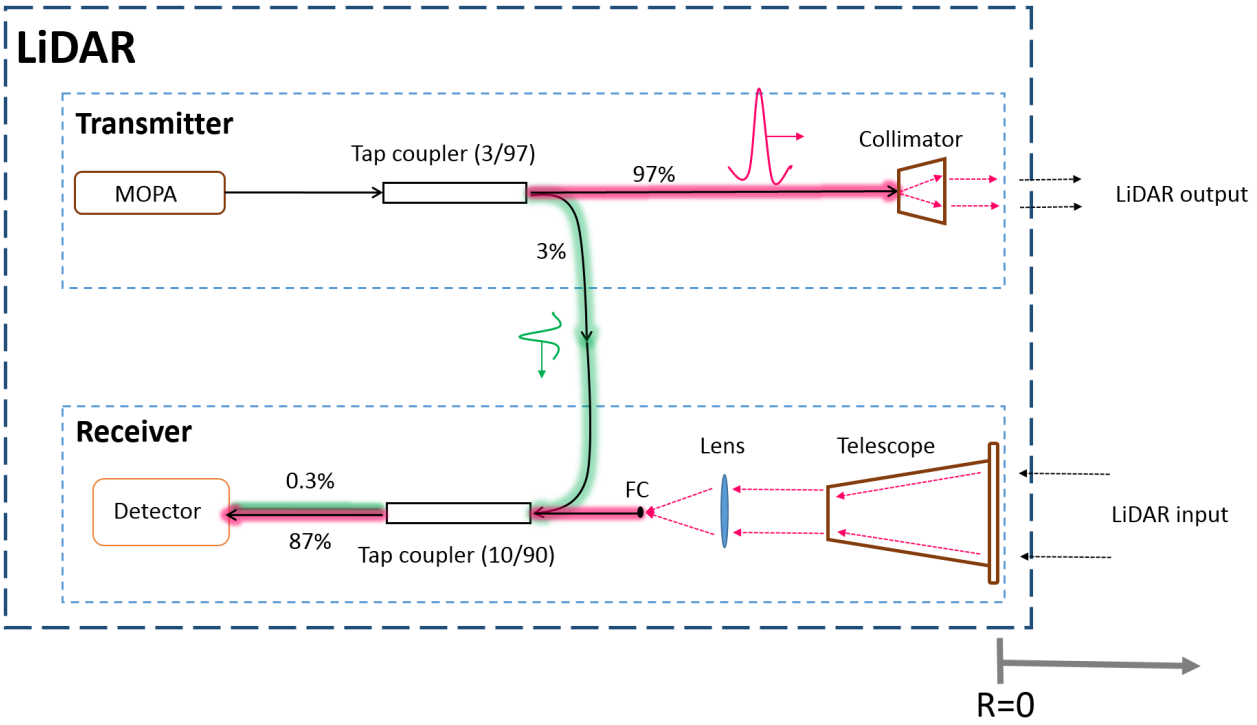

Figure 7.5: The MOPA signal power to be transmitter is split in 3% and 97% as indicated at a 3/97 tap coupler. After splitting, ranging pulse which travels to the target and back, travels the red optical path inside the LiDAR, and a starting pulse travels the green optical path inside the LiDAR. Full drawn lines indicate fiber, and dotted lines indicate free space propagation. The telescope entrance marks the zero range line where $R = 0$.

In Figure 7.5 the optical paths the starting pulse (green path) and ranging pulse (red path) propagate within the LiDAR system after the 3/97 tap coupler are indicated. A difference in path will correspond to a constant time offset t_{offset}. Thus, the actual return time t_{ret} of the pulse used for finding the range R in Equation 2.38 will be

$$t_{ret} = t_1 - t_0 - t_{offset}. \tag{7.1}$$

t_{offset} is a constant system parameter which must be determined once by finding the delay time $t_1 - t_0$ when the range R to a target and hence t_{ret} is known.

A similar method for keeping track of time was used in [81].

7.4 Outlook and End note

This chapter modelled the behaviour of LiDAR setups under clear weather conditions, with a perfect reflecting mirror target. The calculations showed the that the Newport detector was the detector of choice.

Although the mode-locked-MOPA outperforms the LD-MOPA in peak power, the LD-MOPA still allows ranging at longer distances due to its lower repetition rate. The range resolution of the LiDAR system with the Newport detector is better in combination with the mode-locked-MOPA than the LD-MOPA, as the first MOPA emits pulses of significantly shorter pulse duration than the latter.

As the mode-locked-MOPA is available, the LiDAR system was built with the mode-locked-MOPA as outlined in Figure 3.3. The results and discussion of initial testing with the LiDAR system are outlined in the following chapter 8.

Chapter 8

Testing the range finding LiDAR

The mode-locked-MOPA demonstrated in chapter 6 was integrated as the laser source in a range finding LiDAR setup built as described in chapter 7 and depicted in Figure 3.3.

This chapter provides the experimental method, results and discussion on the proof of principle range finding experiment using this LiDAR system.

8.1 Experimental Method and Results

Three experiments were carried out to measure the LiDAR offset time t_{offset}, maximal range R_{max} and range resolution ΔR. The internal technology/logistic/work wise of the LiDAR is summarized in section 7.3. The mode-locked-MOPA is operated as as described in chapter 6. Finally the output of the LiDAR Newport detector of choice is monitored by either an oscilloscope of 1.5 GHZ BW or an oscilloscope of 50 GHz BW.

This section includes the experimental method and results of the three experiments.

8.1.1 Experiment 1: Determining the LiDAR system offset time t_{offset}

In an initial test, the target was a mirror of 5 cm diameter, placed at a range R = 179.5 cm from the LiDAR. The distance corresponds (Equation 2.38) to a pulse return time t_{ret} of 11.97 ns. The LiDAR starting pulse and return ranging pulse were detected by the Newport detector at time t_0 and t_1 as explained in section 7.3. The 1.5 GHz BW oscilloscope output is plotted in Figure 8.2a.

The delay time $t_1 - t_0$ between ranging- and starting pulse was found to be 17.60 ns. Thus, the offset time t_{offset} as defined in Equation 7.1, due to unequal optical path traveled by the starting and ranging pulses, is 5.63 ns. t_{offset} is a system parameter which should be subtracted from all recorded delay times to obtain the return time t_{ret} used to determine the true range R via Equation 2.38.

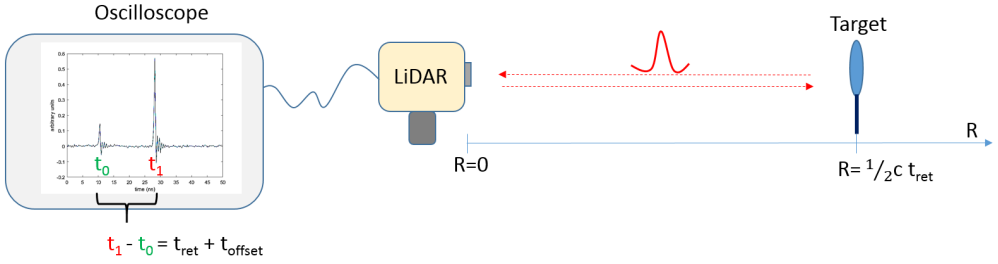

Figure 8.1: A target is fixed at position $\frac{1}{2}ct_{\text{ret}}$. At time t_0 the starting pulse is detected by the detector. t_{ret} is the return time of the ranging pulse (red) detected at the detector at time t_1. The delay time $t_1 - t_0$ is monitored on the oscilloscope. The offset time t_{offset} due to different optical path lengths of the starting and ranging pulse within the LiDAR.

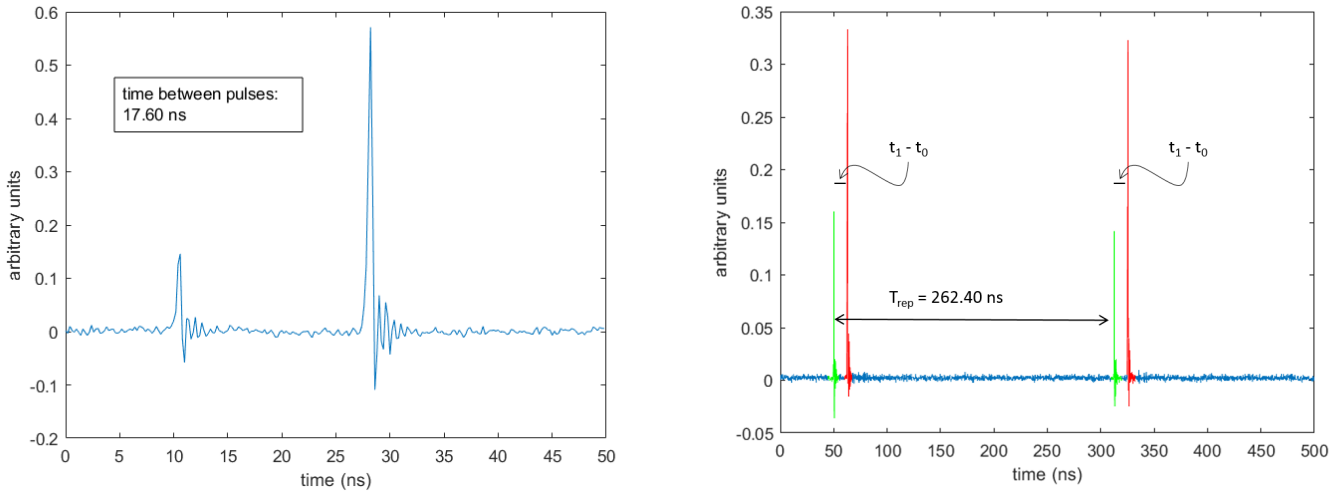

(a) **(b)**

Figure 8.2: (a) The ranging pulse (right) is delayed against the starting pulse (left) by $t_1 - t_0 = 17.60$ ns. (b) Two consecutive sets of starting (green colour) and ranging (red colour) pulses. The period between two pulse sets is $T_{rep} = 262.40$ ns.

8.1.2 Experiment 2: LiDAR maximal range R_{max}

The experimental setup is the same as in Figure 8.1. At any range the time scale at the oscilloscope can be set to view two successive pairs of starting and ranging pulses. Figure 8.2b shows that the monitored time between two starting pulses was T_{rep} is 262.40 ns. T_{rep} corresponds (using Equation 2.30) to the repetition rate 3.81 MHz of the mode-locked-MOPA.

Thus, the maximal range R_{max} is repetition rate limited to 39 m. Increasing the distance between the target and the LiDAR beyond 39 m would introduce an ambiguity of a multiple of 39 m in the true range.

8.1.3 Experiment 3: Finding LiDAR range resolution ΔR

A third experiment was carried out in order to measure the true range resolution ΔR of the LiDAR. The setup is depicted in Figure 8.3. For this experiment an available oscilloscope offering BW of 50 GHz, corresponding to a sampling time of 7 ps according to Equation 2.47 was used to monitor the delay time $t_1 - t_0$. The mirror from the first experiment was mounted on a movable sliding platform. The platform is placed at an arbitrary point $R_{z=0}$ on the R axis. From $R_{z=0}$, the platform can move along the R axis from $z = 0$ mm to $z = 20$ mm as illustrated in Figure 8.3.

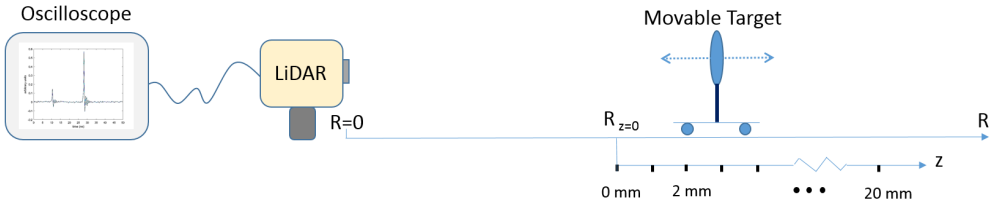

Figure 8.3: The target (a mirror) is mounted on a movable platform. The platform can move along the R axis from $R_{z=0}$ at incremnetns of 1 mm.

The mirror was moved along the z axis from $z = 0$ mm to $z = 20$ mm at increments of 1 mm. The monitored delay

time $t_1 - t_0$ at every position z, and is plotted against z in Figure 8.4. In the plot the delay time $t_1 - t_0$ is scaled to zero at $R_{z=0}$. The data points (blue) were fitted by a linear curve assumed to have slope $\frac{1}{1/2\ c}$ according to Equation 2.49. The standard deviation of the data points from the fitted curve was found to be 40 ps. In measured range, 40 ps corresponds to 6.1 mm via Equation 2.49. $\Delta R = 6.1$ mm is thus the range resolution this LiDAR system.

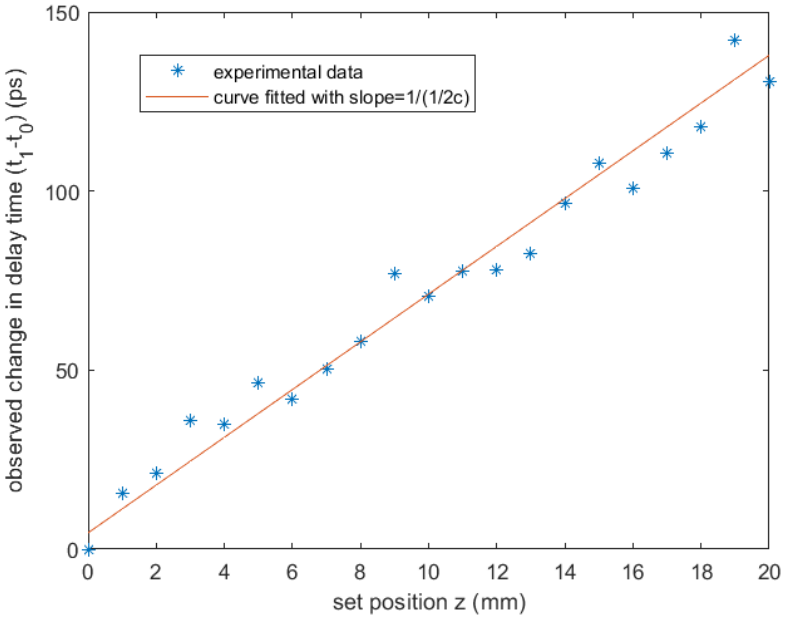

Figure 8.4: The horizontal axis shows the relative displacement of the target. The vertical axis shows the relative delay time. The linear curve is fitted with slope = $\frac{1}{\frac{1}{2}c}$. Standard deviation from the fitted curve is 40 ps, corresponding to $\Delta R = 6.1$ mm.

8.2 Discussion and Outlook

A proof of principle experiment on range finding was demonstrated with the LiDAR setup where the laser source was the all-fiber all-diode-pumped mode-locked-MOPA.

Here follows a discussion on the LiDAR parameters maximal range R_{max} and range resolution ΔR from the point of view of the laser source. Both the demonstrated mode-locked-MOPA, as well as the LD-MOPA are considered. Finally, the possibility of converting the range finding LiDAR into a DIAL is presented.

8.2.1 Maximal range: repetition rate limitations and power scaling

The maximal range R_{max} of the demonstrated LiDAR setup is limited to 39 m by repetition rate of the mode-locked-MOPA laser source. Calculation showed that purely in terms of the mode-locked-MOPA power, the maximal range could have been 4.5 km as tabulated in Table 7.3. To range at longer distances than 39 m, lower repetition rates than the 3.81 MHz are needed. By installing a pulse picker such as an acousto-optic modulator in the transmitter, pulses would only periodically be transmitted, effectively lowering the repetition rate [82]. Directly lowering the repetition rate of a mode-locked laser is also possible in a certain range, by increasing the cavity length as seen in Equation 2.37.The record low repetition rate of 77 kHz was reported in an Ytterbium-doped fiber laser with 3.8 km long cavity [83].

The other laser transmitter, the LD-MOPA, can electronically vary repetition rate between 10-100 kHz. At 10 kHz it

has a repetition rate limited maximal range at 15 km (f_{rep} = 10 kHz), but was limited by power to 1.6 km according to calculations presented in subsection 7.2.2. To range up to 15 km, further amplification would be required. Plans for a 2nd stage Holmium-doped fiber power amplifier, as well as results from a time dependent numerical model of this amplifier are outlined in appendixA. With the LD-MOPA as input, 1 MW peak powers were estimated. Carrying out similar calculations to those made in subsection 7.2.2, such power levels are sufficient to range above 15 km with either the Newport or Thorlabs detector.

8.2.2 Range resolution ΔR and Pulse width Δt

The demonstrated LiDAR showed a ranges resolution ΔR of 6.1 mm. Considering the laser pulse width, detector rise time, and also the oscilloscope sampling time, the LiDAR system has an effective response time (3.5 ps + 28 ps + 7 ps) of 38.5 ps. Modifying Equation 2.49 with the oscilloscope sampling time, the resulting range resolution is then 5.8 mm, which corresponds well with the measured resolution.

For a picosescond pulse duration, resolution is limited on the detector side. Exchanging the mode-locked-MOPA with the LD-MOPA the LiDAR would be limited in range resolution to 15 cm by the of 1 ns LD-MOPA pulse duration. The requirement on ΔR depends on the LiDAR application.

Millimeter range resolution could also be achieved beyond the mode-locked laser repetition rate limited ranges by shortening LD-MOPA pulse duration. A paper [28] first reported on shortening of pulses at 1550 nm from 100 ns to 3.5 ns duration under two-stage amplification from 4 mW to 9.5 W average power in LD-pumped erbium-doped fiber amplifiers. The pulse shortening was attributed to the time dependent gain discussed in subsection 2.3.5, and is expected when when the pulse duration exceeds the saturation energy of Equation 2.26. The 2nd stage amplifier proposed in subsection 8.2.1 for boosting the power of the LD-MOPA also predicts pulse shortening from 1 ns to 200 ps improving the LD-MOPA resolution resolution to 3.5 cm.

8.2.3 Further work: DIAL (Differential Absorption LiDAR)

Characterization of the master oscillator LD presented in subsection 4.1.2 revealed the possibility to easily tune its wavelength by electronically varying LD temperature. This looks promising for a differential absorption LiDAR (DIAL). A DIAL transmits pulses into the air in a direction free of solid objects, and detects the backscattered signal from the atmosphere. A DIAL operates at two wavelengths λ_{on} and λ_{off}. λ_{on} must coincide with an absorption line of the gas to be traced, whereas the atmosphere should generally be transparent to λ_{off}. By comparing the power of the return signals at the respective wavelengths, the gas concentration can be found. Hence the name, differential absorption LiDAR.

A paper [14] found the atmospheric absorption lines specifically around 2.05 μm interesting for a CO_2 sensing DIAL. Today, DIALs for gas sensing generally use two different laser sources for λ_{on} and λ_{off} [55]. Initial work showing how the LD-MOPA is tunable around the CO_2 absorption lines at 2.05 μm, and could be used as the laser source for both λ_{on} and λ_{off} in a CO_2 monitoring DIAL has already been done, and is included in appendix B.

Thus, the tunable LD boosted in power by fiber amplifiers looks promising for a variety of LiDAR applications.

Chapter 9

Conclusion

This thesis aimed at developing a light-weight, compact, laser system with all-diode holmium-doped all-fiber design, and to show its potential of being a laser source for a LiDAR operating within the promising atmospheric window between 2 - 2.5 μm [7]. Four goals were set to achieve this aim, and the following has been done:

First, a gain-switched DM semiconductor LD was characterized, and proved to be tunable in wavelength λ_s between 2051 and 2053 nm with a linewidth $\Delta\lambda < 0.05$ nm. The LD was driven at repetition rates f_{rep} between 10 kHz and 100 kHz. The LD produced pulses of duration Δt down to 1 ns with peak power P_{peak} assumed to be 6 mW.

Secondly, an all-PM single-mode holmium-doped fiber amplifier, pumped by two identical semiconductor CW FBG LDs emitting 300 mW at 1150 nm was built, and a complementary numerical model describing the behavior of the amplifier was developed. The power amplifier is in itself a novel device capable of amplifying optical signals in a broad optical spectrum of 2 - 2.1 μm, and has received its own packaging. The development resulted in a conference paper [73].

Thirdly, the amplifier was successfully demonstrated when integrated in a mode-locked-MOPA configuration, where the master oscillator was a mode-locked holmium-doped fiber laser emitting pulses of picosecond duration at a repetition rate f_{rep} of 3.81 MHz, with a spectral linewidth $\Delta\lambda$ of 1.6 nm centered at 2089 nm wavelength λ_s. The amplifier operated with a slope efficiency η_s of 10 %. The highest optical-to-optical efficiency η of 5.3 % was achieved at full amplification, where the the mode-locked-MOPA emitted 33 mW average power (18 dB gain), the pulse spectrum had broadened to a 6.6 nm linewidth $\Delta\lambda$, and each pulse split into a group of pulses of < 10 ps group duration. At medium amplification, the mode-locked-MOPA outputted 8 mW average power (12 dB gain) by emitting single pulses of 3.2 ps pulse duration Δt, at $\lambda_s = 2088.8$ nm with a linewidth $\Delta\lambda$ of 1.41 nm.

The parameters of the amplifier numerical model were calibrated using experimental data. Although some technical problems with the LD, which prevented a demonstration of the LD-MOPA, were encountered, the output of the LD-MOPA could be estimated using the the improved numerical model of the power amplifier. Amplification of peak power P_{peak} up to 0.8 W, corresponding to a gain of 21 dB, is expected independently of the possible LD repetition rates f_{rep}.

Fourth and finally, to show the potential of the demonstrated mode-locked-MOPA as a laser source for LiDAR applications, a setup was designed and built to carry out a proof of principle range-finding experiment. The designing and implementation of the LiDAR setup was carefully described. The mode-locked-MOPA based LiDAR setup could successfully measure distance to a reflective target. The range resolution ΔR of this LiDAR system was 6.1 mm. The maximal range R_{max} was 39 m due to the 3.81 MHz repetition rate f_{rep} of the mode-locked-MOPA. Range-finding LiDAR parameters were also estimated with the LD-MOPA as laser source, in the case of a reflective target, and when neglecting scattering. LD-MOPA peak power of 0.8 W and 1 ns pulse duration Δt are expected to allow range-finding up to a power limited maximal range R_{max} at 1.6 km, with a 15 cm range resolution ΔR. However, the LD repetition rate f_{rep} at 10 kHz would allow ranging up to a 15 km distance, could the power be scaled sufficiently.

There are several interesting extensions to this work. First, a natural next step would be to implement the LD-MOPA in the LiDAR setup. Secondly, scaling LD-MOPA output power necessary to range up to the 10 kHz LD-MOPA repetition rate limited R_{max} of 15 km, can be done by implementing a 2$^{\text{nd}}$ stage power amplifier. A time dependent numerical model of a 2$^{\text{nd}}$ amplifier has already been developed, and is outlined in appendix A. The 2$^{\text{nd}}$ stage numerical model also predicts pulse shortening, similar to that observed in [28], from 1 ns down to 200 ps duration from the LD-MOPA input. This would improve the LD-MOPA based LiDAR resolution to 3.5 cm. Thirdly, the tunability of LD laser wavelength coincides with the CO_2 absorption lines around 2.05 μm [14]. As argued in appendix B, the LD could be implemented as the single laser source of a CO_2 sensing DIAL.

Appendix A

2nd stage holmium-doped power amplifier

The development of a 2nd stage holmium-doped power amplifier has two origins of motivation. Firs, additional peak power is needed to achieve the LD-MOPA repetition rate limited maximal range of 15 km. Secondly, pulse shortening from nanosecond to picosecond duration under amplification, similar to that reported on in [28], would improve the range resolution of the LD-MOPA based LiDAR.

This appendix includes first the proposed setup of the 2nd stage power amplifier, then simulations of the pulsed signal from the LD-MOPA in the software *RP Fiber Power V5.0*, as well as the reasons for the amplifier design. Finally the main results from modelled behaviour of the 2nd stage amplifier with the LD-MOPA as input are presented.

A.1 Setup of the 2nd stage Power Amplifier

The planned setup of a 2nd stage holmium-doped fiber power amplifier is shown in Figure A.1.

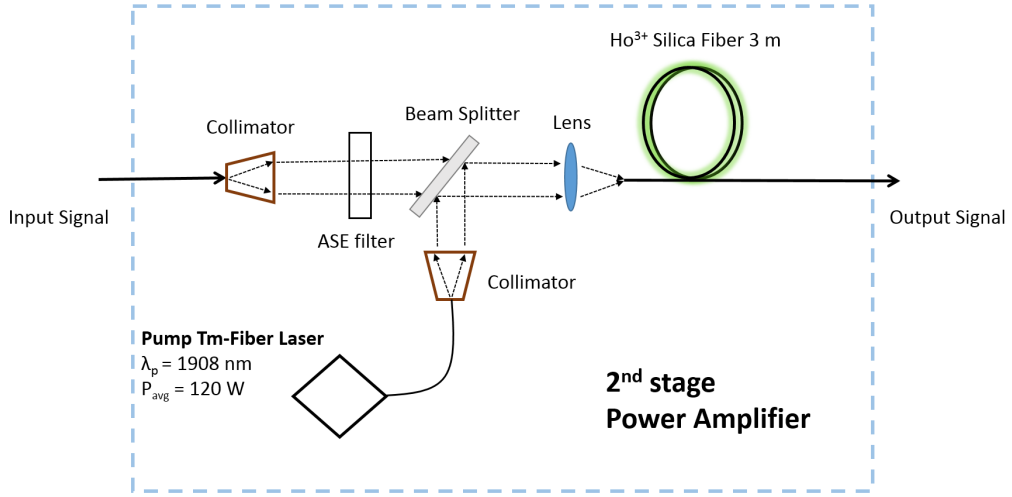

Figure A.1: Setup of the 2nd stage Power Amplifier, where the rhombus represents the Thulium-doped fiber laser. The collimators, beam splitter, ASE filer and lens are marked. Optical fibers are drawn as bold lines. The holmium-doped active fiber is coloured green to distinguish it from the passive fiber. Free space beams are drawn in stippled lines.

A CW thulium-doped fiber laser emitting up to 120 W average power at 1908 nm is the pump laser source. The laser output is collimated to a free space at a collimator, and is coupled to the active fiber via a beam splitter and focused into the fiber with a lens.

The input signal is collimated from the fiber to free space. An ASE filter filters out ASE. The Signal meets the pump power at the beam splitter and is focused into the active fiber via the previous mentioned lens.

The active fiber is a 3 m long Ho^{3+} doped large mode area (LMA) fiber (iXblue IXF-HDF-PM-20-250-0.08). The fiber has core diameter d_{core} of 20 μm and cladding diameter d_{clad} of 250 μm.

The amplifier output is also the output of the two-stage-amplified MOPA.

A.2 Designing the 2nd stage Power Amplifier

The 2nd stage amplifier was designed to maximize amplification of the LD-MOPA with output characteristics summarized in Table A.1.

	λ_s nm	P_{peak} W	Δt ns	f_{rep} kHz
LD-MOPA	2051-2053	0.8	1	10-100

Table A.1: LD-MOPA signal parameter. The λ_s is tunable , peak power P_{peak}, pulse duration Δt and repetition rate f_{rep} are given.

A pulsed model was developed for the 2nd stage power amplifier using the software *RP Fiber Power V5.0* described in section 5.1. Further discussion is based on section 5.1. Functionality of the *RP Fiber Power V5.0* allows the user to first solve the steady-state coupled (Equation 2.15)=0 and Equation 2.20 iteratively through the length of the fiber for the case that the input signal intensity is zero. Then a pulse is introduced as a time-dependent perturbation to the steady-state solution.

Simulations of the LD-MOPA output showed that the ASE power level exceeded the signal as seen in Figure 5.2a. To avoid the amplification of ASE in the 2nd stage amplifier, an ASE filter was planned before the input to the 2nd stage power amplifier. This was modelled by zeroing the power input of the ASE channels of the 2nd stage amplifier.

In order to stay below the fiber damage intensity threshold of 5 kW μm^{-2} [84], a large mode area (LMA) fiber from iXblue (IXF-HDF-PM-20-250-0.08) was considered as the active fiber in the 2nd stage power amplifier. LMA fibers have larger core diameter d_{core} (and consequently larger core areas) than other fibers [85]. Peak powers of < 1.6 MW are possible without going above the damage intensity threshold.

As only the core absorption in dB/m in the iXblue fiber at 1150 nm wavelength was given by the producer, the doping concentration N_{Ho} was estimated by simulating absorption in a steady-state regime, and fitting the curve with the doping concentration. The parameters of the iXblue fiber are given in Table A.2.

	Core absorption at 1150 nm dBm^{-1}	Estimated N_{Ho} 10^{25} m^{-3}	d_{core} μm
iXblue	24	5.8	20

Table A.2: Doping concentration N_{Ho} is estimated from the core absorption announced by the producers of the iXblue LMA fiber. Core diameter d_{core} is also given.

Due to computation time, the choice of fiber length was done by adopting a steady-state approximation of the 2nd amplifier, and considering an input signal at 2051 nm of 80 μW average power (corresponding to running the LD-MOPA at f_{rep} = 100 kHz). The fiber length was decided on to be 3 m, after similar process to the one explained in section 5.2.

A.3 Results and Discussion

A time-dependent numerical model of the planned power amplifier depicted in Figure A.1 was adopted. Taking the LD-MOPA output of 0.8 W peak power, 1 ns pulse duration at first 10 kHz and then 100 kHz repetition rate as input to the numerical model, Figure A.2 shows simulated peak power, Figure A.3a simulated pulse duration, and Figure A.3b simulated pulse energy when applying up to 100 W pump power at 1908 nm. Results from the LD-MOPA signal at 10 kHz repetition rate are marked red, and at 100 kHz are marked blue.

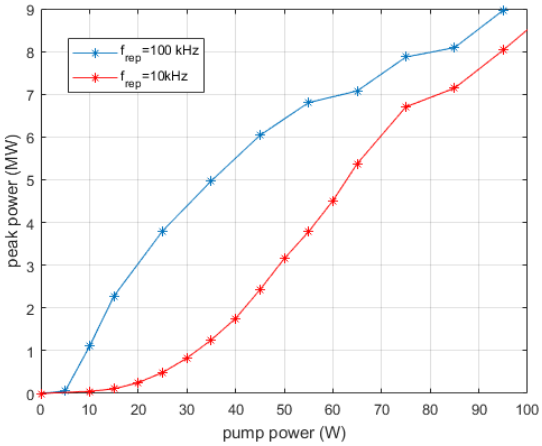

Figure A.2: Simulated output peak power P_{peak} from the 2nd stage power amplifier with an input signal at λ_s = 2051 nm, Δt = 1 ns, P_{peak} = 0.8 W at $f_{rep=10\,\text{kHz}}$ (red) and $f_{rep=100\,\text{kHz}}$ (blue) while varying the applied pump average power up to 100 W.

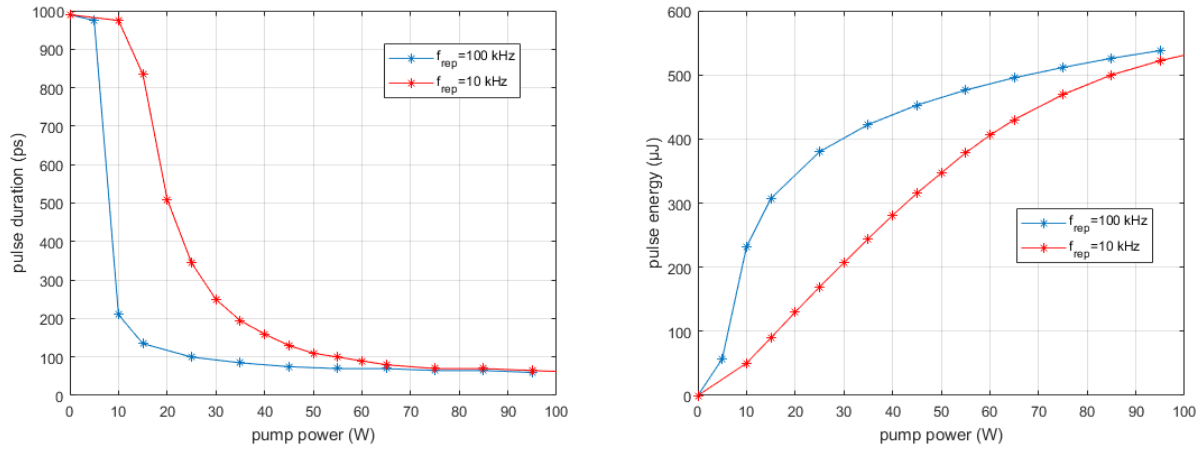

(a) **(b)**

Figure A.3: (a) Simulated output pulse duration and (b) pulse energy from the 2nd stage power amplifier with an input signal at λ_s = 2051 nm, Δt = 1 ns, P_{peak} = 0.8 W at $f_{rep=10\,\text{kHz}}$ (red) and $f_{rep=100\,\text{kHz}}$ (blue) while varying the applied pump average power up to 100 W.

1 MW peak power is expected at respectively 10 W and 30 W applied 2nd stage pump power at a pulse repetition rate of 100 kHz and 10 kHz. Amplification to higher peak powers would require a fiber with larger core area in order not to exceed the damage intensity threshold.

Below the damage threshold, pulse shortening down to around 200 ps and pulse energies of 250 μJ at around 10 W

and 35 W applied stage pump power for signals at respectively 10 kHz and 100 kHz repetition rate are expected.

According to Equation 2.26 the fiber saturation energy is proportional to the mode area. Approximating the mode area to the fiber core area, the saturation energy is 81 μJ. Figure A.3b shows that the signal at 100 kHz repetition rate has reached the 81 μJ saturation energy at between 5-10 W applied pump power. Thus, it is clear that a steady-state model would not have been valid for this amplifier. Also, at between 5-10 W applied pump power, Figure A.3a shows the onset of pulse shortening for the 100 kHz repetition rate signal. Thus, the model shows pulse compression when the saturation energy is reached.

Although amplification beyond the damage threshold is not realistic, the saturating behavior of pulse energy with added pump power in Figure A.3b shows stability in the numerical model.

A.4 Conclusion

Work was done towards planning and modelling a 2$^{\text{nd}}$ stage holmium-doped power amplifier. Assuming the output of the LD-MOPA system modelled in chapter 5 at 2051 nm of 0.8 W peak power, 1 ns pulse duration at first 10 kHz and then 100 kHz repetition rate, the numerical model predicts peak power of 1 MW, pulse shortening from 1 ns to 200 ps, as well as pulse energies of the 250 μJ, while staying below the fiber damage intensity threshold. For higher peak powers, a LMA fiber with larger core area would be necessary.

Thus, the two-stage LD-MOPA has a number of advantages. The LD offers electronic tunability of repetition rate f_{rep} between 10 and 100 kHz and wavelength λ_s between 2051 and 2053 nm. The two-stage fiber amplifiers reducing pulse duration Δt from 1 ns to 200 ps, and increasing peak power P_{peak} from 6 mW to 1 MW. As such, the two-stage-LD-MOPA could be applicable as the laser source for several LiDAR applications.

Appendix B

CO_2 Differential Absorption LiDAR (DIAL) at 2.05 μm

Characterization of the MOPA laser components presented in section 4.1 showed that the master oscillator LD wavelength λ_s could easily be tuned between 2051 and 2053 nm, and that the emission had a linewidth $\Delta\lambda$ of 0.05 nm. With such properties, the LD emission could potentially fit in and around CO_2 absorption lines around 2.05 μm[14], making the LD a promising laser source in a CO_2 monitoring DIAL.

This appendix starts out by outlining relevant background theory on DIAL, before it goes on to discuss the viability of the LD as a laser source in a CO_2 DIAL.

B.1 Background theory on DIAL

This section supplements the background theory on remote sensing presented in section 2.6. A backscattering LiDAR equation and a DIAL equation shows how the information on gas concentration is extracted from backscattered LiDAR signals.

B.1.1 Remote sensing of the atmosphere

In the range finding TOF method discussed in section 2.6 the range R to a solid target was measured by keeping track of the return time of a pulse. However, the target may just as well be the segment of the atmosphere covered by the pulse at range R [5, p. 7]. The size of this segment is determined by the LiDAR resolution discussed in section 2.6.3, and corresponds to how well the gas concentration profile $N_a(R)$ is resolved.

The power scattered back to the LiDAR from a the atmospheric segment covered by the pulse at range R [54, p. 15] can be modeled by adjusting the reflecting target LiDAR Equation 2.40 by letting,

$$\frac{\rho}{\Omega_T} \rightarrow \Delta R \beta(R,\lambda) \, . \tag{B.1}$$

$\frac{\rho}{\Omega_T}$ may be interpreted as the fraction ρ of incident power on the solid target which is reflected and spreads across the target solid angle Ω_T. $\beta(R,\lambda)$ is the fraction of power per segment ΔR scattered back to the LiDAR from range R, and is given by [5, p. 9]

$$\beta(R,\lambda) = \sum_s N_s(R) \frac{\mathrm{d}\sigma_s(\lambda)}{\mathrm{d}\Omega}|_\pi \, . \tag{B.2}$$

Scattering is caused by gas molecules and particles in the atmosphere and depends as described in subsection 2.6.4.

Finally, the target area A_T of Equation 2.43 would always be the beam spot area at range R of $\pi(R\theta_t)^2$ in atmospheric sensing. Transforming Equation 2.40 by altering $\frac{\rho}{\Omega_T}$, A_T and A_r accordingly, the backscattering LiDAR equation takes the form [86]

$$P_r(R,\lambda) = P_t \;\; \Delta R \;\; \beta(R,\lambda) \, \frac{A_r}{R^2} \;\; \mathscr{T}(R,\lambda) \;\; O(R) \;\; \eta_{sys} \, , \tag{B.3}$$

where, the receiver area A_r was given by Equation 2.45 it can be remebered that P_t was transmitted power given by Equation 2.48, D_r the reveiver aperture diameter, $\mathscr{T}$ the atmospheric transmittance given by Equation 2.60 and η_{sys} the LiDAR internal system efficiency. Finally, the overlap of the laser beam and the receiver FOV, the overlap

function $O(R)$ is accounted for. [5, p. 8]. In η_{sys}The terms $\mathscr{T}$ and β contain all the information on the atmosphere in the backscattering LiDAR Equation B.3 [5, p. 6].

Inserting $\mathscr{T}$ from Equation 2.60 into Equation B.3

$$P_r(R,\lambda) = \underbrace{P_t \ \frac{c\Delta t}{2} \ \frac{A_r}{R^2} \ O(R) \ \eta_{sys}}_{\text{LiDAR system dependent}} \ \underbrace{\beta(R,\lambda) \ \exp\Big(-2\int_0^R \sum_s N_s(x)\sigma_s(\lambda)\mathrm{d}x\Big)}_{\text{Scattering (Rayleigh or Mie)}} \ \underbrace{\exp\Big(-2\int_0^R \sum_a N_a(x)\sigma_a(\lambda)\mathrm{d}x\Big)}_{\text{Absorption (molecular)}}, \quad \text{(B.4)}$$

where it is summed over the contribution from all scatterers s and absorbers(gases) a, with respective atmospheric densities N_s and N_a and cross sections σ_s and σ_a [5, p. 10]. Equation B.4 can be factored in a system dependent, scattering dependent and absorption dependent factors. The task of a DIAL is extracting information of the concentration $N_a(R)$ of gas a at range R. $N_a(R)$ is obtained by inverting Equation B.4 as will be seen next.

B.1.2 The DIAL equation

The DIAL operates at two wavelengths λ_{on} (resonant) and λ_{off} (nonresonant). λ_{on} must coincide with an absorption line of the gas to be traced, whereas the atmosphere should generally be transparent to λ_{off} [9]. The DIAL extracts information on the density of gas x, $N_{a=x}(R)$ by comparing the return signal $P_r(R,\lambda_{on})$ at λ_{on} to the return signal $P_r(R,\lambda_{off})$ at λ_{off}, by evaluating

$$\frac{P_r(R,\lambda_{on})}{P_r(R,\lambda_{off})} \quad \text{(B.5)}$$

By choice of wavelengths, $P_r(R,\lambda_{off})$ is generally the stronger than $P_r(R,\lambda_{on})$, as the the signal at λ_{on} is absorbed by the gas to be traced. Equation B.5 can be furter evaluated and under the following assumptions [54, pp. 126-127]:

1. By properly designing the system, the system dependent factor of Equation B.4 can become identical at both λ_{on} and λ_{off}.

2. When λ_{on} and λ_{off} fulfill $|\frac{1}{\lambda_{on}} - \frac{1}{\lambda_{off}}| \leq 1\ \mathrm{cm}^{-1}$

$$\sigma_s(\lambda_{on}) \approx \sigma_s(\lambda_{off}) \ , \quad \text{(B.6)}$$

   for all scatterers s. The scattering factor of Equation B.4 at λ_{on} and λ_{off} is equal to approximation.

3. If there are no absorption lines from other absorbers (gases) around λ_{on} and λ_{off}, then

$$\sigma_{a\neq x}(\lambda_{on}) \ , \ \sigma_{a\neq x}(\lambda_{off}) \to 0 \ , \quad \text{(B.7)}$$

   and only absorption from gas $a = x$ is relevant.

Taking these three assumptions into account, Equation B.5 reduces to

$$\frac{P_r(R,\lambda_{on})}{P_r(R,\lambda_{off})} = \frac{\exp\Big(-2\int_0^R N_{a=x}(x)\sigma_{a=x}(\lambda_{on})\mathrm{d}x\Big)}{\exp\Big(-2\int_0^R N_{a=x}(x)\sigma_{a=x}(\lambda_{off})\mathrm{d}x\Big)} \quad \text{(B.8)}$$

where only attenuation due to absorption contributes to the ratio of returned power levels at the two wavelengths. The absorption cross sections $\sigma_{a=x}$ may be found in the literature for the specific gas. Pulling $\sigma_{a=x}(\lambda_{on})$ and $\sigma_{a=x}(\lambda_{off})$ out of the integrals of Equation B.8, taking the natural logarithm of each side, and differentiating with respects to range R, the gas concentration $N_{a=x}(R)$ of gas $a = x$ at range R is given by [54, p. 126]

$$N_{a=x}(R) \ = \ \frac{1}{2} \ \frac{1}{\sigma_{a=x}(\lambda_{on}) - \sigma_{a=x}(\lambda_{off})} \ \frac{\mathrm{d}}{\mathrm{d}R} \ \ln\frac{P_r(R,\lambda_{off})}{P_r(R,\lambda_{on})} \ . \quad \text{(B.9)}$$

Equation B.9 is referred to as the DIAL equation.

The received power P_r at either wavelength λ_{on} and λ_{off} will be a range dependent signal, as the transmitted pulse is partially backscattered on its way through the atmosphere as illustrated in Figure 2.13b. Processing the data according to Equation B.9, the gas concentration $N_{a=x}$ in the direction in which laser is shot, can be known from range $R = 0$ to the maximal range of the DIAL [55]. It can be noted that although scattering enables the gas tracing, since signal returns to the LiDAR due to scattering, scattering parameters are not needed in order to evaluate $N_{a=x}(R)$ as is seen from Equation B.9, when resonant and non resonant wavelengths are chosen wisely according to the listed requirements.

B.2 Discussion on potential λ_{on} and λ_{off}

Next, λ_{on} and λ_{off} are considered for a CO_2 monitoring DIAL where the LD is the laser source.

B.2.1 LD wavelength tunability

The tunability of the LD emission wavelength λ_s between 2051.1 and 2053.0 nm was shown in Figure 4.2b. The data points are coplotted with the spectral atmospheric transmittance in Figure B.1. The atmospheric absorption lines (regions where $\mathcal{T} \to 0$) in this range correspond to rotational/vibrational absorption lines of CO_2 [14]. λ_{on} = 2052.06 nm and λ_{off} = 2051.81 nm are potential choices of resonant and non resonant wavelengths. Specifically, they fulfill the second assumption Equation B.9 is based on. The spectra of the laser lines centered at these λ_{on} and λ_{off} were measured during the initial characterizations, and are coplotted with atmospheric transmittance in Figure B.2.

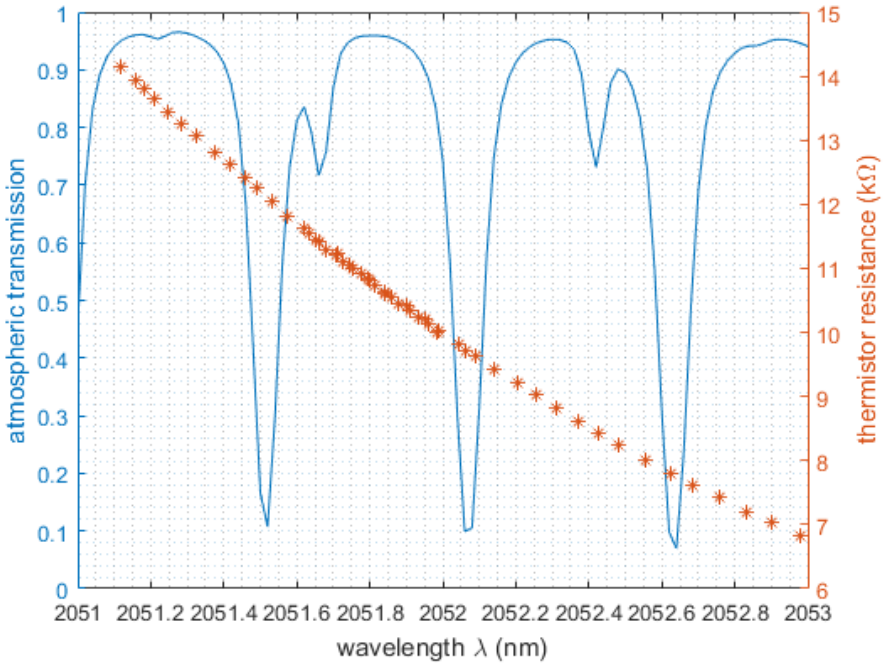

Figure B.1: Spectral atmospheric transmittance due to absorption (blue curves). Plotted with data from [15]. Tunability curve of the LD (orange dots) where the monitored thermistor resistance R_{therm} is plotted against LD emission of the signal wavelength λ_s.

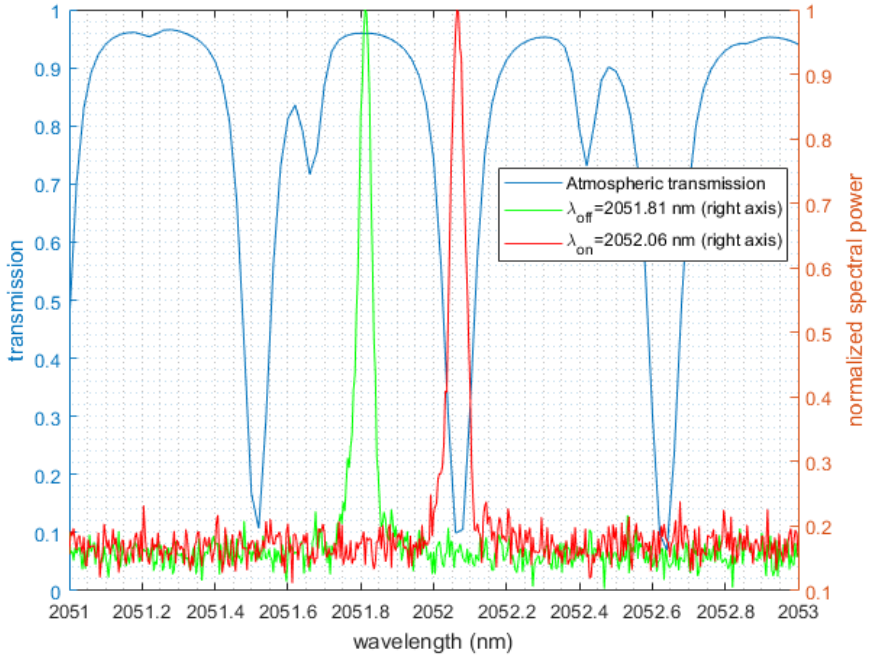

Figure B.2: Spectral atmospheric transmittance due to absorption (blue curves). Plotted with data from [15]. Coplotted are the measured spectral outputs of the LD-MOPA λ_{on} = 2052.06 nm (red curve) and λ_{off} = 2051.81 nm (green curve).

B.2.2 Uncertainty in the tunability

Although the DIAL equation Equation B.9 models the DIAL laser output as a single wavelength emission at $\lambda_s = \lambda_{on}$ or $\lambda_s = \lambda_{off}$, the LD laser output was found in subsection 4.1.2 to have an average linewidth $\Delta\lambda$ of 0.05 nm. It is of importance that especially λ_{on} is set with high precision to avoid error in the measured gas concentration found by Equation B.9 [9]. Since the laser linewidth at λ_{on} = 2052.06 nm is comparable to the absorption linewidth at 2052.07 of 0.015 nm estimated from Figure B.2, it is relevant to discuss the precision with which the laser wavelength λ_s may be tuned, and the uncertainty in the width of the laser linewidth $\Delta\lambda$ of 0.05 nm that was measured. It is advisable to first read section 4.1.

The current to the TEC could be adjusted to the closest 0.01 V in the monitored thermistor voltage V_{therm}, corresponding to a change of 0.1 kΩ in thermistor resistance R_{therm} according to Equation 4.1. According to Figure 4.2b a 0.1 kΩ change in R_{therm} corresponds to a change of 0.075 nm in λ at the most. Thus the laser wavelength λ_s can be set with a precision of 0.04 nm. However, wavelength λ could be measured to the nearest 0.05 nm, as this was the resolution of the optical spectrum analyzer used. Thus, it is believed that with an optical spectrum analyzer of higher resolution the laser wavelength λ_s could potentially be set with a precision < 0.05 nm.

On average, the linewidth LD in $\Delta\lambda$ characterization of the of the output was 0.056 nm , with a standard deviation of 0.0046 nm. The linewidth $\Delta\lambda$ is on the verge of the uncertainty 0.05 nm in the measurement of wavelength λ. Thus, the linewidth could be narrower than 0.05 nm.

Thus, once calibrated with a optical spectrum analyzer of higher resolution than 0.05 nm, the LD-MOPA laser wavelength λ_s set to λ_{on} = 2052.06 nm is believed to fit inside the absorption line at 2052.07 of 0.15 nm width.

B.3 Conclusion

The LD is tunable in wavelength across the CO_2 absorption lines around 2.05 μm. It is estimated that the LD laser wavelength λ_s can be set with a precision $\leq$ 0.05 nm. The laser linewidth is seen to be $\Delta\lambda \leq$ 0.05 nm. Thus, two possible λ_{on} = 2052.06 nm and λ_{off} = 2051.81 nm wavelengths achievable by the LD, are promising for a CO_2 DIAL.

Bibliography

[1] F. Riehle, "Optical atomic clocks for a future new definition of the second," in *2014 Conference on Lasers and Electro-Optics - Laser Science to Photonic Applications*, 2014, pp. 1–2.

[2] V. Serebryakov, E. V. Boiko, N. N. Petrishchev, and A. Yan, "Medical applications of mid-IR lasers. Problems and prospects," *Journal of Optical Technology*, vol. 77, no. 1, pp. 6–17, 2010.

[3] J. Hecht, "Lidar for Self-Driving Cars," *Optics & Photonics News*, vol. 29, no. 1, pp. 26–33, 2018.

[4] L. Joly, F. Marnas, F. Gibert, D. Bruneau, B. Grouiez, P. H. Flamant, G. Durry, N. Dumelie, B. Parvitte, and V. Zéninari, "Laser diode absorption spectroscopy for accurate CO_2 line parameters at 2 μm: consequences for space-based DIAL measurements and potential biases," *Applied Optics*, vol. 48, no. 29, pp. 5475–5483, 2009.

[5] U. Wandinger, "Introduction to lidar," in *Lidar: Range-Resolved Optical Remote Sensing of the Atmosphere*, C. Weitkamp, Ed. Springer, 2005, vol. 1, pp. 1–18.

[6] M.-C. Amann, T. M. Bosch, M. Lescure, R. A. Myllylae, and M. Rioux, "Laser ranging: a critical review of unusual techniques for distance measurement," *Optical Engineering*, vol. 40, pp. 10–19, 2001.

[7] I. T. Sorokina, V. V. Dvoyrin, N. Tolstik, and E.Sorokin, "Mid-IR Ultrashort Pulsed Fiber-Based Lasers," *IEEE Journal of Selected Topics in Quantum Electronics*, vol. 20, no. 5, pp. 1–12, 2014.

[8] M. L. Salby, *Fundamentals of Atmospheric Physics*. 1996, Academic Press.

[9] W. Gong, C. Xiang, F. Mao, X. Ma, and A. Liang, "Wavelet modulus maxima method for on-line wavelength location of pulsed lidar in CO_2 differential absorption lidar detection," *Photonics Research*, vol. 4, no. 2, pp. 74–83, 2016.

[10] Figure from: "Electro-Optics", RF Cafe. [Online]. Available: http://www.rfcafe.com/references/electrical/ew-radar-handbook/electro-optics.htm. Accessed:2018-06-20].

[11] S. Mayor, and S. Spuler, "High pulse-energy, eye-safe lidar system," U.S. Patent 7 583 364, 2009.

[12] D. J. Richardson, J. Nilsson, and W. A. Clarkson, "High power fiber lasers: current status and future perspectives [invited]," *Journal of the Optical Society of America B*, vol. 27, no. 11, pp. 63–92, 2010.

[13] J. D. V. Hey, *A Novel Lidar Ceilometer: Design, Implementation and Characterisation*. Doctoral Thesis accepted by Loughborough University, UK. Published by Springer: 2015.

[14] S. Schilt, R. Matthey, K. H. Tow, L. Thévenaz, and T. Südmeyer, "All-fiber molecular frequency reference at 2 μm based on a versatile laser modulation sideband locking and a hollow-core fiber gas cell," in *2017 Conference on Lasers and Electro-Optics Europe European Quantum Electronics Conference*, 2017, pp. 1–1.

[15] S. D. Lord, "Nasa technical memorandum 103957," courtesy of Gemini Observatory, 1992. [Online]. Available: http://www.gemini.edu/sciops/telescopes-and-sites/observing-condition-constraints/ir-transmission-spectra. [Accessed:2017-12-17].

[16] Figure provided by I. T. Sorokina.

[17] R. M. Measures, *Laser Remote Sensing: Fundamentals and Applications*. John Wiley & Sons, 1984.

[18] M. U. Piracha, D. Nguyen, D. Mandridis, T. Yilmaz, I. Ozdur, S. Ozharar, and P. J. Delfyett, "Range resolved lidar for long distance ranging with sub-millimeter resolution," *Optics Express*, vol. 18, no. 7, pp. 7184–7189, 2010.

[19] R. Paschotta, "Rare-earth-doped fibers," *Encyclopedia of Laser Physics and Technology*, [Online]. Available:

https://www.rp-photonics.com/rare_earth_doped_fibers.html. [Accessed:2017-12-18].

[20] N. Massa, "Fiber optic telecommunication," in *Fundamentals of Photonics*, C. Roychoudhuri, Ed. SPIE, 2000, vol. 1, pp. 293–347.

[21] B. M. Walsh, "Review of Tm and Ho materials; spectroscopy and lasers," *Laser Physics*, vol. 19, no. 4, pp. 855–866, 2009.

[22] L. Li, B. Zhang, K. Yin, L. Yang, and J. Hou, "1 mJ nanosecond all-fiber thulium-doped fiber laser at 2.05 μm," *Optics Express*, vol. 23, no. 14, pp. 18 098–18 105, 2015.

[23] N. Simakov, Z. Li, Y. Jung, J. M. O. Daniel, P. Barua, P. C. Shardlow, S. Liang, J. K. Sahu, A. Hemming, W. A. Clarkson, S. Alam, and D. J. Richardson, "High gain holmium-doped fibre amplifiers," *Optics Express*, vol. 24, no. 13, pp. 13 946–13 956, 2016.

[24] D. Barat, A. Vicet, J. Angellier, Y. Rouillard, S. Guilet, L. L. Gratiet, A. Martinez, and A. Ramdane, "Antimonide-based dfb laser diodes in the 2-2.7 μm wavelength range," in *2007 European Conference on Lasers and Electro-Optics and the International Quantum Electronics Conference*, 2007, pp. 1–1.

[25] J. O'Carroll, D. Byrne, B. Kelly, R. Phelan, F. C. G. Gunning, P. M. Anandarajah, and L. P. Barry, "Dynamic characteristics of InGaAs/InP multiple quantum well discrete mode laser diodes emitting at 2 μm," *Electronics Letters*, vol. 50, no. 13, pp. 948–950, 2014.

[26] C. Herbert, D. Jones, A. Kaszubowska-Anandarajah, B. Kelly, M. Rensing, J. O'Carroll, R. Phelan, P. Anandarajah, P. Perry, L. Barry, and J. O'Gorman, "Discrete mode lasers for communication applications," *IET Optoelectronics*, vol. 3, no. 1, pp. 1–17, 2009.

[27] Thorlabs, "1940 nm Fabry-Perot Laser Butterfly Package," FPL1940S datasheet, 2011.

[28] V. V. Dvoyrin, D. Klimentov, J. O. Klepsvik, I. V. Mazaeva, and I. T. Sorokina, "Multi-kilowatt peak power nanosecond Er-doped fibre laser," *IEEE Photonics Technology Letters*, vol. 28, no. 23, pp. 2772–2775, 2016.

[29] O. Svelto, *Principles of Lasers*. Springer, 2010.

[30] R. Paschotta, "Lasers," *Encyclopedia of Laser Physics and Technology*, [Online]. Available: https://www.rp-photonics.com/lasers.html. [Accessed:2017-12-03].

[31] R. Paschotta, "Master oscillator power amplifier," *Encyclopedia of Laser Physics and Technology*, [Online]. Available: https://www.rp-photonics.com/master_oscillator_power_amplifier.html. [Accessed:2017-12-18].

[32] R. S. Quimby, *Photonics and Lasers: An Introduction*. John Wiley & Sons, 2006.

[33] J.-C. Diels and W. Rudolph, *Ultrashort Laser Pulse Phenomena: Fundamentals, Techniques, and Applications on a Femtosecond Time Scale*. Academic Press, 2006.

[34] R. Paschotta, "Bandwidth," *Encyclopedia of Laser Physics and Technology*, [Online]. Available: https://www.rp-photonics.com/fiber_bragg_gratings.html. [Accessed:2017-12-21].

[35] R. Paschotta, "Beam quality," *Encyclopedia of Laser Physics and Technology*, [Online]. Available: https://www.rp-photonics.com/beam_quality.html. [Accessed:2017-12-18].

[36] R. Paschotta, "Silica fibers," *Encyclopedia of Laser Physics and Technology*, [Online]. Available: https://www.rp-photonics.com/silica_fibers.html. [Accessed:2017-12-18].

[37] M.-A. Lapointe, S. Chatigny, M. Piché, M. Cain-Skaff, and J.-N. Maran, "Thermal effects in high-power CW fiber lasers," *Proceedings of SPIE - The International Society for Optical Engineering*, vol. 7195, pp. 46–57, 2009.

[38] G. Keiser, F. Xiong, Y. Cui, and P. P. Shum, "Review of diverse optical fibers used in biomedical research and clinical practice," *Journal of Biomedical Optics*, vol. 19, no. 8, pp. 19–29, 2014.

[39] R. Paschotta, "V number," *Encyclopedia of Laser Physics and Technology*, [Online]. Available: https://www.rp-photonics.com/v_number.html. [Accessed:2018-06-08].

[40] R. Paschotta, "Numerical aperture," *Encyclopedia of Laser Physics and Technology*, [Online]. Available: https://www.rp-photonics.com/numerical_aperture.html. [Accessed:2018-06-08].

[41] R. Paschotta, "Polarization-maintaining fibers," *Encyclopedia of Laser Physics and Technology*, [Online]. Available: https://www.rp-photonics.com/polarization_maintaining_fibers.html. [Accessed:2017-12-21].

[42] T. Y. Fan, "Quasi-three-level lasers," in *Solid State Lasers: New Developments and Applications*, M. Inguscio and R. Wallenstein, Eds. Springer, 1993, vol. 317, pp. 189–203.

[43] E. J. Friebele, C. G. Askins, J. R. Peele, B. M. Wright, N. J. Condon, S. O'Connor, C. G. Brown, and S. R. Bowman, "Ho-doped fiber for high energy laser applications," *Proceedings of SPIE*, vol. 8961, pp. 1 – 9, 2014.

[44] R. Paschotta, "Pulse amplification in the steady state," *Encyclopedia of Laser Physics and Technology*, [Online]. Available: https://www.rp-photonics.com/software_news_2017_09_22.html. [Accessed:2017-12-19].

[45] R. Paschotta, "Saturation energy," *Encyclopedia of Laser Physics and Technology*, [Online]. Available: https://www.rp-photonics.com/saturation_energy.html. [Accessed:2018-06-09].

[46] J. Hecht, "High-efficiency optical pumping; 'going green' cranks up the laser power.(report)," *Laser Focus World*, vol. 52, no. 4, pp. 45–48, 2016.

[47] R. Paschotta, "Quantum defect," *Encyclopedia of Laser Physics and Technology*, [Online]. Available: https://www.rp-photonics.com/quantum_defect.html. [Accessed:2017-12-19].

[48] R. Paschotta, "Amplified spontaneous emission," *Encyclopedia of Laser Physics and Technology*, [Online]. Available: https://www.rp-photonics.com/amplified_spontaneous_emission.html. [Accessed:2017-12-19].

[49] C. W. Rudy, M. J. Digonnet, and R. L. Byer, "Advances in 2- μm Tm-doped mode-locked fiber lasers," *Optical Fiber Technology*, vol. 20, no. 6, pp. 642 – 649, 2014.

[50] J. Singh, *Smart Electronic Materials: Fundamentals and Applications*. Cambridge University Press, 2005.

[51] R. Paschotta, "Fiber-coupled diode lasers," *Encyclopedia of Laser Physics and Technology*, [Online]. Available: https://www.rp-photonics.com/pulse_pickers.html. [Accessed:2018-06-20].

[52] R. Paschotta, "Fiber bragg gratings," *Encyclopedia of Laser Physics and Technology*, [Online]. Available: https://www.rp-photonics.com/bandwidth.html. [Accessed:2018-06-03].

[53] C. Elachi and J. J. van Zyl, *Introduction To The Physics and Techniques of Remote Sensing*. John Wiley & Sons, 2006.

[54] T. Fujii and T.Fukuchi, *Laser Remote Sensing*. Taylor & Francis, 2005.

[55] A. Johansen, A. Czajkowski, M. Scobey, P. Egerton, and R. Fortenberry, "Thin-Film Interference Filters for LIDAR," *Alluxa White Paper Series*, 2017.

[56] D. Gatziolis and H.-E. Andersen, "A Guide to LIDAR Data Acquisition and Processing for the Forests of the Pacific Northwest, Pacific Northwest Research Station, Forest Service, United States Department of Agriculture, Tech. Rep. PNW-GTR-768, 2008.

[57] R. Paschotta, "Photodiodes," *Encyclopedia of Laser Physics and Technology*, [Online]. Available: https://www.

rp-photonics.com/photodiodes.html. [Accessed:2018-06-25].

[58] M. Milenković, Class Lecture, "Lecture notes: Introduction to LiDAR", Department of Geodesy and Geoinformation, Vienna University of Technology, 2014. [Online]. Available: http://www.newfor.net/wp-content/uploads/2014/07/Introduction_Lidar_M.Milenkovic.pdf. [Accessed:2018-06-17].

[59] B. Friedland, "On definitions of bandwidth and response time," in *2016 IEEE 11th Conference on Industrial Electronics and Applications*, 2016, pp. 1945–1948.

[60] J. W. Giles, I. N. Bankman, R. M. Sova, T. R. Morgan, D. D. Duncan, J. A. Millard, W. J. Green, and F. J. Marcotte, "Lidar system model for use with path obscurants and experimental validation," *Applied Optics*, vol. 47, no. 22, pp. 4085–4093, 2008.

[61] A. T. Reghunath, N. K. Verma, and Y. Kumar, "Estimation of signal and noise for a differential absorption lidar in the mid-infrared band," *Proceedings of SPIE*, vol. 6409, pp. 1 – 6, 2006.

[62] M. Vazquez-Navarro, *Life cycle of contrails from a time series of geostationary satellite images*. Doctoral Thesis accepted by Ludwig-Maximilians-Universität, Germany, 2009.

[63] G. Shayeganrad and P. Parvin, "DIAL–phoswich hybrid system for remote sensing of radioactive plumes in order to evaluate external dose rate," *Progress in Nuclear Energy*, vol. 51, no. 3, pp. 420–433, 2008.

[64] N. Cao, C. Zhu, Y. Kai, and P. Yan, "A method of background noise reduction in lidar data," *Applied Physics B: Lasers and Optics*, vol. 113, no. 1, pp. 115–123, 2013.

[65] V. Mackowiak, J. Peupelmann, Y. Ma, and A. Gorges, "NEP – Noise Equivalent Power," *Thorlabs White Paper*, [Online]. Available: https://www.thorlabs.com/images/TabImages/Noise_Equivalent_Power_White_Paper.pdf. Accessed:2018-06-20].

[66] J. Ready, "Optical detectors and human vision," in *Fundamentals of Photonics*, C. Roychoudhuri, Ed. SPIE, 2000, vol. 1, pp. 211–248.

[67] D. G. Andrews, *An Introduction to Atmospheric Physics*. Cambridge University Press1, 2010.

[68] Figure from: "Remote Sensing Notes", Japan Association of Remote Sensing, Ed. 1996. [Online]. Available: http://wtlab.iis.u-tokyo.ac.jp/wataru/lecture/rsgis/rsnote/cp1/1-11-2.gif. Accessed:2018-06-20].

[69] Figure provided by P. J. Espy.

[70] A. J. Cox, A. J. DeWeerd, and J. Linden, "An Experiment to Measure Mie and Rayleigh Total Scattering cross Sections," *American Journal of Physics*, vol. 70, no. 6, pp. 620–625, 2002.

[71] J. S. Steinhart and S. R. Hart, "Calibration curves for thermistors," *Deep Sea Research and Oceanographic Abstracts*, vol. 15, no. 4, pp. 497–503, 1968.

[72] Eblana Photonics, "DM Butterfly Report," EP2051-0-DMH-B46-FA YE3131 datasheet, 2017.

[73] N. Tolstik, I. K. Bakke, E. Sorokin, and I. T. Sorokina, "All-PM All-diode-pumped Mode-locked Holmium Fiber MOPA laser system," in *High-Brightness Sources and Light-driven Interactions*. Optical Society of America, 2018.

[74] Innolume, "Test report for FBG-coupled laser diode module with optical isolator," LD-1150-FBG-300 DO2160d-q3-Bo4-G05 datasheet, 2017.

[75] Innolume, "Test report for FBG-coupled laser diode module with optical isolator," LD-1150-FBG-300 DO2160d-q3-Bo4-G11 datasheet, 2017.

[76] *RP Fiber Power V5.0*, RP Photonics Consulting GmbH, Bad Dürrheim, Germany, 2014.

[77] J. Gene, S. K. Kim, and S. D. Lim, "Study of methodology for gain-switched holmium-doped fiber laser combined with Q-switched Thulium-doped fiber laser," in *2017 Conference on Lasers and Electro-Optics Europe European Quantum Electronics Conference*, 2017, pp. 1–1.

[78] O. M. Christensen, *1.55 micron high-brightness pulsed fiber lasers for LIDAR applications*. Project Work accepted by the Norwegian University of Science and Technology, Norway, 2008.

[79] L. Mei, P. Guan, Y. Yang, and Z. Kong, "Atmospheric extinction coefficient retrieval and validation for the single-band Mie-scattering Scheimpflug lidar technique," *Optics Express*, vol. 25, no. 16, pp. A628–A638, 2017.

[80] Y. Wang, J. Zhang, Q. Fu, Y. Song, B. L. H. Di, and D. Hua, "Variations in the water vapor distribution and the associated effects on fog and haze events over Xi'an based on Raman lidar data and back trajectories," *Applied Optics*, vol. 56, no. 28, pp. 7927–7938, 2017.

[81] E. Abramov, M. Evzelman, O. Kirshenboim, T. Urkin, and M. M. Peretz, "Low voltage sub-nanosecond pulsed current driver IC for high-resolution LIDAR applications," *2018 IEEE Applied Power Electronics Conference and Exposition, 2018*, pp. 708–715.

[82] R. Paschotta, "Pulse pickers," *Encyclopedia of Laser Physics and Technology*, [Online]. Available: https://www.rp-photonics.com/pulse_pickers.html. [Accessed:2018-06-20].

[83] S. Kobtsev, S. Kukarin, and Y. Fedotov, "Ultra-low repetition rate mode-locked fiber laser with high-energy pulses," *Optics Express*, vol. 16, no. 26, pp. 21 936–21 941, 2008.

[84] A. V. Smith, B. T. Do, G. R. Hadley, and R. L. Farrow, "Optical Damage Limits to Pulse Energy from Fibers," *IEEE Journal of Selected Topics in Quantum Electronics*, vol. 15, no. 1, pp. 153–158, 2009.

[85] R. Paschotta, "Large mode area fibers," *Encyclopedia of Laser Physics and Technology*, [Online]. Available: https://www.rp-photonics.com/large_mode_area_fibers.html. [Accessed:2018-01-16].

[86] W. Gong, A. Liang, G. Han, X. Ma, and C. Xiang, "Sensitivity of on-line wavelength during retrieval of atmospheric CO_2 vertical profile," *Photonics Research*, vol. 3, no. 4, pp. 146–152, 2015.